Signal Design and Processing Techniques for WSR-88D Ambiguity Resolution

Staggered PRT Updates and Generalized Phase Codes

National Severe Storms Laboratory Report

prepared by: **Sebastian Torres, David Warde, and Dusan Zrnic**

with contributions from: **Valery Melnikov**

Part 12
May 2009

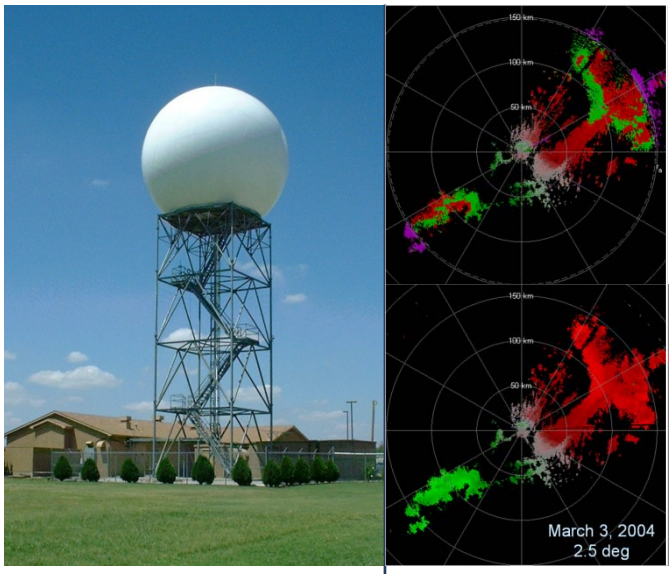

National Oceanic and Atmospheric Administration
National Severe Storms Laboratory
Norman, Oklahoma 73072

SIGNAL DESIGN AND PROCESSING TECHNIQUES FOR WSR-88D AMBIGUITY RESOLUTION

Part 12: Staggered PRT Updates and Generalized Phase Codes

National Severe Storms Laboratory Report

prepared by: Sebastián Torres, David Warde, and Dusan Zrnić

May 2009

NOAA, National Severe Storms Laboratory
120 David L. Boren Blvd., Norman, Oklahoma 73072

SIGNAL DESIGN AND PROCESSING TECHNIQUES FOR WSR-88D AMBIGUITY RESOLUTION

Part 12: Staggered PRT Updates and Generalized Phase Codes

Contents

SIGNAL DESIGN AND PROCESSING TECHNIQUES FOR WSR-88D AMBIGUITY RESOLUTION

Part 12: Staggered PRT Updates and Generalized Phase Codes

1. Introduction

The Radar Operations Center (ROC) of the National Weather Service (NWS) has funded the National Severe Storms Laboratory (NSSL) to address the mitigation of range and velocity ambiguities in the WSR-88D. This is the twelfth report in the series that deals with range and velocity ambiguity resolution in the WSR-88D (other relevant reports are listed at the end). It documents NSSL accomplishments in FY08.

We start in section 2 with a brief description of two data sets that were collected during this year. These sets augment our large collection of data sets from previous years. Some of these cases are listed on our website (*http://cimms.ou.edu/rvamb/home.htm*); only few have been thoroughly analyzed.

Section 3 is devoted to staggered PRT (SPRT). First, we describe the evolution of the SPRT algorithm and justify the recommended updates (the reader should note that because of delays in publishing this report, the SPRT algorithm described here is not the most recent). A revised set of criteria that trades-off range coverage for better performance is proposed to define scanning strategies that exploit SPRT. Last, we explore in great detail the performance of the spectral SPRT clutter filter to demonstrate that it meets WSR-88D System Specification requirements.

Section 4 documents the exploratory work in the area of generalized phase codes. We look at the family of SZ(n/64) codes and compare their performance to the familiar SZ(8/64). Because, SZ(8/64) is not always the best choice, we recommend further research and SZ-2 algorithm changes to exploit the improved performance of other codes in this family.

Section 5 includes advanced techniques. The first part of this section describes the concept of polarimetric spectral densities and their application for adaptive ground clutter filtering. The second part revisits the concept of range oversampling and illustrates possible data quality improvements via simple examples.

This report also includes four appendices. Appendix A contains an updated description of the staggered PRT algorithm that uses the DC removal ground clutter filter (this is the 2008 version). Appendix B summarizes our recommendations for VCPs that exploit SPRT for range and velocity ambiguity mitigation. Appendix C includes a relevant paper that was presented at the European Radar conference in Helsinki, Finland during this year. Appendix D is a short NSSL report documenting a clutter recognition technique using dual polarization.

Once again, the work performed in FY08 exceeded considerably the allocated budget; hence, a part of it had to be done on other NOAA funds.

2. Data Collection

Due to the numerous data cases collected in previous years and other projects competing for radar time, data collection during FY08 was limited to just two cases.

A new volume coverage pattern (VCP) was created: RV-CE-02052.vcp. VCP 2052 is summarized in Table 2.1 and was developed to evaluate the performance of generalized SZ codes.

Elev. (deg)	AZ Rate (deg/s)	WF Type	PRT #	*M*
0.5	18.7	CS	1	17
0.5	19.2	CD	5	52
0.5	20.0	SZ(8/64)	8	64
0.5	20.0	SZ(4/64)	8	64
0.5	20.0	SZ(3/64)	8	64
1.5	19.8	CS	1	16
1.5	19.2	CD	5	52
1.5	20.0	SZ(8/64)	8	64
1.5	20.0	SZ(4/64)	8	64
1.5	20.0	SZ(3/64)	8	64

Table 2.1. VCP 2052.

A data set using VCP 2052 was collected with the KOUN radar on 11 September 2008 at 15:47 CDT. This is a case of stratiform precipitation associated with a mesoscale convective system. In addition to the VCP data, we collected 500 radials of spotlight data at an elevation of 0.4 deg and azimuth of 38 deg. 100 radials were collected for each of the acquisition settings of the first 5 tilts of VCP 2052.

3. Staggered PRT

3.1. Algorithm Evolution and Updates

3.1.1. *A short history of the staggered PRT algorithm*

The staggered pulse repetition time (SPRT) concept was initially proposed for the mitigation of range and velocity ambiguities on weather radars in the 70s (Sirmans et al. 1976). SPRT has significantly evolved in over three decades, much in part due the work of scientists at NSSL. In 1985, Zrnić and Mahapatra examined the statistical performance of SPRT in great detail. Whereas a PRT ratio close to one would be ideal to maximally extend the Nyquist velocity, errors of estimates limit the maximum PRT ratio that can be used in practice. A PRT ratio of 2/3 was quickly identified as one that could lead to an operational algorithm. However, the main limitation of SPRT had been the lack of an effective ground clutter filter for the staggered sampling. In 1999 (NSSL Report 3), NSSL developed the concept for a spectral ground clutter filter that works with a staggered PRT ratio of 2/3. However, this filter had not been perfected until recently. NSSL's report 7 (2003) contains an algorithm description for SPRT using a simpler DC removal ground clutter filter. Since 2005, NSSL has been working on perfecting the spectral SPRT clutter filter, referred to as SACHI (Spectral Algorithm for Clutter Harmonics Identification and removal). NSSL's report 9 (2005) contains the first formal description of such filter, and NSSL's report 11 (2007) contains further updates and documentation of its performance.

3.1.2. *Updates to the SPRT Algorithm*

Although the ground clutter suppression of the DC removal filter is not enough to meet the WSR-88 System Specification requirements, the ROC decided to implement it on the ORDA for a simpler version of the SPRT algorithm that could be used for initial engineering testing. In April of 2008, the SPRT algorithm with a DC removal clutter filter was improved: it was revised to fit the RVP-8's signal processing architecture, and it was generalized for any staggered PRT ratio. Table 3.1.1 shows a high-level list of steps in the SPRT algorithm; a complete description is included in this report as Appendix A.

```
If the PRT ratio has changed
   1. Pre-computation of velocity de-aliasing rules
End
For each range bin n, where 0 ≤ n < max(N1,N2)
   2. Clutter filtering
   3. Power and correlation computations for each PRT
End
4. Short/long PRT data swap
For each range bin n, where 0 ≤ n < N2
   5. Combined power computation
End
6. Strong point clutter canceling
For each range bin n, where 0 ≤ n < N2
   7. Signal power computation
   8. Reflectivity computation
   9. Velocity computation
   10.  Spectrum width computation
   11.  Determination of significant returns for reflectivity
   12.  Determination of significant returns for velocity
   13.  Determination of significant returns for spectrum
      width
End
For each range bin n, where 0 ≤ n < N2
   14.  Determination of overlaid returns for velocity and
      spectrum width
End
```

Table 3.1.1. Staggered PRT high-level algorithm description.

The new algorithm includes updates in the following areas:

- Re-ordering of steps,
- Generalized velocity dealiasing rules,
- Ground clutter filtering,
- Spectrum width estimation, and
- Overlaid censoring rules.

Discussion of the specific changes follows next.

a) Short/long-PRT order

The updated algorithm works with any PRT ordering. That is, it is not assumed that the first PRT is the short PRT.

b) Re-ordered steps

Combined powers are computed at an early stage to accommodate the strong-point clutter filter in the ORDA.

c) Generalized velocity dealiasing rules

The old algorithm could only handle a PRT ratio of 2/3, which leads to a minimum number of velocity dealiasing rules and is mandatory if using SACHI. However, this constraint is not needed if using the DC removal clutter filter. Velocity dealiasing rules are now generalized to any PRT ratio. Other PRT ratios may prove useful in matching requirements and extending the Nyquist velocity in situations where there is not strong clutter contamination. A velocity dealiasing rule is associated with each constant level in

the velocity difference transfer function (VDTF), as illustrated in Fig. 3.1.1. The new algorithm includes a recursive algorithm to generate the dealiasing rules as described in Torres et al. (2004). Rule values are normalized by the extended Nyquist velocity, so they can be pre-computed for any given PRT ratio. For example, for PRT ratios of 2/3 and 3/5, the VDTF constant values and associated dealiasing rules are given in Tables 3.1.2 and 3.1.3. Velocities are dealiased by using the dealiasing factor that corresponds to the VDTF constant that is the closest to $\hat{v}_1 - \hat{v}_2$ (i.e., the difference between the short- and long-PRT velocity estimates). A dealiased velocity is obtained as $\hat{v} = \hat{v}_1 + 2v_{a1}P$, where P is the dealiasing factor. As previously documented, this process fails if errors of velocity estimates are such that the wrong dealiasing factor (P) is selected. These dealiasing errors are termed "catastrophic errors" and, as shown in Fig. 3.1.2, they appear as speckles in the velocity fields. As expected, these errors are associated with large spectrum width values.

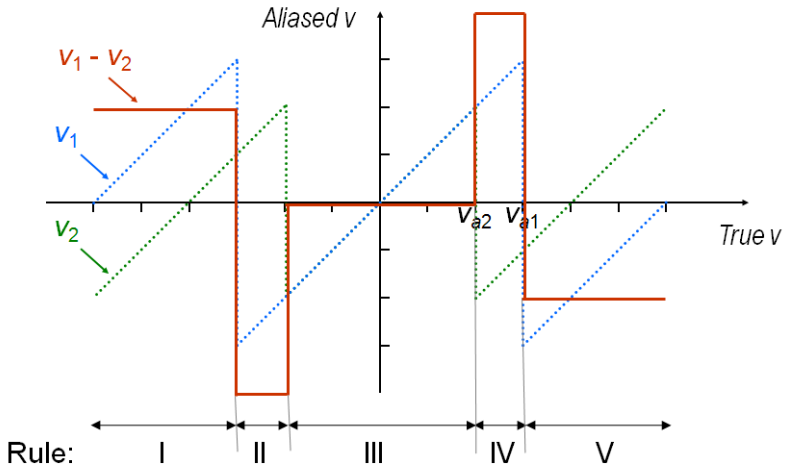

Fig. 3.1.1. Velocity difference transfer function for a PRT ratio of 2/3. A specific dealiasing rule (indicated with roman numerals) is associated with each constant value of this function.

VDTF constant	v_{a2}	$-2v_{a2}$	0	$2v_{a2}$	$-v_{a2}$
Dealiasing factor	-1	0	0	0	1

Table 3.1.1. Dealiasing rules for a PRT ratio of 2/3.

VDTF constant	$-2v_{a2}/3$	$4v_{a2}/3$	$-2v_{a2}$	0	$2v_{a2}$	$-4v_{a2}/3$	$2v_{a2}/3$
Dealiasing factor	-1	-1	0	0	0	1	1

Table 3.1.2. Dealiasing rules for a PRT ratio of 3/5.

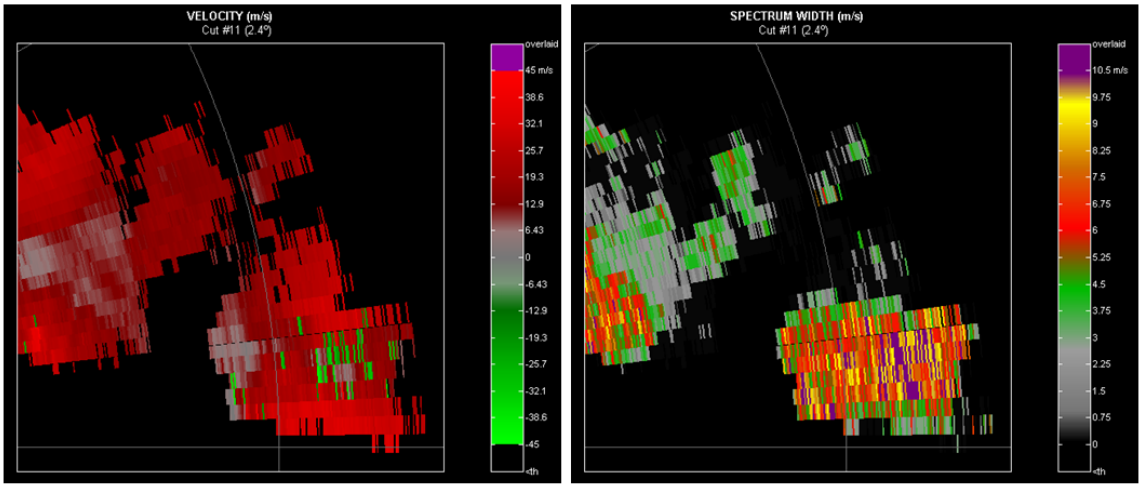

Fig. 3.1.2. Example of "catastrophic errors" and their association with large spectrum widths.

d) Ground clutter filtering

In the previous algorithm, the DC removal was done on the autocovariances. That is, the filtered power was obtained as in Fig. 3.1.3, or mathematically as $P_F^{(old)} = \frac{1}{M}\sum_{m=0}^{M-1}|V(m)|^2 - \left|\frac{1}{M}\sum_{m'=0}^{M-1}V(m')\right|^2$, where V are the complex samples in the dwell time. However, to match the RVP-8 software architecture, the new implementation is as

shown in Fig. 3.1.4, or mathematically as $P_F^{(new)} = \frac{1}{M}\sum_{m=0}^{M-1}\left|V(m) - \frac{1}{M}\sum_{m'=0}^{M-1}V(m')\right|^2$. It is not difficult to prove that the previous two equations are mathematically equivalent.

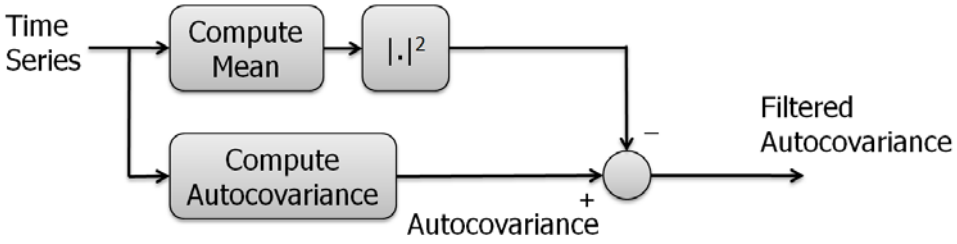

Fig. 3.1.3. Old DC removal clutter filter.

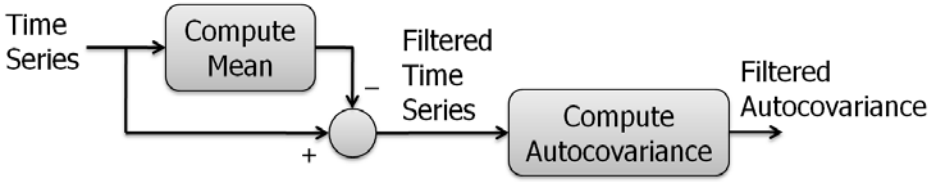

Fig. 3.1.4. New DC removal clutter filter.

However, in the SPRT algorithm, powers are computed independently for each PRT set and mean computations are performed on the entire sample set. That is,

$$P_{F_i}^{(old)} = \frac{1}{M_p}\sum_{m=0}^{M_p-1}\left|V(2m+i)\right|^2 - \left|\frac{1}{M}\sum_{m'=0}^{M-1}V(m')\right|^2, \text{ and}$$

$$P_{F_i}^{(new)} = \frac{1}{M_p}\sum_{m=0}^{M_p-1}\left|V(2m+i) - \frac{1}{M}\sum_{m'=0}^{M-1}V(m')\right|^2,$$

where i = 0, 1 selects the short- and long-PRT sets, respectively. In this case, the "old" and "new" filters are different, and this is easily verified on real data (Fig. 3.1.5). Still,

the performance of these two filters should be equivalent in statistical terms. This is verified by computing the expected values of the two filtered powers:

$$E\left[P_{F_i}^{(old)}\right] = \frac{1}{M_p}\sum_{m=0}^{M_p-1} E\left[\left|V(2m+i)\right|^2\right] - E\left[\left|\frac{1}{M}\sum_{m'=0}^{M-1} V(m')\right|^2\right], \text{ and}$$
$$= E\left[\left|V\right|^2\right] - E\left[P_{DC}\right]$$

$$E\left[P_{F_i}^{(new)}\right] = \frac{1}{M_p}\sum_{m=0}^{M_p-1} E\left[\left|V(2m+i) - V_{DC}\right|^2\right]$$
$$= E\left[\left|V - V_{DC}\right|^2\right]$$
$$= E\left[\left|V\right|^2 - V^* V_{DC} - V V_{DC}^* + \left|V_{DC}\right|^2\right]$$
$$= E\left[\left|V\right|^2\right] - E\left[\left|V_{DC}\right|^2\right]$$
$$= E\left[\left|V\right|^2\right] - E\left[P_{DC}\right].$$

,

where V_{DC} and P_{DC} are the DC voltage and DC power, respectively.

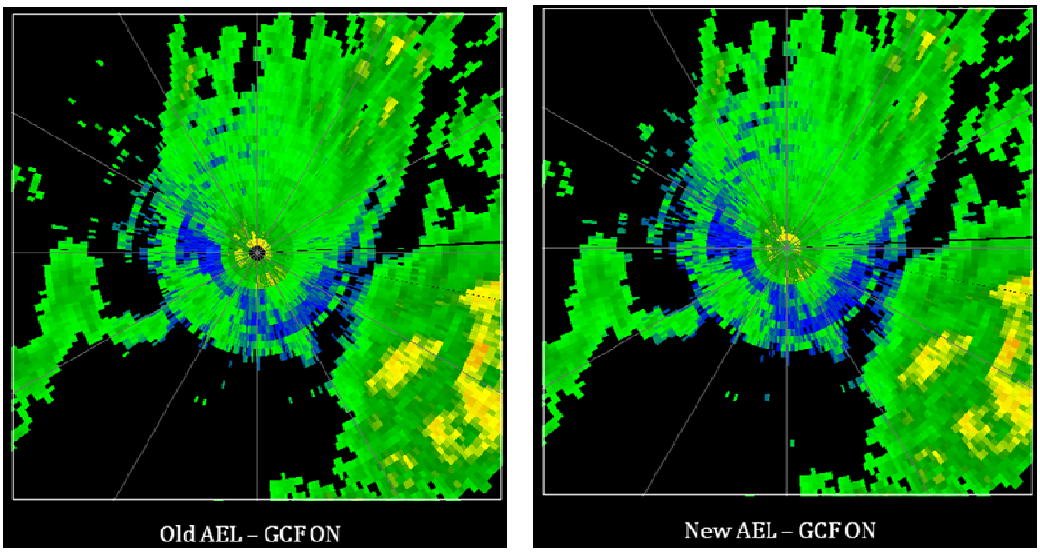

Fig. 3.1.5. Performance comparison between the "old" (left panel) and "new" (right panel) DC removal filter implementations on real data.

e) Spectrum width computation

The algorithm uses the classical spectrum width estimator based on the ratio of lag-0 to lag-1 autocorrelation magnitudes, but autocorrelation values can be estimated in different ways. Lag-0 autocorrelation (i.e., signal power) could be estimated from the short-PRT samples only, from the long-PRT samples only, or from all samples. Lag-1 autocorrelation could be estimated from either the short-PRT pairs or the long-PRT pairs. Hence, there are a total of six variations that could be implemented. The best alternative should be selected based on statistical performance and saturation effects. Fig. 3.1.5 shows the standard deviation of spectrum width estimates as a function of the true spectrum width for a signal-to-noise ratio of 40 dB, a dwell time of 60 ms, and a PRT ratio of 2/3. The short PRT (T_1) was varied from 0.5 ms to 2 ms in 0.5 ms steps, and 4 estimators are being evaluated since the difference between using only short- or long-PRT samples for lag-0 autocorrelation estimates is insignificant. The old algorithm implemented the spectrum width estimator that uses only the long-PRT samples and pairs for the lag-0 and lag-1 autocorrelation estimates, respectively. In Fig. 3.1.6, the performance of this estimator is given by the solid lines with markers. As shown in this figure, no single estimator provides the best performance under all conditions. However, the best performance overall is achieved when using all samples for power and the short-PRT pairs for the lag-1 autocorrelation (dashed lines without markers), which also results in a higher saturation value.

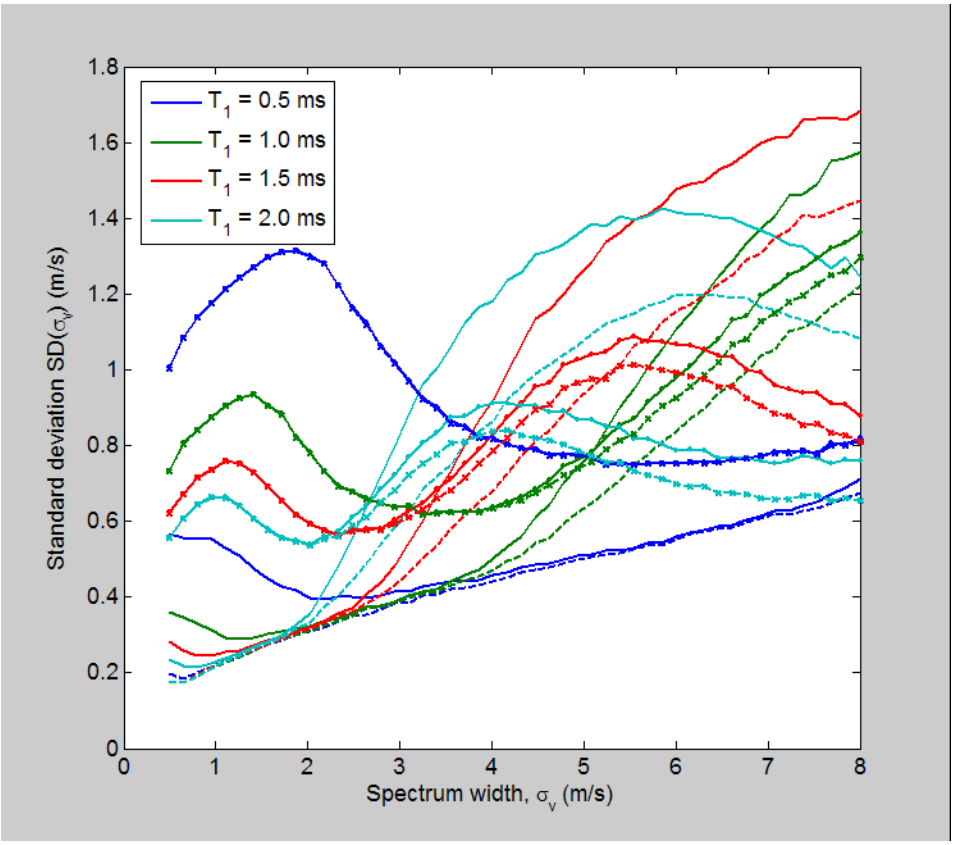

Fig. 3.1.6. Standard deviation of spectrum width estimates as a function of the true spectrum width for different estimators and different PRTs. Solid lines correspond to estimators that use only half of the samples (only short- or long-PRT samples) for the lag-0 autocorrelation estimates. Dashed lines correspond to estimators that use all samples for the lag-0 autocorrelation estimates. Lines without markers correspond to estimators that use the short-PRT pairs for the lag-1 autocorrelation estimates. Lines with markers correspond to estimators that use the long-PRT pairs for the lag-1 autocorrelation estimates.

f) Censoring of overlaid echoes

The SPRT algorithm assumes that there are no significant returns beyond the maximum unambiguous range corresponding to the long PRT (r_{a2}). However, echoes from ranges between the maximum unambiguous range of the short PRT (r_{a1}) and r_{a2} may be overlaid in every other pulse. Fig. 3.1.7 depicts the three regions in the SPRT algorithm. Based on the initial assumption, segment I cannot contain overlaid echoes in the short-PRT pulses,

but may in the long-PRT pulses. No overlaid echoes can occur in segment II or segment III, but segment II data is only available from the long-PRT pulses.

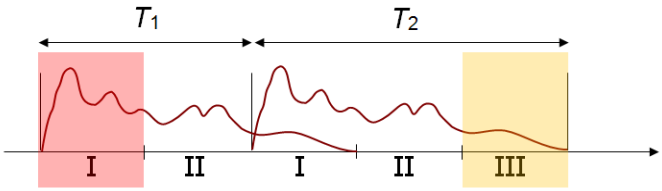

Fig. 3.1.7. Depiction of the three range segments in the SPRT algorithm.

Hence, reflectivity is computed from the short-PRT pulses in segment I, from all pulses in segment II, and from the long-PRT pulses in segment III. However, velocity and spectrum widths can only be computed up to r_{a1}, and because these estimates are obtained from pairs and not individual samples, the SPRT algorithm must determine the presence of overlaid echoes to avoid biased estimates. Overlaid echoes are detected by analyzing the powers from the short-PRT samples in segment I and the corresponding powers from the long-PRT samples in segment III. That is, segment I will contain purple haze if, for any range gate (n) in segment I, $P_1(n) < P_2(n + N_1) + T_{ov}$, where N_1 is the number of range gates in the short PRT and T_{ov} is the overlaid power threshold. To match the behavior of overlaid echo detection in other ORDA modes, the algorithm was modified to perform the above check only if $P_2(n + N_1)$ is a significant return (i.e., exceeds the SNR threshold). Fig. 3.1.8 shows the performance of the overlaid echo detection technique with and without this consideration. Although more realistic, the old check results in more purple haze. It is worth noting that velocities and spectrum widths in segment II will not contain any purple haze, and will be all purple in segment III as the short-PRT samples are unavailable to form the pairs. This is depicted by an example in Fig. 3.1.9.

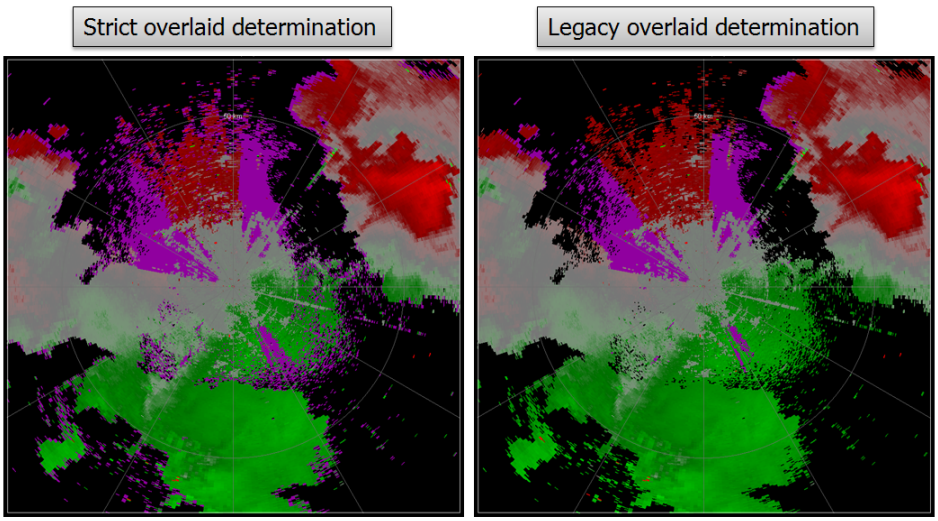

Fig. 3.1.8. Example of old (left) and new (right) overlaid echo determination.

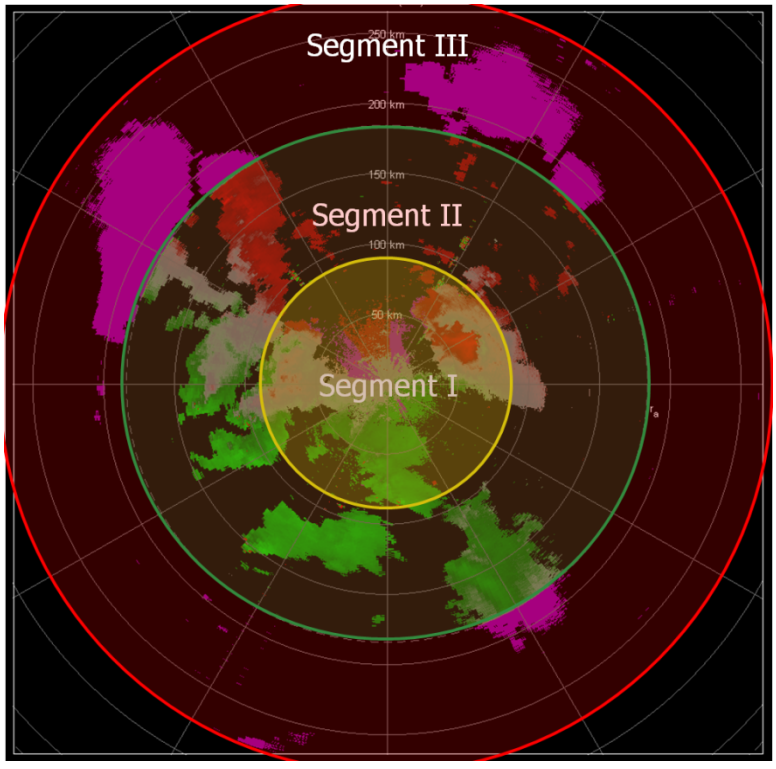

Fig. 3.1.9. Example of overlaid echoes in the three SPRT range segments.

3.2. Volume Coverage Patterns for the SPRT Algorithm

This year, we also worked closely with the ROC to validate the ORDA implementation of the recommended SPRT algorithm. Equally important to the algorithm is the design of volume coverage patterns (VCP) that exploit the technique in the most effective way. In general, the design of a VCP is tied to six performance indicators:

- Acquisition time,
- Maximum unambiguous range,
- Maximum unambiguous velocity,
- Saturation of the spectrum width,
- Error of estimates, and
- Ground clutter suppression.

These performance indicators were explained in detail in our report 11 (2007). In general, the problem boils down to selecting the best short PRT for a given situation (i.e., there is only one degree of freedom). On one hand, longer PRTs are needed to obtain longer unambiguous ranges. The required maximum unambiguous range is dictated by the antenna elevation angle and the maximum height of storms (see Fig. 3.1.9). On the other hand, shorter PRTs will provide a number of benefits: larger Nyquist velocity, larger maximum measurable spectrum width, more samples for a given dwell time, lower variance of velocity and spectrum width estimates, lower rate of catastrophic errors, and better ground clutter suppression (see section 3.3). Hence, it is evident that one should select the shortest set of possible PRTs.

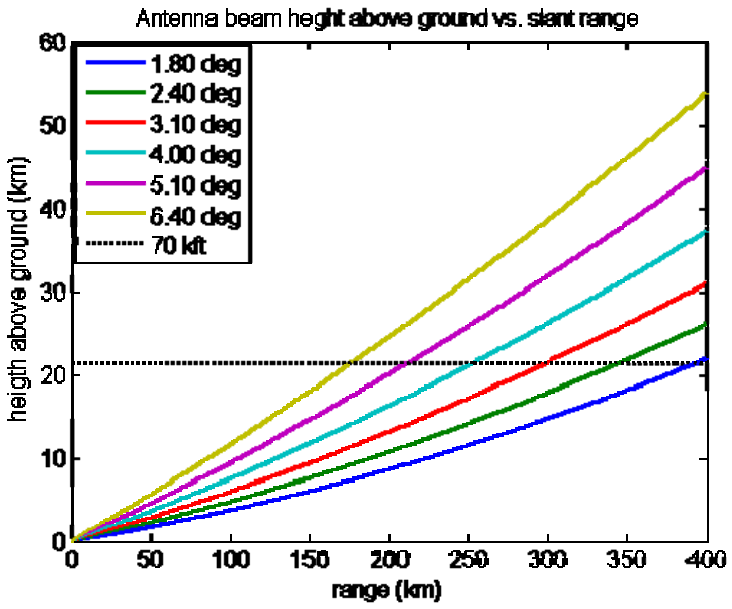

Fig. 3.1.9. Required maximum unambiguous range for different antenna elevation angles and the required maximum height of storms of 70,000 ft.

Assume that T_1 and T_2 are the short and long PRTs, respectively, and that the PRT ratio is 2/3, which is a requirement to use the SACHI filter. Their associated maximum unambiguous ranges are $r_{a,1} = cT_1/2$ and $r_{a,2} = cT_2/2 = 3cT_1/4$, where c is the speed of light. Also, with the current SPRT algorithm, the maximum unambiguous ranges for surveillance and Doppler are given by $r_{a,S} = r_{a,2}$ and $r_{a,D} = r_{a,1}$, respectively. With these definitions in mind, several criteria can be used to select the shortest PRT possible for a staggered PRT VCP. The most restrictive criterion consists in selecting the PRTs such that there are no overlaid echoes. That is, $r_{a,1} \geq r_{\max}$, where r_{max} is the maximum range of storms for a given elevation angle as depicted in Fig. 3.1.9. Hence the short PRT can be chosen as $T_1 = 2r_{\max}/c$, and the long PRT follows from this as $T_2 = 3T_1/2$. Whereas the no-overlay condition would be ideal, this is not a requirement for the current algorithm. Another criterion, which is less restrictive but an algorithm limitation, consists in

selecting the PRTs such that there are no overlaid echoes from the long-PRT into the short-PRT pulses. That is, $r_{a,2} \geq r_{\max}$, and $T_1 = 4r_{\max}/3c$, which is smaller than $2r_{\max}/c$. However, in this situation, $r_{a,1} < r_{\max}$ and, unlike with split cuts or the batch mode, the algorithm cannot currently handle range unfolding (we are currently researching ways to do this!).

In 2007, we recommended two SPRT test VCPs based on the elevation angles of the operational VCP 12. One of these VCPs is included in Table 3.1.3 for reference purposes. Fig. 3.1.10 shows the design criteria used to select the PRTs for each elevation angle based on the required r_{max}. For elevation angles at or above 4 deg (r_{max} < 242 km), the short PRT is chosen such that there are no overlaid echoes (i.e., the green line in Fig. 3.1.10 stays above the dotted line for r_{max}). As the elevation angle increases, T_1 decreases until the maximum unambiguous velocity reaches about 60 m/s, which should not be exceeded to prevent a coarser quantization of the 8-bit velocity data. For elevation angles below 4 deg (r_{max} > 242 km), the short PRT is chosen so that there are no echoes beyond $r_{a,2}$ (i.e., the red line in Fig. 3.1.10 stays above the dotted line for r_{max}) and to meet the required minimum Doppler coverage of 230 km.

VCP 14	*Optimum SPRT w/limited PRT set*												
Angle (°)	AZ Rate (deg/s)	Period (sec)	WF Type	PRF #	No. Pulses	PRF #	No. Pulses	T1 (ms)	T2 (ms)	DT (ms)	ra,S (km)	ra,D (km)	va (m/s)
0.50	21.15	17.02	CS	1	15			3.11		46.60	466		
0.50	25.00	14.40	CD			5	40		0.99	39.47		148	26.7
0.90	21.15	17.02	CS	1	15			3.11		46.60	466		
0.90	25.00	14.40	CD			5	40		0.99	39.47		148	26.7
1.30	21.15	17.02	CS	1	15			3.11		46.60	466		
1.30	25.00	14.40	CD			5	40		0.99	39.47		148	26.7
1.80	24.60	14.63	SPRT			1	18	1.74	2.61	39.15	391	261	30.2
2.40	26.40	13.64	SPRT			2	18	1.62	2.43	36.38	364	242	32.5
3.10	26.40	13.64	SPRT			2	18	1.62	2.43	36.38	364	242	32.5
4.00	26.40	13.64	SPRT			2	18	1.62	2.43	36.38	364	242	32.5
5.10	28.01	12.85	SPRT			3	18	1.49	2.24	33.62	336	224	35.2
6.40	28.01	12.85	SPRT			5	22	1.25	1.87	34.32	281	187	42.1
8.00	28.40	12.68	SPRT			7	28	1.00	1.50	35.07	225	150	52.5
10.00	28.88	12.46	SPRT			8	30	0.88	1.32	33.08	198	132	59.6
12.50	28.74	12.53	SPRT			8	32	0.88	1.32	35.28	198	132	59.6
15.60	28.74	12.53	SPRT			8	32	0.88	1.32	35.28	198	132	59.6
19.50	28.74	12.53	SPRT			8	32	0.88	1.32	35.28	198	132	59.6
	VCP Time	3.97	min										

Table 3.1.3. Staggered PRT test VCP recommended in 2007.

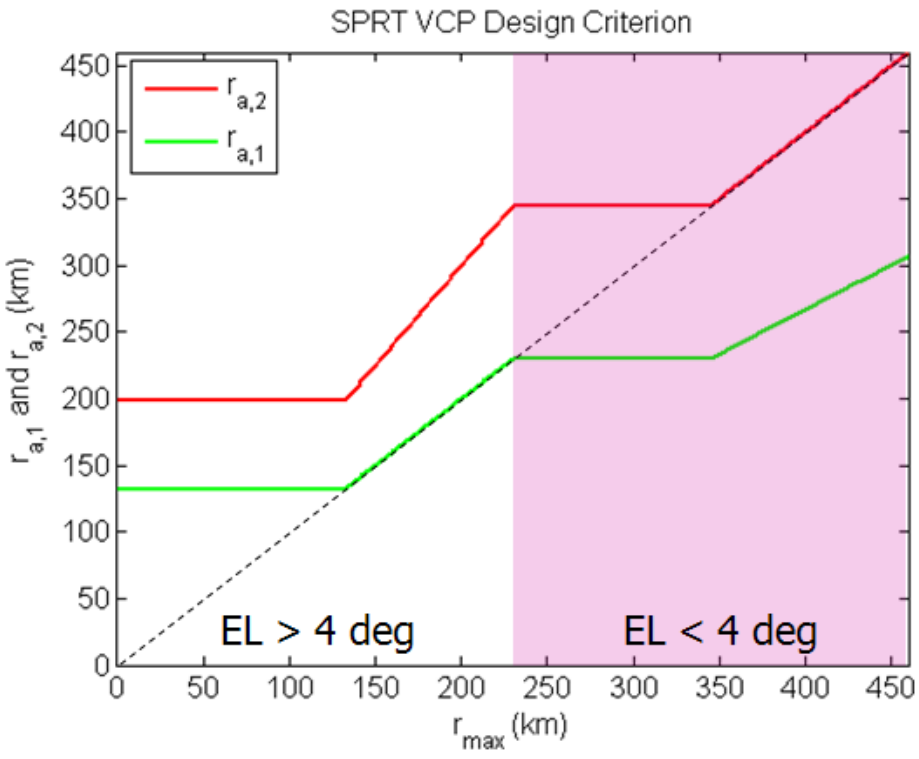

Fig. 3.1.10. Staggered PRT VCP design criteria used for the test VCPs recommended in 2007.

Based on the previous discussion, the criteria used to select the PRTs in the 2007 VCPs may be too restrictive. Without violating algorithm assumptions, we can select shorter PRTs at the price of allowing overlaid echoes. In general, the PRTs can be chosen such that $r_{a,1} \le r_{\max} \le r_{a,2}$. The lower bound (Fig. 3.1.11, left panel) results in no overlaid echoes, and the upper bound (Fig. 3.1.11, right panel) leads to the shortest PRTs that the algorithm can handle at the price of accepting overlaid echoes. Due to the numerous advantages derived from using shorter PRTs, we recommend allowing for overlaid echoes and working on extending the SPRT algorithm to recover overlaid echoes.

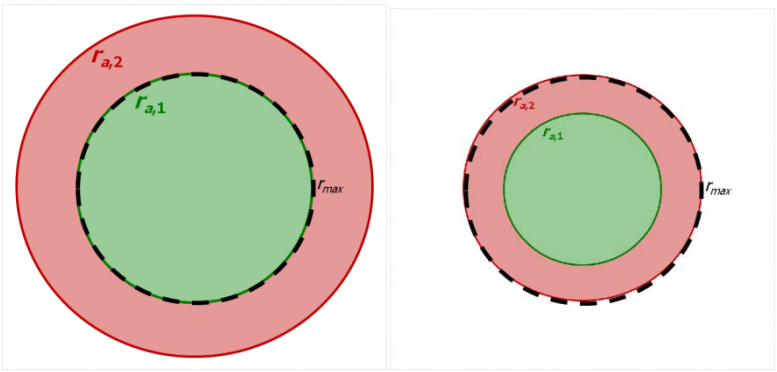

Fig. 3.1.11. Maximum unambiguous range bounds for the SPRT algorithm.

With this in mind, we can relax the no-overlaid-echo criterion and trade shorter PRTs for increased likelihood of overlaid echoes. Fig. 3.1.12 shows the old and new criteria (solid vs. dotted lines). The new criterion results in a range of elevation angles that can use shorter PRTs at the expense of allowing more overlaid echoes. However, the benefits of this trade-off occur at elevations between 2.4 and 10 deg.

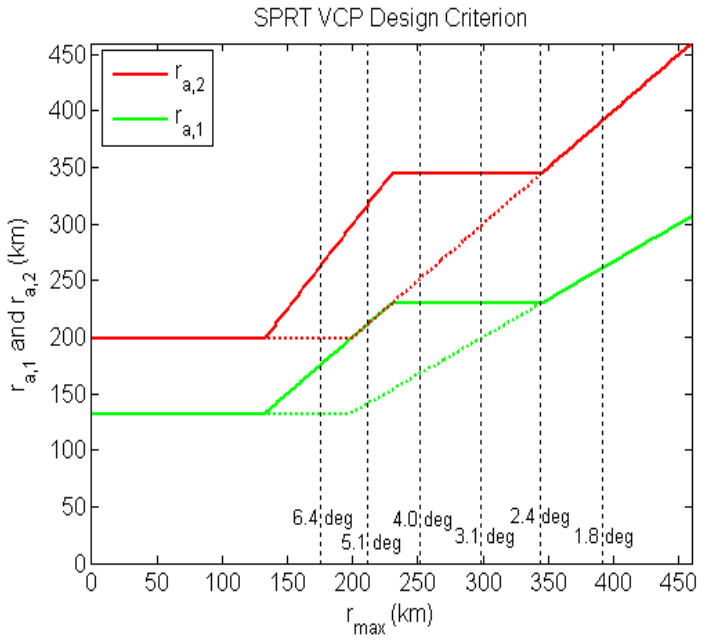

Fig. 3.1.12. Old (solid lines) and new (dashed lines) staggered PRT VCP design criteria.

Once a staggered PRT set is chosen for every elevation in the VCP, we need to establish a criterion for choosing the proper dwell times. On one hand, dwell times must be long enough to meet standard error requirements for reflectivity, velocity, and spectrum width, and also to ensure proper ground clutter suppression. On the other hand, dwell times must be short enough to meet operational needs for faster updates. Based on the performance of the SACHI filter in terms of velocity recovery (see section 3.3), dwell times for optimum clutter suppression may be exceedingly long (depending on the PRTs). Whereas feasible, this is not operationally acceptable! We recommend using dwell times no longer than what is needed to meet spectral moment error requirements. Such dwell times would exceed those of VCP 12; nevertheless, as it will be shown next, they are operationally acceptable.

A proposed staggered PRT VCP is given in Table 3.1.4. The PRTs are chosen for maximum allowable overlay and the dwell times to meet WSR-88D System Specification error requirements, leading to a total VCP time of about 6 minutes. With this VCP, the performance of SACHI may not be optimum everywhere. For example, velocity estimates after clutter filtering may be affected if (1) there is strong clutter contamination, (2) the velocity of the weather signal is around 0, $\pm v_a/5$, or $\pm 2v_a/5$, (3) the SACHI filter does not pick the right weather "replica", *and* (4) the ORPG velocity dealiasing algorithm fails to fix the spatial discontinuity (i.e., the catastrophic error is not isolated). While this has not been quantified, we believe that it will have a relatively minor impact compared to the benefits of using the SPRT algorithm. If this is deemed problematic, it would not be difficult to devise a set of velocity censoring rules to avoid producing noisy velocities after the ground clutter filter. The reader should note that this issue does not affect spectrum width or reflectivity estimates, which have about three times lower standard errors than in the Batch mode.

VCP X *Optimum SPRT with ra1 < rmax < ra2*

Angle (°)	AZ Rate (deg/s)	Period (sec)	WF Type	PRF #	No. Pulses	PRF #	No. Pulses	T1 (ms)	T2 (ms)	DT (ms)	ra,S (km)	ra,D (km)	va (m/s)	σvmax (m/s)	SD(Z) (dB)*	SD(v) (m/s)
0.50	21.46	16.78	CS	1	15			3.11		46.60	466				0.62	
0.50	25.34	14.21	CD			5	40		0.99	39.47		148	26.7	16.3		1.07
0.90	21.46	16.78	CS	1	15			3.11		46.60	466				0.62	
0.90	25.34	14.21	CD			5	40		0.99	39.47		148	26.7	16.3		1.07
1.30	21.46	16.78	CS	1	15			3.11		46.60	466				0.62	
1.30	25.34	14.21	CD			5	40		0.99	39.47		148	26.7	16.3		1.07
1.80	12.68	28.39	SPRT			N/A	36	1.75	2.63	78.87	394	263	30.0	8.1	0.50	0.87
2.40	16.26	22.14	SPRT			N/A	32	1.54	2.31	61.49	346	230	34.2	9.1	0.55	0.98
3.10	16.67	21.60	SPRT			N/A	36	1.33	2.00	59.99	300	200	39.5	10.7	0.55	0.99
4.00	16.11	22.35	SPRT			N/A	44	1.13	1.69	62.07	254	169	46.6	13.0	0.54	0.99
5.10	15.16	23.75	SPRT			N/A	56	0.94	1.41	65.98	212	141	55.8	16.2	0.52	0.99
6.40	15.12	23.81	SPRT			N/A	60	0.88	1.32	66.15	198	132	59.6	17.5	0.51	1.00
8.00	15.12	23.81	SPRT			N/A	60	0.88	1.32	66.15	198	132	59.6	17.5	0.51	1.00
10.00	15.12	23.81	SPRT			N/A	60	0.88	1.32	66.15	198	132	59.6	17.5	0.51	1.00
12.50	15.12	23.81	SPRT			N/A	60	0.88	1.32	66.15	198	132	59.6	17.5	0.51	1.00
15.60	15.12	23.81	SPRT			N/A	60	0.88	1.32	66.15	198	132	59.6	17.5	0.51	1.00
19.50	15.12	23.81	SPRT			N/A	60	0.88	1.32	66.15	198	132	59.6	17.5	0.51	1.00
	VCP Time	5.90	min												*worst case	
															includes range averaging	

Table 3.1.4. Recommended test staggered PRT VCP.

In summary, the newly proposed staggered PRT VCP takes about 6 minutes, but brings a significant improvement in terms of mitigation of range and velocity ambiguities. Both maximum unambiguous range and velocity are increased with respect to existing VCPs. In addition, with the implementation of the SACHI filter, ground clutter suppression is operationally acceptable with the exception of eventual velocity catastrophic errors, which may be handled by the ORPG's velocity dealiasing algorithm. All spectral moments meet or exceed WSR-88D System Specification requirements for standard errors of estimates. In fact, errors of reflectivity estimates are significantly better than with the current batch mode.

With appropriate VCPs, staggered PRT can provide significant operational benefits by increasing the range coverage, avoiding aliasing errors, and providing more accurate reflectivity estimates. The price to pay is longer VCP times and the occurrence of catastrophic velocity dealiasing errors, which can be handled in most part by the modified ORPG velocity dealiasing algorithm (Torres et al., 2009).

We recommend that the ROC implements the proposed VCP in a test mode and that more level-I data sets are collected with this VCP. To evaluate the data quality of spectral moment estimates produced with the staggered PRT technique, these real-data cases should be processed end to end; that is, with the recommended SPRT algorithm that includes the SACHI ground clutter filter and the modified ORPG velocity dealiasing algorithm. As future work to support this new VCP, we propose the extension of the SPRT algorithm to recover overlaid echoes and more research towards improving the performance of the SACHI filter.

3.3. Staggered PRT Clutter Filtering

The SPRT algorithm and the Spectral Algorithm for Clutter Harmonics Identification (SACHI) filter have been described in literature and in past NSSL reports. NSSL Report 11 (2007) details the latest updates to the algorithm. This report reflects the findings from simulation analyses of the SACHI filter performance using the SPRT ratio of 2/3.

3.3.1. *Analysis Methodology*

The filter performance is characterized using a MATLAB implementation of the SACHI filter algorithm, where the notch widths are determined with the Gaussian Model Adaptive Processing (GMAP) filter. Simulations of weather and clutter were done using Gaussian power spectra (Sirmans and Bumgarner 1975, Zrnić 1975). To reduce windowing effects and to provide a pseudo-continuous spectrum, the number of spectral coefficients is increased by a factor of three and the resulting time series signal is truncated to create a uniformly spaced signal of the appropriate sample size. The uniformly spaced sampling is then reduced by retaining only those samples in the 2:3 SPRT kernel [10100…]. The statistical performance of the filter is characterized over a range of parameters with one hundred realizations created for each parameter set. Table 3.3.1 provides a summary of simulated parameters.

The parameters in Table 3.3.1 are selected to assess the SACHI filter for WSR-88D operational use at all elevations of volume coverage patterns (VCP); however, additional consideration is given to intermediate an upper elevations where SPRT is expected to replace batch and contiguous Doppler elevations. For this reason, the parameter set reflects VCP 212 with batch and contiguous Doppler waveforms replaced by the SPRT

waveform. The structure of VCP 212 with the lowest intermediate elevation scan (1.8°) and the shortest dwell times provides the most rigorous operational environment for the filter since lower elevations tend to contain higher ground contamination levels and shorter dwell times exhibit the highest error of estimate for the spectral moments.

	Parameter Range
PRT_1 ($PRT_2 = 3*PRT_1/2$)	882 to 2000 μs
Dwell	40 to 100 ms
Signal Power (SNR)	0 to 20 dB
Clutter Power (CSR)	-30 to 100 dB
Velocity	Nyquist co-interval
Spectrum Width	0.1 to 10.0 m/s

Table 3.3.1. Range of parmeters used to evaluate the performance of SACHI.

An example of how VCP 212 is changed to incorporate SPRT is shown in Table 3.3.2. This VCP was implemented as test VCP 14 with RDA Build 11 by ROC personnel. The SPRT waveform in test VCP 14 uses a customized PRT set (Table 3.3.3) to ensure reflectivity and Doppler range coverage is maximized: 450 km for reflectivity and 130 km for Doppler (i.e., velocity and spectrum width) with a maximum ceiling height of 70 kft for both. Additionally, the PRT at the highest elevations of the VCP were limited so that the Nyquist velocity is maintained below 64 m/s to ensure 0.5 m/s velocity resolution using the 8-bit WSR-88D format.

The requirement to provide adequate range coverage means that velocity errors will be high when using the standard dwell times from VCP 212. It can be seen in Table 3.3.2 that the standard errors for the velocities exceed the unfiltered WSR-88D system specification of 1 m/s at all elevations of the SPRT waveform used in test VCP 14. The high errors in velocity are the theoretical errors based on perturbation analysis (e.g. Doviak and Zrnić 1993 equation 6.22a) and are mainly due to the short dwell times used

for the SPRT waveforms. An additional test VCP was implemented in RDA Build 11 as test VCP 15 (Table 3.3.4) that reduces the theoretical velocity errors to the levels required by the WSR-88D system specification. To achieve WSR-88D system specification levels, the dwell times for the SPRT waveform in test VCP 15 range from 70 to 80 ms (i.e., double the dwell times in test VCP 14).

Test VCP 14									
Elevation (deg)	Azimuth Rate (deg/sec)	Dwell (ms)	Samples	PRI	PRT (μs)		WF Type	SD[Z]	SD[V]
					T_1	T_2			
0.5	21.15	47.28	15	1			CS	0.62	
0.5	25.00	40.00	64	8			SZ2		1.07
0.9	21.15	47.28	15	1			CS	0.62	
0.9	25.00	40.00	64	8			SZ2		1.07
1.3	21.15	47.28	15	1			CS	0.62	
1.3	25.00	40.00	64	8			SZ2		1.07
1.8	**24.64**	**40.58**	**18**	**1**	**1740**	**2610**	**STP**	**0.69**	**1.24**
2.4	**26.40**	**37.88**	**20**	**2**	**1617**	**2426**	**STP**	**0.71**	**1.28**
3.1	**26.40**	**37.88**	**20**	**2**	**1617**	**2426**	**STP**	**0.71**	**1.28**
4.0	**26.40**	**37.88**	**20**	**2**	**1617**	**2426**	**STP**	**0.71**	**1.28**
5.1	**28.01**	**35.70**	**20**	**3**	**1494**	**2241**	**STP**	**0.70**	**1.26**
6.4	**28.01**	**35.70**	**24**	**5**	**1248**	**1872**	**STP**	**0.70**	**1.30**
8.0	**28.40**	**35.21**	**30**	**6**	**1125**	**1688**	**STP**	**0.71**	**1.35**
10.0	**28.88**	**34.62**	**36**	**8**	**882**	**1323**	**STP**	**0.69**	**1.41**
12.5	**28.74**	**34.79**	**36**	**8**	**882**	**1323**	**STP**	**0.69**	**1.41**
15.6	**28.74**	**34.79**	**36**	**8**	**882**	**1323**	**STP**	**0.69**	**1.41**
19.5	**28.74**	**34.79**	**36**	**8**	**882**	**1323**	**STP**	**0.69**	**1.41**

Table 3.3.2. Test VCP 14. PRI is the Pulse Repetition Interval, where the PRI numbers are indexes into a standard table of pulse repetition times (PRT) used within the VCP. For SPRT, the PRI is a reference to the shortest PRT (T_1). The RDA control software calculates the long PRT based on the 2:3 ratio for SPRT. T_1 is the short PRT and T_2 is the long PRT of the SPRT waveform (2:3 ratio). WF Type is the waveform type, where CS stands for contiguous surveillance, SZ2 for Sachidananda-Zrnić (8/64 phase code) with two sweeps, and STP for SPRT. SD[Z] and SD[V] are the standard deviations of reflectivity and velocity estimates, respectively.

PRI	T_1 (μs)	T_2 (μs)
1	1740	2610
2	1617	2426
3	1494	2241
4	1371	2057
5	1248	1872
6	1125	1688
7	1002	1503
8	882	1323

Table 3.3.3. SPRT PRI table.

Test VCP 15									
Elevation (deg)	Azimuth Rate (deg/sec)	Dwell (ms)	Samples	PRI	PRT (μs)		WF Type	SD[Z]	SD[V]
					T_1	T_2			
0.5	21.15	47.28	15	1			CS	0.62	
0.5	25.00	40.00	64	8			SZ2		1.07
0.9	21.15	47.28	15	1			CS	0.62	
0.9	25.00	40.00	64	8			SZ2		1.07
1.3	21.15	47.28	15	1			CS	0.62	
1.3	25.00	40.00	64	8			SZ2		1.07
1.8	**12.30**	**81.30**	**37**	**1**	**1740**	**2610**	**STP**	**0.49**	**0.85**
2.4	**13.20**	**75.76**	**37**	**2**	**1617**	**2426**	**STP**	**0.50**	**0.88**
3.1	**13.20**	**75.76**	**37**	**2**	**1617**	**2426**	**STP**	**0.50**	**0.88**
4.0	**13.20**	**75.76**	**37**	**2**	**1617**	**2426**	**STP**	**0.50**	**0.88**
5.1	**14.01**	**71.38**	**38**	**3**	**1494**	**2241**	**STP**	**0.52**	**0.92**
6.4	**14.01**	**71.38**	**45**	**5**	**1248**	**1872**	**STP**	**0.50**	**0.92**
8.0	**14.20**	**70.42**	**50**	**6**	**1125**	**1688**	**STP**	**0.50**	**0.94**
10.0	**14.44**	**69.25**	**62**	**8**	**882**	**1323**	**STP**	**0.50**	**1.00**
12.5	**14.37**	**69.59**	**63**	**8**	**882**	**1323**	**STP**	**0.50**	**1.00**
15.6	**14.37**	**69.59**	**63**	**8**	**882**	**1323**	**STP**	**0.50**	**1.00**
19.5	**14.37**	**69.59**	**63**	**8**	**882**	**1323**	**STP**	**0.50**	**1.00**

Table 3.3.4. Test VCP 15.

3.3.2. *Clutter Suppression Requirements*

The SACHI filter was compared against requirements detailed in the WSR-88D System Specifications 2810000H dated 25 April 2008, chapter 3.7.2.7 *Ground Clutter Suppression*. Although the system specification includes filter requirements for dual

polarization, only the single-polarization requirements for reflectivity, velocity, and spectrum width are assessed in this report.

It is noted that the WSR-88D System Specification (SS) is written for an infinite-impulse-response (IIR) filter with selectable notch widths; thus, some of the specifications do not apply to frequency domain filters using automatic adaptable notch widths (Ice et. al. 2004). Additionally, the SACHI filter is intended to be employed with the SPRT waveform at elevations that will replace batch and contiguous Doppler waveforms. In this regime, the clutter contamination is expected to be reduced to power levels several orders of magnitude lower than at the lowest elevations for which the system specification is written. Nonetheless, the evaluation characterizes the SACHI filter performance toward meeting the clutter filter requirements listed in the WSR-88D SS.

The goal of ground clutter filtering is to remove the effects of ground clutter bias on reflectivity, velocity, and spectrum width while providing meaningful estimates of these moments (i.e., small errors of estimates). To that end, the WSR-88D SS provides bias and standard deviation requirements for the application of a filter for a signal at 20 dB signal-to-noise ratio (SNR) with a weather signal spectrum width of 4 m/s. Clutter model A of the WSR-88D SS provides for a zero-mean normally distributed clutter model and is most relevant for this ground clutter filter evaluation. Although not specified in the WSR-88D SS, a 0.28 m/s clutter spectrum width is used for this evaluation which is in line with the expected clutter spectrum width of 0.1 m/s when accounting for spectrum broadening due to the antenna motion. Additionally, 0.28 m/s clutter spectrum width provides ready

comparison with earlier filter evaluations conducted for the WSR-88D system at the Radar Operation Center (e.g. Sirmans 1992, Sirmans et. al. 2003, and Ice et. al. 2004).

When applied, the filter is required to provide a clutter suppression capability of 30 dB in the reflectivity channel and selectable clutter suppression levels from 20 dB to 50 dB in the Doppler channel (velocity and spectrum width), where clutter suppression is defined as the ratio of the input power to the output power after application of the clutter filter. As mentioned earlier, the SACHI filter does not have a selectable notch width; however, the filter does utilize the same adaptable notch width scheme currently used by the GMAP filter in the WSR-88D system.

The bias in the spectral moments caused by the application of the filter is assessed with a signal-to-clutter ratio (SCR) of 30 dB. In the bias assessment, the low clutter level with high signal level is used so that the prominent contributor to the moment bias is associated with the filter performance and not due to clutter residue. An additional allowance in moment bias is provided in the WSR-88D SS when clutter residue is present in the output signal: reflectivity bias of 1 dB for an output SCR of 10 dB, velocity bias of 1 m/s for an output SCR of 11 dB, and spectrum width bias of 1 m/s for an output SCR of 15 dB.

The filtered reflectivity bias requirement is assessed with a weather signal at 0 m/s and is dependent on the spectrum width of the weather signal as shown in Table 3.3.5 (reproduced from the WSR-88D SS). As can be seen in this table, the bias in reflectivity is expected to increase as the weather spectrum width becomes small compared to the notch width of the clutter filter. The bias in reflectivity is due to portions of the weather

signal coincident with the notch width of the filter centered at 0 m/s. When the weather signal is completely contained within the notch width of the filter, the entire weather signal moments are likely to be unrecoverable (i.e., they are severely biased).

Weather Spectrum Width (m/s)	Maximum Bias of Reflectivity (dB)
1	10
2	2
≥3	1

Table 3.3.5. WSR-88D filtered reflectivity bias requirements.

The filtered Doppler moments have a bias requirement of less than 2 m/s over a range of usable velocities as a function of the notch width selection as shown in Table 3.3.6 (reproduced from the WSR-88D SS). As mentioned earlier, this requirement is for an IIR filter with selectable notch widths. The WSR-88D system no longer uses an IIR filter; however, filtered velocity and spectrum width bias and standard deviation can be assessed to ensure 2 m/s is not exceeded for all usable velocities above those minimums stated on the left side of Table 3.3.6 when the filter provides the clutter suppression level listed on the right side of the table.

Minimum Usable Velocity (m/s)	Notch Width Clutter Suppression Selection (dB)
2	20
3	28
4	50

Table 3.3.6. WSR-88D usable filtered velocity requirements.

3.3.3. *Overview of SACHI Filter*

The SACHI filter operates in the frequency domain and provides both filtering and velocity dealiasing functionality. A set of non-uniform digitized receiver pulses (staggered PRT with a 2:3 ratio) are ingested into the algorithm and the filtered

reflectivity, filtered/dealiased velocity, and filtered spectrum width base moments are provided. Unlike signals sampled uniformly where clutter and weather signals overlap in one velocity region centered on 0 m/s, the 2:3 SPRT sampling creates five distinct clutter and weather signal overlap regions. Thus, the SACHI filter must provide filtering in these five distinct velocity regions. The velocity regions for the 2:3 SPRT ratio are located at the normalized extended Nyquist intervals of 0, ±0.4, and ±0.8 as shown in Fig. 3.3.1. The relative clutter power amplitudes of each clutter spectral replica of a SPRT signal compared to the uniformly sampled clutter signal are given by the Discrete Fourier Transform (DFT) of the code kernel [10100] as -3.98 dB for a normalized velocity of 0 (-14.18 dB for ±0.4 and -5.82 dB for ±0.8).

The spectral overlap of weather and clutter is readily seen by examining the Doppler spectra after performing the Discrete Fourier Transform (DFT) on the reconstructed uniform sampling of the SPRT waveform. The reconstruction is accomplished by inserting zeros between the SPRT samples as shown in NSSL report 11 (Torres et. al. 2007). In Fig. 3.3.1, the Doppler spectrum of weather and clutter are plotted along the y-axis in decibels-milliwatts (dBm) against the normalized extended Nyquist velocity (v/v_a) on the x-axis. For this example, the weather has a SNR of 20 dB with velocity at $-v_a/2$ and spectrum width of 1 m/s where v_a is the extended Nyquist velocity. The clutter power is 30 dB stronger than the weather signal, its mean velocity is 0 m/s, and its spectrum width is 0.28 m/s. In the uniform sampling of the composite signal (dotted black line), the weather and clutter signals are clearly distinguishable from each other because they are sufficiently separated in velocity. In the SPRT composite signal (blue line), four replicas of clutter signal are centered at 0, ±0.4, and ±0.8 (normalized velocity) and the weather

signal replicas are centered at -0.9, -0.5, -0.1, 0.3, and 0.7 given by the aliased velocities from the equation: $-0.5+(0,\pm 0.4,\pm 0.8)$. The SPRT Doppler spectrum of the clutter signal (red line) and the weather signal (green line) are plotted separately to show the relative amplitudes of each signal replica. In Fig. 3.3.1, the largest weather replica is at $-v_a/2$; whereas, the largest clutter replica is centered at 0 m/s.

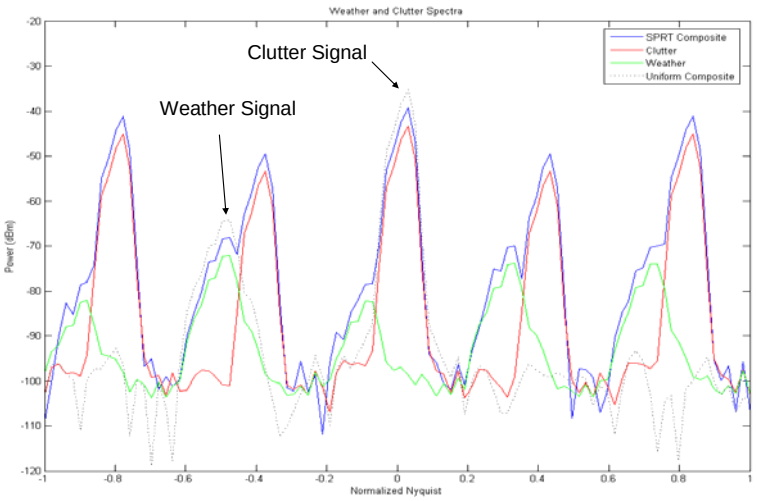

Fig. 3.3.1. Example of weather and clutter spectra in SPRT.

3.3.4. *SACHI Filter Performance*

a) Reflectivity Clutter Suppression and Bias Analysis

In Fig. 3.3.2, two scatter plots showing filtered power bias as a function of input clutter-to-signal ratio (CSR) demonstrate the clutter suppression performance of the SACHI filter. The input CSR levels are -30 dB and 0 dB to 70 dB in 5 dB steps. At each CSR level, results from 100 realizations are shown. The color scales represent the percentage of occurrences at each power bias level, with the maroon indicating 100% (100 occurrences) and white indicating 0% (0 occurrences). Optimal clutter suppression

performance of the filter is achieved when the power bias is at 0 dB. Clutter residue is present when the power bias increases above 0 dB; while, over-suppression occurs when the power bias drops below 0 dB. In each scatter plot, high occurrences (>90%) are seen along the zero power bias and occurrences quickly tapper to near zero on either side of zero power bias. The clutter suppression performance of the tested filter can be estimated at the point where the highest occurrence of power bias (blue line) departs from zero power bias. For the examples in Fig. 3.3.2, clutter suppression is assessed at about 50 dB in the graph on the left; whereas clutter suppression is assessed at about 10 dB in the graph on the right. A complete summary of maximum clutter suppression levels based on power bias requirements is shown in Table 3.3.7.

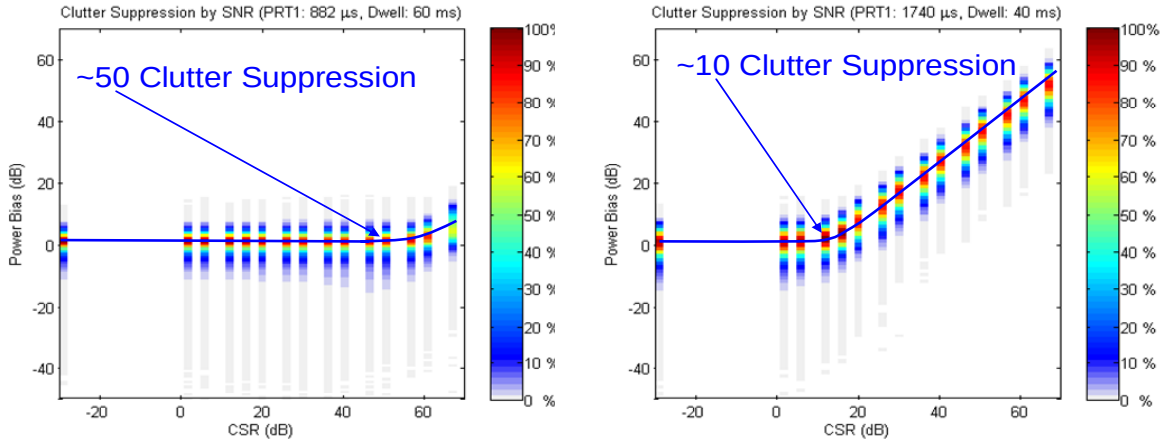

Fig. 3.3.2. Examples of assessment of clutter suppression from the power bias plots.

T_1 (μs)		882	1002	1125	1248	1371	1494	1617	1740	2000
v_a (m/s)		61	53	48	43	39	36	33	31	27
$r_{a,D}$ (km)		132	150	169	187	206	224	242	261	300
$r_{a,S}$ (km)		198	225	253	281	308	336	364	391	450
Dwell (ms)	40	50	40	40	40	40	40	10	10	10
	44	50	50	40	35	40	40	40	35	10
	48	50	50	50	35	35	35	40	35	10
	52	50	50	50	50	35	35	35	35	35
	56	50	50	50	50	50	35	35	35	35
	60	50	50	50	50	50	50	30	35	30
	64	55	50	50	50	50	50	30	30	30
	68	55	55	50	50	50	50	50	30	30
	72	55	55	50	50	50	45	50	50	25
	76	55	55	55	50	50	50	50	50	25
	80	55	55	55	50	50	50	50	50	50
	84	55	55	55	55	50	50	50	45	50
	88	55	55	55	55	50	50	50	50	50
	92	55	55	55	55	55	50	45	50	45
	98	55	55	55	55	55	50	50	50	45
	100	55	55	55	55	55	55	50	50	50

Table 3.3.7. Maximum clutter suppression based on power bias requirements.

In Table 3.3.7, parameters for a 2:3 ratio SPRT waveform are displayed with the shortest PRT (T_1) listed at the top. For convenience, the extended Nyquist (v_a), the Doppler unambiguous range ($r_{a,D}$) and the reflectivity unambiguous range ($r_{a,S}$) are shown. The clutter suppression levels in the table represent zero mean-power bias, which includes power bias estimates for all velocities above 4 m/s. The colors in the table indicate three levels of clutter suppression: green for clutter suppression greater than 50 dB, yellow for clutter suppression between 30 and 50 dB, and red for clutter suppression below 30 dB. It is shown that the WSR-88D reflectivity bias requirement for 30 dB of clutter suppression is met for all boxes colored green and yellow. Matching clutter suppression levels in Table 3.3.7 with SPRT waveforms in Table 3.3.4 reveals that the WSR-88D clutter suppression requirement is met for all SPRT elevations in test VCP 15. Although not

shown in Table 3.3.7, clutter suppression requirements would not be met for test VCP 14 (Table 3.3.2) for SPRT waveforms below the 6.4° elevation (i.e., elevations between 1.8° and 5.1°). In general, clutter suppression performance of the filter degrades for shorter dwell times and/or longer PRTs. As seen in Table 3.3.7, for a dwell time of 40 ms, T_1 must be shorter than 1617 μs to achieve 30 dB of clutter suppression. The anomalous behavior within the table (e.g., decreased clutter suppression of T_1 at 2000 μs with increasing dwell times), where the clutter suppression level seems to contradict the previous generality is attributed to the CSR step sizes used in generating the statistics for the table rather than the performance of the SACHI filter.

Another measure of SACHI filter performance is seen when compared to current (GMAP) and past (IIR) filters used in the WSR-88D system (legacy and GMAP data are repeated from Ice et al. 2004). The comparisons are made in Surveillance, Clear Air and Doppler weather modes which make up the VCP scanning strategies employed on the WSR-88D system for both precipitation and clear air operations. Although the SPRT waveform is not currently planned for use in the Surveillance and Clear Air weather modes, it is instructive to make these comparisons for future considerations.

i) Surveillance Mode

In the Surveillance mode, long PRTs (~3000 μs) are used to sample the convective environment at low elevation angles providing reflectivity coverage of about 450 km. The unambiguous range for reflectivity is established by the relationship $cT_2/2$, where the specific values for test VCP 14 and 15 are listed in Tables 3.3.2 and 3.3.4, respectively. To meet the reflectivity unambiguous range of 450 km, a 2:3 ratio SPRT Surveillance

mode will need to use a T_2 of 3000 μs (T_1 of 2000 μs). Fig. 3.3.3 shows the reflectivity bias of all three filters (legacy IIR, GMAP, and SACHI) in the Surveillance weather mode as a function of the true spectrum width.

The reflectivity bias requirements from Table 3.3.5 are plotted in Fig. 3.3.3 as blue circled x's to provide easy reference to the WSR-88D requirements. The composite weather and clutter signal input parameters are described in Table 3.3.5. The legacy IIR filter is shown with three notch width suppression levels: high (blue), medium (green) and low (orange) (e.g., Sirmans 1992). The GMAP filter (magenta) is displayed with the operationally used clutter spectrum seed width of 0.4 m/s using a PRF of 322 Hz and 16 samples (a dwell of approximately 50 ms) (e.g., Ice et al. 2004). It is seen that the SACHI filter meets the reflectivity bias levels down to about a 2 m/s true spectrum width and has performance comparable to the GMAP filter in the Surveillance mode. Referring back to the last column of Table 3.3.7, the clutter suppression levels are shown to meet WSR-88D requirements for dwell times above 48 ms (except as noted for the anomalous estimates at 72 ms and 76 ms) in the Surveillance mode.

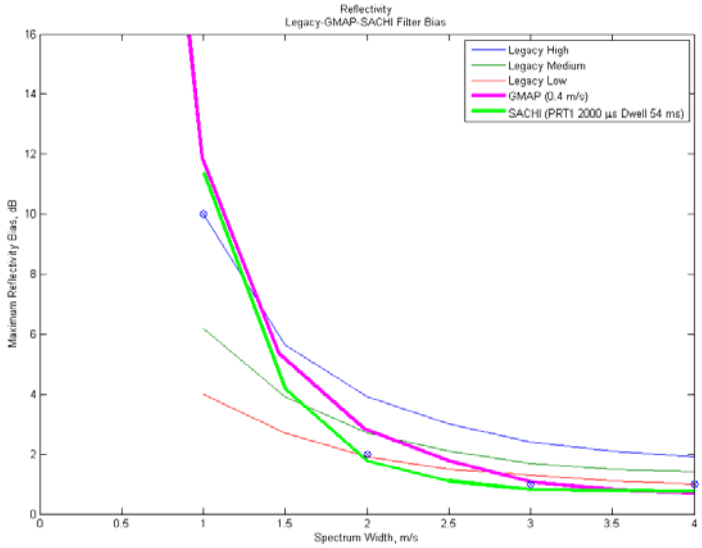

Fig. 3.3.3. Maximum reflectivity bias in Surveillance Mode.

ii) Clear Air Mode

The Clear Air mode is used when expected precipitation is low and provides increased sensitivity for low signal detection (FMH-11). The WSR-88D has two VCP definitions for the Clear Air mode: VCP 31 (long pulse width) and VCP 32 (short pulse width). The filter evaluation was performed only for the short pulse width of VCP 32. The plots in Fig. 3.3.4 provide a ready comparison of the reflectivity bias for both the SACHI filter (green) and the GMAP filter (magenta) as the true spectrum width ranges from about 1 m/s to 4 m/s. For the GMAP filter, the signal PRF is 450 Hz (a PRT of about 2222 µs) with 64 samples (a dwell time of about 142 ms). For the SACHI filter, T_2 is 2241 µs with a dwell of 82 ms. In the Clear Air mode, the SACHI filter is seen to meet the reflectivity bias requirements of the WSR-88D SS down to a spectrum width of about 1 m/s and has comparable performance to the GMAP filter. Note that the SACHI filter should have improved performance in VCP 32 over those displayed in Fig. 3.3.4 since dwell times for VCP 32 are much longer than used to create the figure.

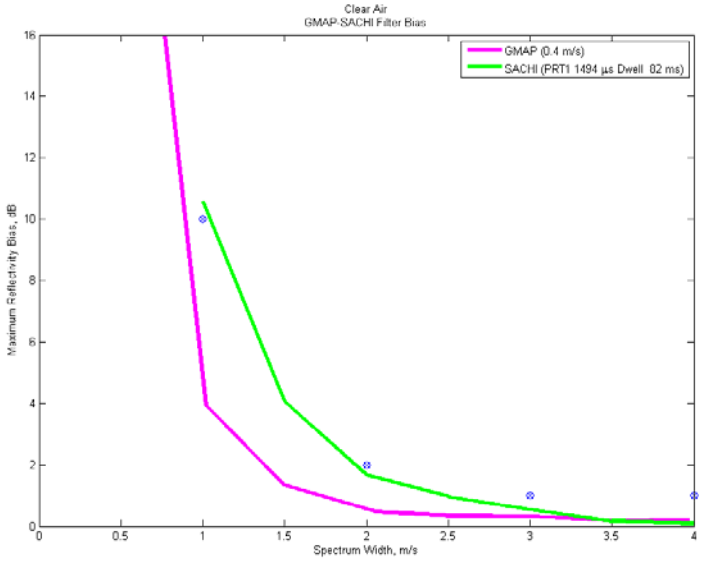

Fig. 3.3.4. Maximum reflectivity bias in Clear Air Mode.

iii) Doppler Mode

In the Doppler mode, shorter PRTs are used to extend the Nyquist interval; however, the unambiguous range is reduced making overlaid echoes likely at the lowest elevations levels of the VCP. In the intermediate and upper elevations, storm tops heights of 70 kft are quickly reached because of the earth's curvature, eliminating the concern for overlaid echoes since storm tops above this height are rare. At the intermediate and upper elevations of the VCP, the SPRT waveform allows additional increase in the Nyquist interval for the same coverage region as are experienced by either batch or Doppler waveforms.

Fig. 3.3.5 shows reflectivity bias as a function of true spectrum width for legacy IIR, GMAP, and SACHI filters. As in the Surveillance mode, the legacy IIR filter has selections for high, medium, and low notch widths. The GMAP filter is supplied a signal with a PRF of 1000 Hz (a PRT of 1000 µs) with 64 samples (a 64 ms dwell time) and the

SPRT waveform is supplied a signal with a T_1 of 1002 μs and a dwell time of 64 ms. All other weather signal and clutter parameters are detailed in section 3.3.1. The SACHI filter is shown to provide performance comparable to the GMAP filter. For this example, the SPRT waveform provides the same range coverage in the Doppler channel while doubling the Nyquist interval. The clutter suppression levels exhibited by the SACHI filter in the Doppler mode exceed the WSR-88D SS requirements of 30 dB for a T_1 of 1002 μs as shown in Table 3.3.7. Although the reflectivity bias (shown in Fig. 3.3.5) is slightly over the WSR-88D SS requirement for this example, better filter performance can be realized when using the longer dwell times of test VCP 15 detailed in Table 3.3.4.

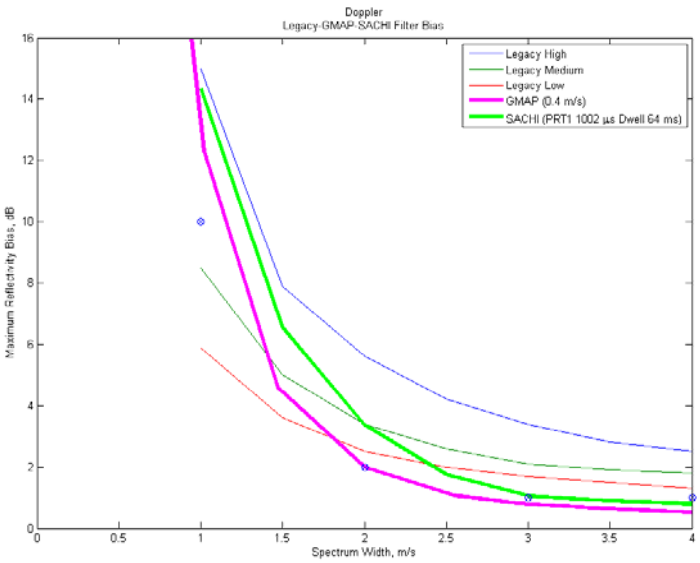

Fig. 3.3.5. Maximum reflectivity bias in Doppler Mode.

b) Velocity Clutter Suppression and Bias Analysis

If ground clutter is not removed from the composite signal, it biases the weather velocity estimate toward zero while the power (reflectivity) is increased by the amount of clutter power present in the composite signal. The weather signal velocity estimate can still be

biased toward zero even after filtering when enough ground clutter remains in the signal at the output of the filter. If all or part of the weather signal is in the filter stopband, the estimates of weather signal velocities and power may be unrecoverable or severely biased. As mentioned in section 3.3.3, the SACHI filter has five stopband velocity regions at 0, ±0.4, and ±0.8 of the normalized extended Nyquist co-interval. The WSR-88D SS provides guidance for a single static stopband at 0 m/s, but does not address multiple dynamic stopbands.

In Fig. 3.3.6, the power bias is shown for a narrow weather signal (i.e., a 1 m/s spectrum width). The weather signal has an SNR of 20 dB with a 1 m/s spectrum width, and the clutter signal has a SCR of 30 dB with a 0.28 m/s spectrum width. T_1 is set to 882 μs with a 40 ms dwell time. The filtered weather power bias is evaluated at 50 velocities across the Nyquist co-interval. For this example, the power bias (mean of 100 realizations) of a narrow weather signal is shown to emphasize the effect when the weather signal is in the filter stopband. The stopband of the SACHI filter is dynamically determined by GMAP. We can see that the power biases displayed in Fig. 3.3.2 meet the WSR-88D reflectivity bias requirement of 10 dB (Table 3.3.5) for a weather signal at 0 m/s velocity with a 1 m/s spectrum width. Note that all other power bias levels are within 2 dB once the weather signal is out of the stop band of the filter centered at 0 m/s.

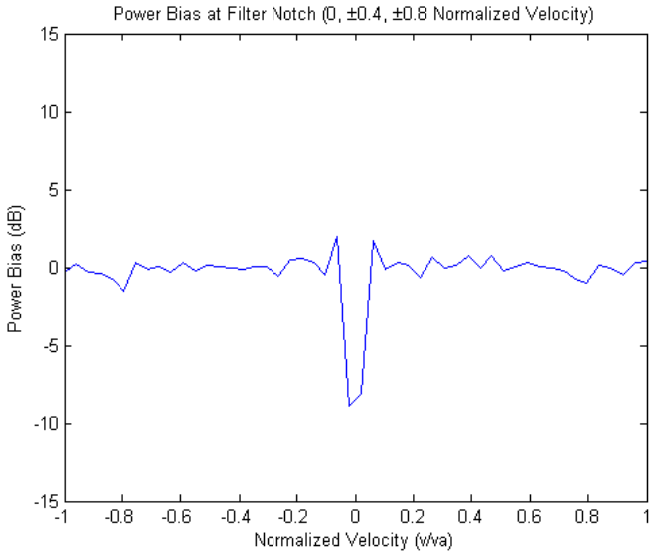

Fig. 3.3.6. Power bias for a narrow weather signal with a 1 m/s spectrum width and a CSR of -30 dB (no clutter).

As seen in Fig. 3.3.7, the weather power bias at the five stopband velocity regions of the SACHI filter are strongly affected by the filtering process in the presence of clutter. For this example, the narrow weather signal is completely contained in the dynamically controlled stopband of the filter, and the clutter signal has been increased to a CSR of 45 dB. The notch widths at 0 and ±0.8 exceed a power bias of 5 dB, with the region near 0 m/s exhibiting the largest power bias of nearly 10 dB. This example shows that the filter is over-suppressing the weather signal at the filter notch widths.

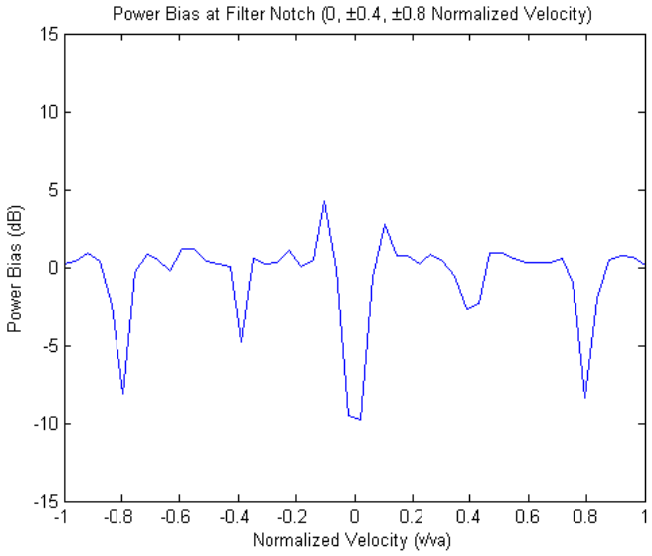

Fig. 3.3.7. Power bias for a narrow weather signal with a 1 m/s spectrum width and a CSR of 45 dB (strong clutter).

Recall that the WSR-88D velocity requirements listed in Table 3.3.6 are for a single stopband filter that has selectable clutter suppression levels between 20 and 50 dB. The intent is to provide usable velocities in the passband of such filter. Usable velocities in the passband of the filter should result in power biases less than 2 dB (3 dB with clutter residue). Usable velocities will exhibit biases less than 2 m/s (3 m/s with clutter residue) and standard deviations less than 2 m/s (no additional allowance for clutter residue). It may be instructive to impose the "usable velocities" rules in the regions of the SACHI filter that are outside the central stop band at 0 m/s velocity (i.e., ±0.4 and ±0.8 velocities normalized to the extended Nyquist interval). To do so requires revisiting the clutter suppression levels shown in Table 3.3.7 with these additional constraints. In Tables 3.3.8 and 3.3.9 are the clutter suppression levels that meet the usability rules of Table 3.3.6 for velocities above 4 m/s. The tables show the same parameters as Table 3.3.7 with T_1 at the top.

The high clutter suppression requirement (50 dB) for usable velocities above 4 m/s is highlighted in Table 3.3.8 using the green color. We see that the usable velocity requirement imposes longer dwell times over Table 3.3.7. For example, the 882 μs T_1 requires dwell times above 80 ms to achieve the velocity bias and standard deviation of 2 m/s in a high clutter environment.

T_1 (μs)		882	1002	1125	1248	1371	1494	1617	1740	2000
v_a (m/s)		61	53	48	43	39	36	33	31	27
$r_{a,D}$ (km)		132	150	169	187	206	224	242	261	300
$r_{a,S}$ (km)		198	225	253	281	308	336	364	391	450
Dwell (ms)	40	40	10	25	0	0	0	-30	-30	-30
	44	40	30	25	25	-30	-30	-30	-30	-30
	48	40	40	30	25	15	-30	-30	-30	-30
	52	40	30	35	10	20	-30	-30	-30	-30
	56	40	40	40	15	20	10	-30	-30	-30
	60	45	40	30	40	15	15	-30	-30	-30
	64	45	40	40	25	35	10	0	10	-30
	68	45	40	40	20	30	35	20	-30	-30
	72	45	45	40	35	25	15	10	-30	0
	76	45	45	45	45	25	20	15	5	-30
	80	45	45	45	40	35	15	10	0	-30
	84	50	45	45	35	40	20	15	5	-30
	88	50	50	45	45	40	30	15	15	-30
	92	50	50	45	45	35	35	20	5	0
	98	50	50	50	45	40	40	20	20	-30
	100	50	50	45	45	40	25	25	15	-30

Table 3.3.8. Maximum clutter suppression based on velocity requirements for high-suppression clutter filtering.

Recall that the clutter power is expected to be reduced substantially as the radar scans at higher elevation angles. Conversely, clutter suppression requirements are higher at the lowest elevations where longer PRTs are needed for radar coverage. The clutter suppression capability of the SACHI filter is limited at the longer PRTs, making clutter residue more likely in the output of the filter. Shown in Table 3.3.9 are the high clutter suppression values for velocities above 4 m/s when allowing for clutter residue with 3 dB

power bias and 3 m/s velocity bias. The SACHI filter is capable of providing a clutter suppression of about 35 dB (80 ms dwell time) when clutter residue is present in the output of the filter for test VCP 15 (Table 3.3.4) at the 1.8° elevation where the SPRT waveform replaces the batch waveform. This may not be a serious operational limitation since ground clutter contamination at 1.5° elevations and above is expected to be acquired through contact with the antenna side lobes which provide an additional two-way clutter isolation of about 55 dB (Sirmans 1992). For the batch waveforms, clutter suppression performance of the SACHI filter in the Doppler channel is comparable to the step-initialized IIR filter (i.e., about 35 dB) and inferior to the GMAP filter (i.e., about 55 dB) (e.g., Sirmans 1992, Ice et al. 2004).

T_1 (μs)		882	1002	1125	1248	1371	1494	1617	1740	2000
v_a (m/s)		61	53	48	43	39	36	33	31	27
$r_{a,D}$ (km)		132	150	169	187	206	224	242	261	300
$r_{a,S}$ (km)		198	225	253	281	308	336	364	391	450
Dwell (ms)	40	40	30	30	5	0	0	-30	0	0
	44	40	40	30	30	25	0	0	5	-30
	48	40	40	40	30	25	5	0	0	0
	52	40	35	40	40	25	20	5	-30	0
	56	45	40	40	35	40	25	25	20	25
	60	45	40	35	40	30	20	20	20	0
	64	45	45	40	40	35	25	15	15	5
	68	45	45	45	35	40	40	20	15	-30
	72	45	45	45	40	35	35	20	15	10
	76	45	50	45	45	45	35	40	10	15
	80	45	50	45	45	45	40	40	35	30
	84	50	50	50	45	45	40	30	35	40
	88	50	50	50	45	45	40	20	40	40
	92	50	50	50	45	45	40	40	35	5
	98	50	50	50	50	45	40	35	40	25
	100	50	50	50	50	45	45	45	25	40

Table 3.3.9. Maximum clutter suppression based on velocity requirements for high-suppression clutter residue.

SACHI filter performance with clutter residue for medium (28 dB for usable velocities above 3 m/s) and low (20 dB for usable velocities above 2 m/s) clutter suppression levels are shown in Tables 3.3.10 and 3.3.11, respectively. Shorter dwell times can be utilized when these clutter suppression levels are required. In both the medium and low clutter environments, the SACHI filter meets the WSR-88D SS requirements at all elevations in test VCP 15 for those usable velocities indicated in Table 3.3.6.

T_1 (μs)		882	1002	1125	1248	1371	1494	1617	1740	2000
v_a (m/s)		61	53	48	43	39	36	33	31	27
$r_{a,D}$ (km)		132	150	169	187	206	224	242	261	300
$r_{a,S}$ (km)		198	225	253	281	308	336	364	391	450
Dwell (ms)	40	30	30	30	30	30	5	0	0	-30
	44	30	30	30	30	30	5	5	5	-30
	48	30	30	30	30	30	30	5	5	-30
	52	30	30	30	30	30	30	30	5	-30
	56	30	30	30	30	30	30	30	25	-30
	60	30	30	30	30	30	30	30	25	-30
	64	30	30	30	30	30	30	30	25	-30
	68	30	30	30	30	30	30	30	25	0
	72	30	30	30	30	30	30	30	30	15
	76	30	30	30	30	30	30	30	30	15
	80	30	30	30	30	30	30	30	30	30
	84	30	30	30	30	30	30	30	30	15
	88	30	30	30	30	30	30	30	30	30
	92	30	30	30	30	30	30	30	30	30
	98	30	30	30	30	30	30	30	30	30
	100	30	30	30	30	30	30	30	30	30

Table 3.3.10. Maximum clutter suppression based on velocity requirements for medium-suppression clutter filtering.

T_1 (μs)		882	1002	1125	1248	1371	1494	1617	1740	2000
v_a (m/s)		61	53	48	43	39	36	33	31	27
$r_{a,D}$ (km)		132	150	169	187	206	224	242	261	300
$r_{a,S}$ (km)		198	225	253	281	308	336	364	391	450
Dwell (ms)	40	20	20	20	20	5	5	0	0	-30
	44	20	20	20	20	20	5	5	5	-30
	48	20	20	20	20	20	20	5	5	-30
	52	20	20	20	20	20	20	20	5	-30
	56	20	20	20	20	20	20	20	20	-30
	60	20	20	20	20	20	20	20	20	0
	64	20	20	20	20	20	20	20	20	0
	68	20	20	20	20	20	20	20	20	0
	72	20	20	20	20	20	20	20	20	20
	76	20	20	20	20	20	20	20	20	15
	80	20	20	20	20	20	20	20	20	20
	84	20	20	20	20	20	20	20	20	15
	88	20	20	20	20	20	20	20	20	20
	92	20	20	20	20	20	20	20	20	20
	98	20	20	20	20	20	20	20	20	20
	100	20	20	20	20	20	20	20	20	20

Table 3.3.11. Maximum clutter suppression based on velocity requirements for low-suppression clutter filtering.

c) Velocity Dealiasing

We note at this point that the SACHI filter provides velocity dealiasing as well as clutter filtering. Dealiasing is accomplished by reconstructing the uniform time series (inserting zeroes) from the SPRT samples; then, removing the effects of the code kernel [10100] from the reconstructed spectra of the filtered weather signal using magnitude deconvolution. The process of dealiasing using magnitude deconvolution is limited to "narrow" spectrum widths to ensure the weather spectrum does not "impinge" on adjacent replicas in the extended SPRT Nyquist co-interval. The spectrum is considered "narrow" if the spectral spread of the weather signal is less than a fifth of the extended

Nyquist co-interval with a PRT ratio of 2:3. The "narrow" spectrum width constraint is shown in Table 3.3.12 to confidence levels from 68.3% to 100% (1 to 4 standard deviations for a Gaussian weather signal). The table shows the extended Nyquist velocity (m/s) that is required to achieve the "narrow" spectrum width constraint for different values of the weather signal spectrum width. For example, a spectrum width of 4 m/s is "narrow" for a 2:3 SPRT waveform with T_1 of 1371 μs (Nyquist velocity of 39 m/s) to about a 95.4% confidence level.

Confidence / σ_v (m/s)	68.3%	95.4%	99.7%	100%
1	5	10	15	20
2	10	20	30	40
3	15	30	45	60
4	20	40	60	80
5	25	50	75	100
6	30	60	90	120
7	35	70	105	140
8	40	80	120	160
9	45	90	135	180
10	50	100	150	200

Table 3.3.12. "Narrow" spectrum width constraint for 2:3 SPRT waveform.

An additional consideration on the filter dealiasing performance is the amount of spectral spread of the clutter signal since the clutter signal has a "very narrow" spectrum width: 0.1 m/s to 0.3 m/s with 0 m/s mean velocity (Sirmans 1992). Because not all clutter spectral components are periodic, the discrete Fourier transform spreads the clutter across the entire Nyquist co-interval. Further, concentration of clutter power in such a small band of frequencies results in large bias contributions to spectral components far removed from 0 m/s. In the SPRT spectrum this means that the five clutter spectra overlap when the clutter power becomes moderately large. Additionally, shorter dwell times and/or

longer PRTs result in larger clutter power contributions to all spectral coefficients of the discrete Fourier transform. Data windowing constrains the clutter spectral spread to a large degree, but eventually the dealiasing performance degrades for large clutter powers, short dwell times, and long PRTs. Fig. 3.3.8 shows filtered velocity biases as a function of the true velocity. Superimposed on the scatter plot is a density cloud of the scatter plot. The scatter plot shows the bias of 100 velocity estimates (red dots) for each true velocity input. The density cloud depicts how the scattered velocity biases group together in regions. The density cloud color scale ranges from red (50% occurrence) to white (0% occurrence). In Fig. 3.3.8a (top row), T_1 is increased from 882 μs (left) to 1371 μs (middle) to 1740 μs (right). For T_1 of 882 μs, the velocity bias is 0 m/s with few occurrences of dealiasing errors. The dealiasing errors increase at 1371 μs for T_1 as seen by the accumulation of scattered estimates in regions above and below the notches of the filter. At 1740 μs for T_1, the estimated velocities are dominated by clutter which biases the velocity estimate to 0 m/s (i.e., the velocity bias mirrors the true velocity). In Fig. 3.3.8b (middle row), the effects of increased dwell time are shown to improve the velocity dealiasing performance. Here, T_1 of 1371 μs and CSR of 40 dB are held constant while the dwell time increases from 40 ms (left) to 60 ms (middle) to 100 ms (right). The WSR-88D system requirements for velocity bias and standard deviation are met for the bottom row of plots (Fig. 3.3.8c), where the CSRs reported in Table 3.3.8 for T_1 of 1371 μs at dwell times of 40 ms (left) to 60 ms (middle) to 100 ms (right) are shown.

It is evident that the velocity dealiasing performance degrades for velocities near the filter notches as seen in Fig. 3.3.8b (left plot) for the velocities of 0, ±15.6, and ±31.2 m/s for T_1 equal to 1371 μs. The degradation in velocity dealiasing is experienced before the

clutter suppression performance becomes unusable, as seen by comparing Fig. 3.3.8c (left plot) and 3.3.8b (left plot). This velocity dealiasing degradation is seen when comparing clutter suppression levels shown in Table 3.3.7 with those shown in Tables 3.3.8 through 3.3.11.

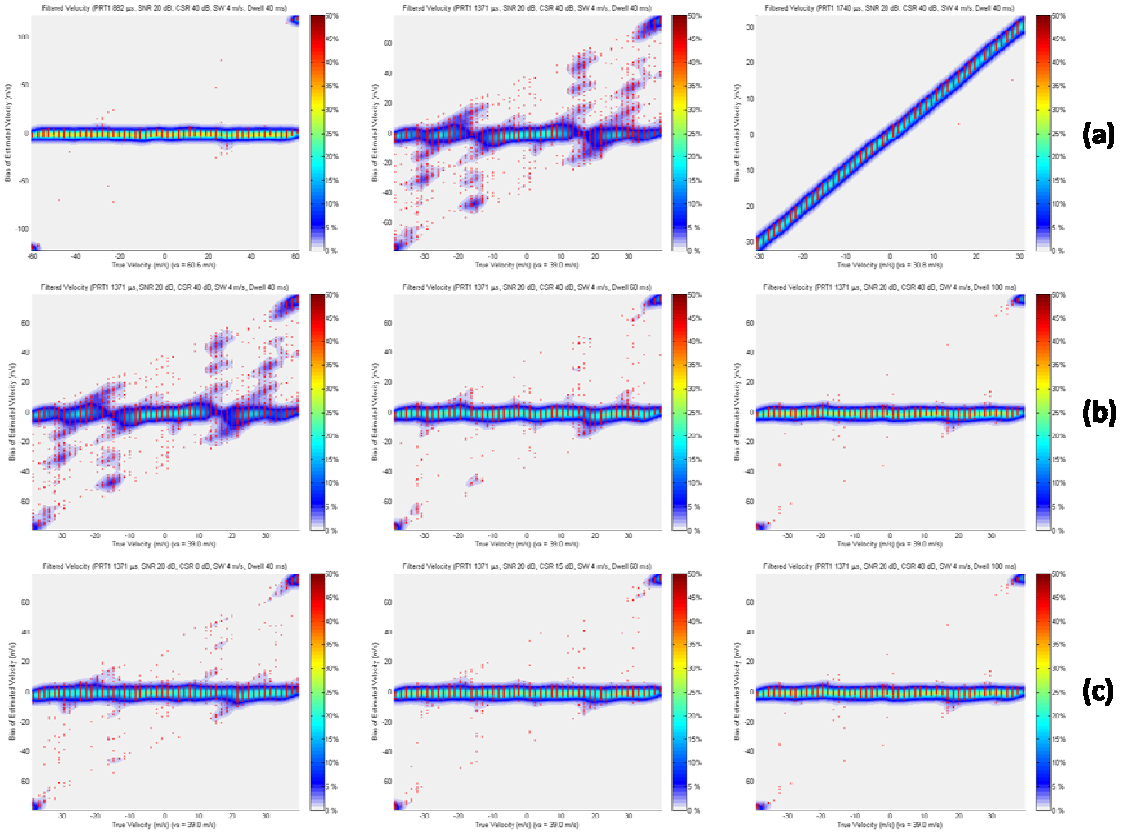

Fig. 3.3.8. SACHI filter velocity dealiasing performance.

d) Spectrum Width Clutter Suppression and Bias Analysis

The sensitivity of the spectrum width estimate to clutter contamination requires special consideration for the SPRT waveform. The SACHI filter algorithm uses a combination of filter notches, bias correction, and reduced spectral components to ensure a quality spectrum width estimate (e.g., Sachidananda 1999, Torres et al. 2005, and Torres et al.

2007). The WSR-88D SS requirements for spectrum width bias and standard deviation are 2 m/s for an input spectrum width of 4 m/s. An additional 1 m/s allowance is provided for spectrum width bias when clutter residue (SCR 15dB) is present in the output of the filter.

One hundred simulations were performed for each of the true spectrum width values of 0.1, 0.3, 0.5, 1, 2, 3, 4, 5, 6, 7, 8, 9, 10 m/s over the range of parameters listed in Table 3.3.1. The spectrum width bias is plotted as a function of true spectrum width in Fig. 3.3.9. The error bars indicate the standard deviation from the mean for each true spectrum width input. A green error bar indicates that the spectrum width meets WSR-88D SS (bias $\leq$ 2 m/s and standard deviation $\leq$ 2 m/s); whereas a red error bar indicates that the specification was exceeded in either spectrum width bias and/or standard deviation. Red lines are shown at ±2 m/s (WSR-88D SS spectrum width bias specification) and a green line is shown at 0 m/s for ease of comparison to the specifications. The density cloud depicts how the 100 estimated spectrum widths are distributed for each of the true spectrum widths inputs. The density cloud color scale ranges from red (100% occurrence) to white (0% occurrence).

In the left plot of Fig. 3.3.9, T_1 is set at 882 μs with a SNR of 20 dB, CSR of 45 dB, and dwell time of 60 ms (80 pulses); whereas in the right plot, T_1 is set at 1740 μs with a SNR of 20 dB, CSR of 10 dB, and dwell time of 40 ms (26 pulses). Both plots show that the WSR-88D SS bias and standard deviation requirements are met at the benchmark where the true spectrum width is 4 m/s. Note that the lower T_1 of 882 μs (left plot) with a longer dwell time of 60 ms has a wider range of bias estimates that are below 2 m/s. Spectrum widths that meet the bias and standard deviation requirements other than at the WSR-88D

benchmark of 4 m/s for these simulations (left plot) range from about 2 m/s to about 7 m/s. For a true spectrum width of 2 m/s the bias is at about 1.4 m/s with a standard deviation of about 2.5 m/s. At a true spectrum width of 7 m/s the bias is near 0 m/s with a standard deviation just over 2 m/s. With the higher T_1 of 1740 µs and lower dwell time of 40 ms (right plot), spectrum widths that range from about 2 m/s to about 6 m/s are within the bias and standard deviation requirements. For this case, note that there is an obvious bias saturation at about 4 m/s where the bias slope is nearly -1 m/s as true spectrum width increases. Neither of these cases meets the clutter suppression requirements of 50 dB.

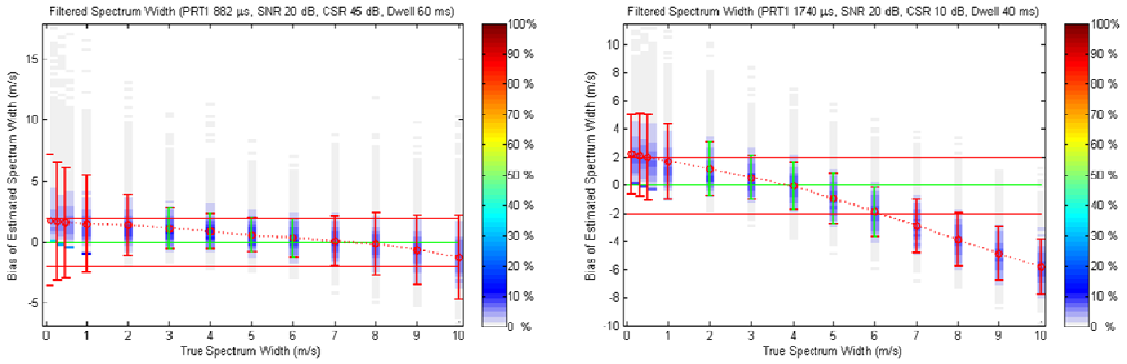

Fig. 3.3.9. Spectrum width bias and standard deviation for SACHI filter.

Table 3.3.13 summarizes the clutter suppression levels for all the cases where the bias and standard deviation requirements are met at the benchmark of 4 m/s. The table shows the same parameters as Table 3.3.2 with T_1 at the top. In general, for all the simulations, the bias is high for narrow spectrum widths and low for high spectrum widths; while the standard deviation increases as the true spectrum width moves away from the center of usable spectrum widths. Shown in Table 3.3.9 are the clutter suppression levels that meet the bias and standard deviation requirements of the WSR-88D SS. The range of spectrum widths that meet both the bias and standard deviation for all simulations with the clutter

suppression levels listed are between about 0.03 to about 0.20 of the normalized spectrum width (σ_v/v_a).

T_1 (μs)		882	1002	1125	1248	1371	1494	1617	1740	2000
v_a (m/s)		61	53	48	43	39	36	33	31	27
$r_{a,D}$ (km)		132	150	169	187	206	224	242	261	300
$r_{a,S}$ (km)		198	225	253	281	308	336	364	391	450
Dwell (ms)	40	40	35	35	35	35	35	25	10	10
	44	40	40	35	35	35	35	35	35	15
	48	40	40	40	35	35	35	35	35	15
	52	45	45	45	45	35	35	35	35	30
	56	45	45	45	45	45	35	35	35	30
	60	45	45	45	45	45	45	35	35	35
	64	45	45	45	45	45	45	35	35	35
	68	45	45	45	45	45	45	45	35	35
	72	50	50	50	50	50	50	50	45	35
	76	50	50	50	50	50	50	50	50	35
	80	50	50	50	50	50	50	50	50	45
	84	50	50	50	50	50	50	50	50	50
	88	50	50	50	50	50	50	50	50	50
	92	50	50	50	50	50	50	50	50	50
	98	50	50	50	50	50	50	50	50	50
	100	50	50	50	50	50	50	50	50	50

Table 3.3.13. Maximum clutter suppression based on spectrum width requirements for high-suppression clutter filtering.

For high clutter suppression of 50 dB depicted in Table 3.3.13, the dwell times would be required to be above about 72 ms. The high clutter suppression requirements are met for the intermediate elevation levels (1.8˚ to 4˚) of VCP 15 (Table 3.3.4) and nearly met for all of the higher elevations. This may not be a serious operational issues when we recall that the ground clutter contamination at 1.5° elevations and above is expected to be acquired through contact with the antenna side lobes which provide an additional two-way clutter isolation of about 55 dB (Sirmans 1992).

For medium and low clutter environments (28 dB and 20 dB clutter suppression, respectively), Tables 3.3.14 and 3.3.15 detail the clutter suppression performance of the SACHI filter for the same parameter settings as Table 3.3.13. Here, all elevations with SPRT waveforms for the dwell times listed in VCP 15 meet the WSR-88D requirements. In fact, almost all parameter settings meet the spectrum width bias and standard deviation requirements. The range of spectrum widths that meet the both the bias and standard deviation for all simulations with the clutter suppression levels listed are between about 0.01 to about 0.20 of the normalized spectrum width (σ_v/v_a).

T_1 (μs)		882	1002	1125	1248	1371	1494	1617	1740	2000
v_a (m/s)		61	53	48	43	39	36	33	31	27
$r_{a,D}$ (km)		132	150	169	187	206	224	242	261	300
$r_{a,S}$ (km)		198	225	253	281	308	336	364	391	450
Dwell (ms)	40	30	30	30	30	30	30	20	10	10
	44	30	30	30	30	30	30	30	30	15
	48	30	30	30	30	30	30	30	30	15
	52	30	30	30	30	30	30	30	30	30
	56	30	30	30	30	30	30	30	30	30
	60	30	30	30	30	30	30	30	30	30
	64	30	30	30	30	30	30	30	30	30
	68	30	30	30	30	30	30	30	30	30
	72	30	30	30	30	30	30	30	30	30
	76	30	30	30	30	30	30	30	30	30
	80	30	30	30	30	30	30	30	30	30
	84	30	30	30	30	30	30	30	30	30
	88	30	30	30	30	30	30	30	30	30
	92	30	30	30	30	30	30	30	30	30
	98	30	30	30	30	30	30	30	30	30
	100	30	30	30	30	30	30	30	30	30

Table 3.3.14. Maximum clutter suppression based on spectrum width requirements for medium-suppression clutter filtering.

T_1 (μs)		882	1002	1125	1248	1371	1494	1617	1740	2000
v_a (m/s)		61	53	48	43	39	36	33	31	27
$r_{a,D}$ (km)		132	150	169	187	206	224	242	261	300
$r_{a,S}$ (km)		198	225	253	281	308	336	364	391	450
Dwell (ms)	40	20	20	20	20	20	20	10	10	10
	44	20	20	20	20	20	20	20	20	15
	48	20	20	20	20	20	20	20	20	15
	52	20	20	20	20	20	20	20	20	20
	56	20	20	20	20	20	20	20	20	20
	60	20	20	20	20	20	20	20	20	20
	64	20	20	20	20	20	20	20	20	20
	68	20	20	20	20	20	20	20	20	20
	72	20	20	20	20	20	20	20	20	20
	76	20	20	20	20	20	20	20	20	20
	80	20	20	20	20	20	20	20	20	20
	84	20	20	20	20	20	20	20	20	20
	88	20	20	20	20	20	20	20	20	20
	92	20	20	20	20	20	20	20	20	20
	98	20	20	20	20	20	20	20	20	20
	100	20	20	20	20	20	20	20	20	20

Table 3.3.15. Maximum clutter suppression based on spectrum width requirements for low-suppression clutter filtering.

3.3.5. *Summary*

The SACHI filter performance has been shown to meet the WSR-88D SS requirements for reflectivity, velocity, and spectrum width. The filter performance is comparable to the current WSR-88D filter in the reflectivity channel. The largest constraint in the performance of the filter is the clutter suppression capability in the velocity channel in high-clutter environments as depicted in Tables 3.3.8 and 3.3.9. In high-clutter environments, the filter performance is comparable to the legacy IIR filter. Since the expected clutter environment at intermediate and high elevations is expected to be low to moderate, the SACHI filter performance makes SPRT a viable candidate to replace the batch and contiguous Doppler waveforms in the WSR-88D.

4. Generalized Phase Codes

The SZ-2 algorithm is based on the SZ(8/64) phase code, which was deemed optimum in the early stages of this project (NSSL Report 2, 1997). However, the methodology used to make this determination did not consider overlay situations with trip differences of more than one. With the current implementation of the SZ-2 algorithm, overlaid signals in the short PRT can exhibit trip differences of one, two, or three. Hence, it is natural to question whether the assessment done using only one overlay case still holds when we allow other overlay cases to occur. The main motivation for this work is the need to determine which phase codes might lead to better performance for overlay cases not considered before. In addition, we would like to explore the ability of other phase codes to extend the recovery of weak overlaid echoes to more trips, since the operational SZ-2 algorithm only provides recovery of weak overlaid signals up to four trips. Although this is not a limitation within the NEXRAD network, other radar systems, especially those operating at shorter wavelengths, might benefit from an approach that extends the recovery of overlaid echoes to more trips.

Herein, we look at switching codes in the SZ(n/64) family. These are of the form

$$\psi(m) = -\sum_{p=0}^{m} \frac{n\pi p^2}{64}, \; m = 0, 1, 2, \ldots \tag{4.1}$$

These codes are attractive because they exploit the WSR-88D phase shifter resolution to the maximum. That is, because the WSR-88D phase shifter is controlled with 7 bits, its

phase resolution is $2\pi/2^7 = \pi/64$. Hence, the phase shifter can realize any phase that is an integer multiple of $\pi/64$, and this is the exact same form of the code given in (4.1).

In addition, these codes have periodicities of the form $M = 2^k$ (where k is a positive integer); which make them a perfect fit for the fast Fourier transform algorithm. However, given the computational power of modern digital signal processors, this is not as important a consideration as it was a decade ago.

As with the SZ(8/64) code, the modulation codes for the family of SZ(n/64) codes are different for different overlay cases. In general, the modulation code for an overlay trip difference t is given by

$$\phi(m) = \psi(m-t) - \psi(m) = \frac{n\pi}{64}\sum_{l=0}^{t-1}\left(m-l\right)^2 \; ; \tag{4.2}$$

which for $t = 1$ (i.e., the only case analyzed in NSSL's report 2) reduces to

$$\phi(m) = \frac{n\pi m^2}{64} \, . \tag{4.3}$$

4.1. Periodicity and performance of SZ(n/64) codes

In general, the performance of systematic phase codes is measured by the ability of recovering the velocity of the weaker overlaid signal after removing most of the stronger signal. In our report 2, it was established that recovery of weak-trip velocity is possible from at least two replicas of the modulated weak-trip signal. Thus, a contradiction arises. On one hand, a modulation code producing more replicas (i.e., one with shorter periodicity) allows for a wider processing notch filter (PNF) and therefore a more

efficient suppression of the strong-trip signal. On the other hand, a modulation code producing fewer replicas (i.e., one with longer periodicity) would result in more accurate weak-trip velocity estimates since less overlap of the weak-trip replicas occurs. It would seem that the periodicity (or the number of replicas) of the modulation code determines its performance in terms of weak-trip velocity recovery. However, it can be shown with a simple counterexample that the performance of these codes is not dictated solely by their periodicity.

Let's first consider the codes SZ(8/64) and SZ(56/64). The spectra of the corresponding modulation codes are shown in Fig. 4.1, where it is evident that both exhibit the same number of replicas. The performance of these codes in terms of weak-trip velocity recovery is shown in Fig. 4.2 as the standard deviation of velocity estimates on the power-ratio/strong-trip spectrum width plane for a weak-trip spectrum width of 4 m/s and high signal-to-noise ratios. Evidently, these two codes have the same periodicity and the same performance.

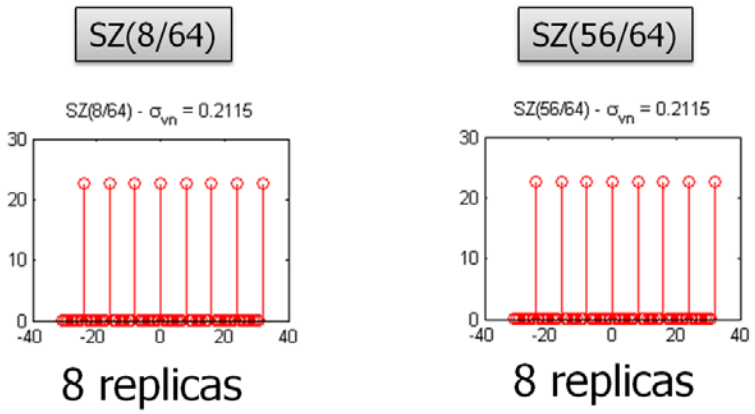

Fig. 4.1. Spectra of the SZ(8/64) and SZ(56/64) modulation codes.

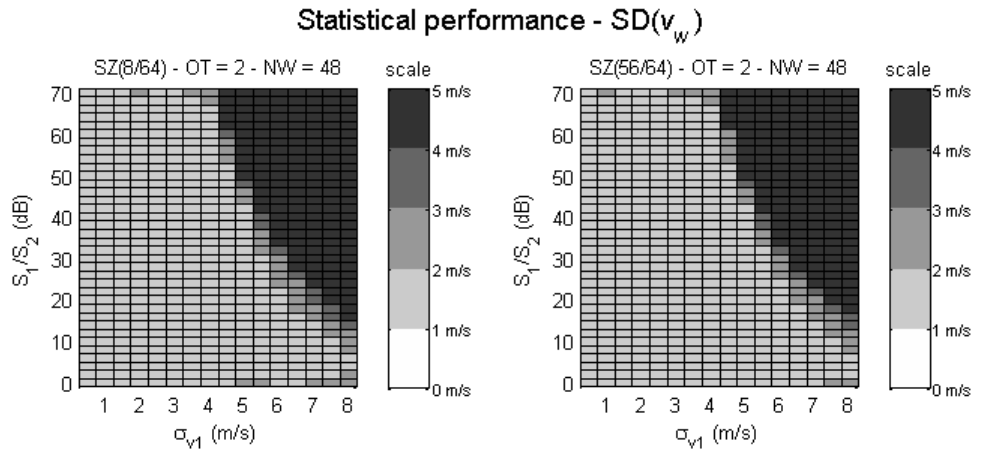

Fig. 4.2. Statistical performance of weak-trip recovery corresponding to the SZ(8/64) and SZ(56/64) codes. The plots show the standard deviation of weak-trip velocity estimates as a function of the strong-to-weak trip power ratio and the strong-trip spectrum width. Strong and weak trips differ by one.

Consider now the codes SZ(8/64) and SZ(24/64). Again, the modulation code spectra and performance charts are shown below in Figs. 4.3 and 4.4., where it is now obvious that same periodicity does not lead to same performance.

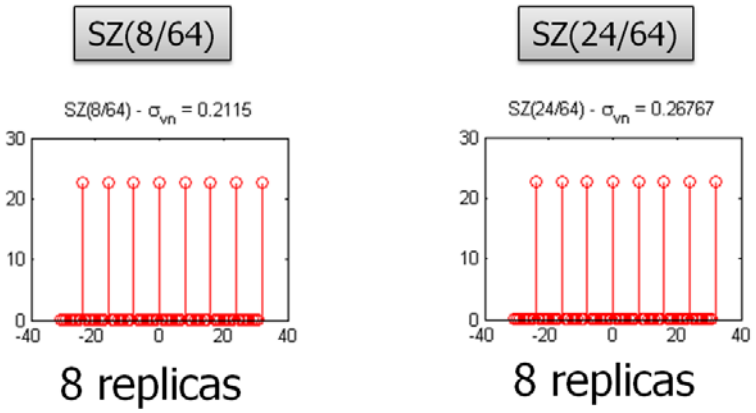

Fig. 4.3. Spectra of the SZ(8/64) and SZ(24/64) modulation codes.

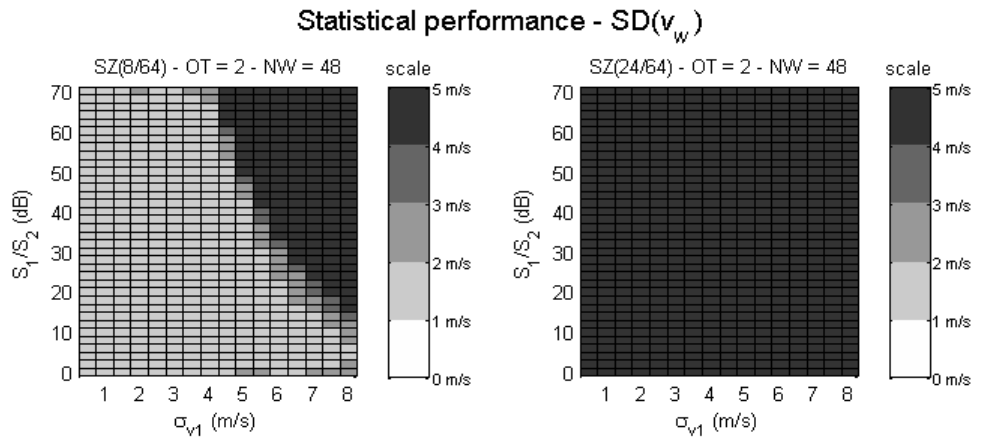

Fig. 4.4. Same as Fig. 4.2 for the SZ(8/64) and SZ(24/64) codes.

Although the periodicity of the modulation code plays an important role in the performance of these codes, it is not enough to predict it. The reader might be wondering what is different between the two examples presented above. It is important to remember that weak-trip velocities are recovered after applying the processing notch filter (PNF) and re-cohering the weak trip signal. So it would make sense to look at the spectra of the modulation codes after the same process. Fig. 4.5 shows the spectra of the modulation codes after the SZ-2 process for the codes in the examples above. Note that the codes with the same performance have the same code spectrum after notching and re-cohering. This is not the case for the SZ(24/64) code, which, as shown above, does not exhibit the same performance.

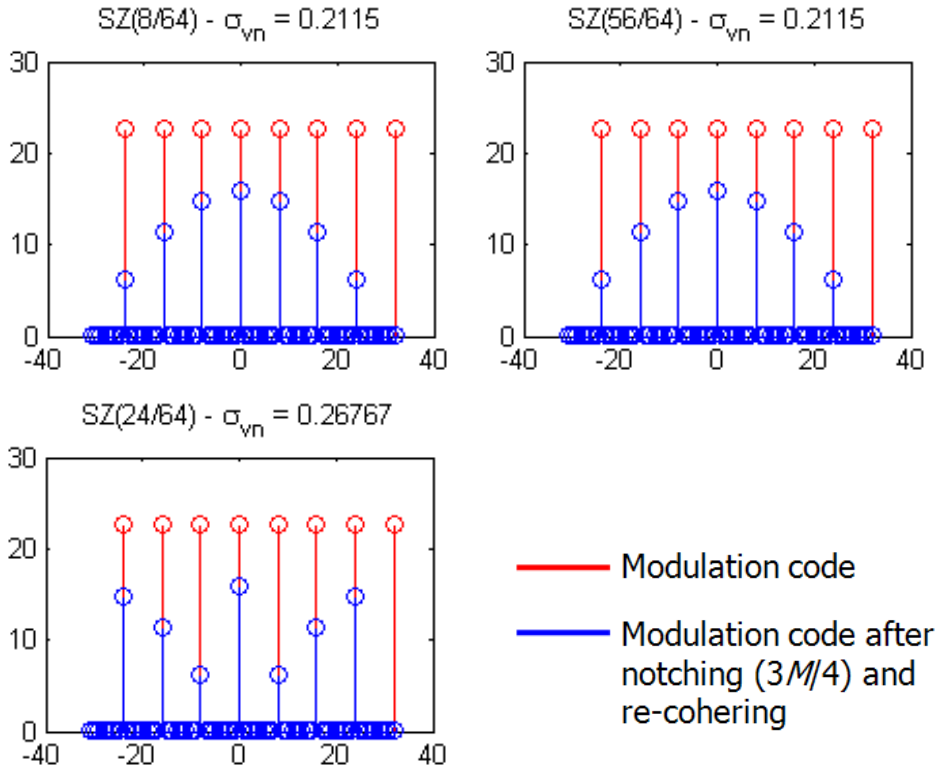

Fig. 4.5. Spectra of the SZ(8/64), SZ(56/64), and SZ(24/64) modulation codes (red) and same after notching and re-cohering (blue).

In conclusion, not all codes with the same period (i.e., the same number of replicas) exhibit the same performance in terms of weak-trip velocity recovery. The performance of a given code depends on the structure of the sidebands after notching and re-cohering. But it is not clear at this time if there is a way to predict the performance of a given code based on its sideband structure.

The previous examples showed codes with the same periodicity and different performance. Are there codes with the same performance but different periodicity? Consider now the SZ(8/64) and SZ(3/64) codes. These codes have a periodicity of 8 and 64, respectively. Although the periodicity of these codes is very different (see Fig. 4.6), their performance in terms of weak-trip velocity recovery is very similar! (see Fig. 4.7)

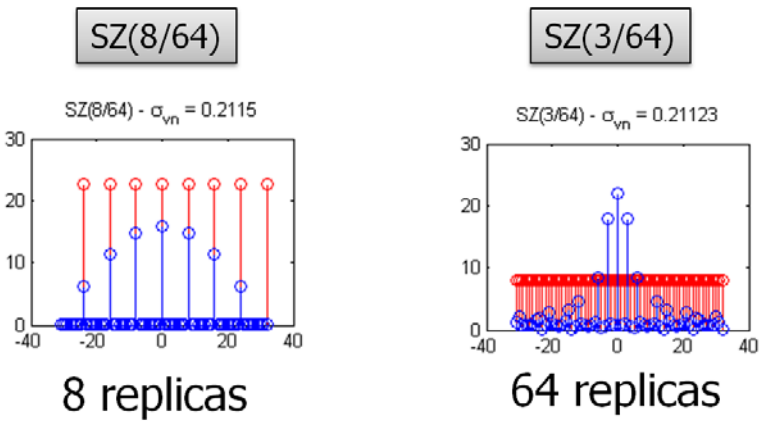

Fig. 4.6. Spectra of the SZ(8/64) and SZ(3/64) modulation codes (red) and same after notching and re-cohering (blue).

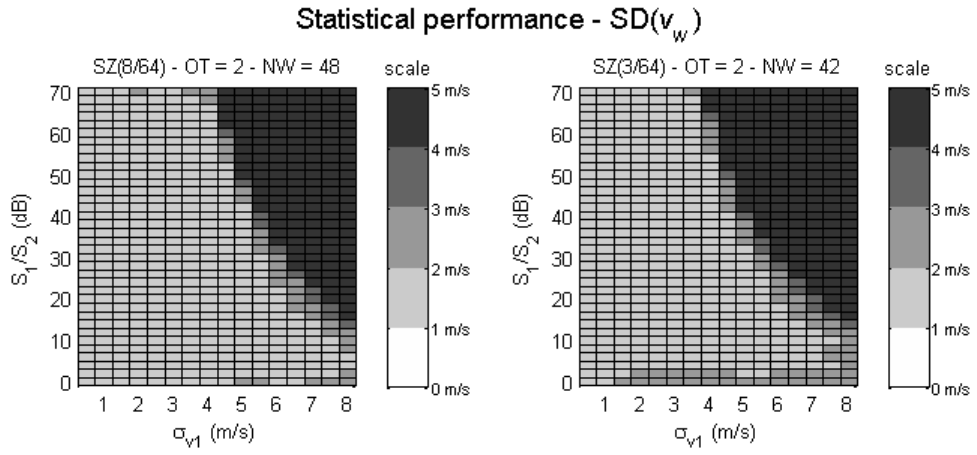

Fig. 4.7. Same as Fig. 4.2 for the SZ(8/64) and SZ(3/64) codes.

This example reinforces the idea that the performance of systematic phase codes is not uniquely related to the number of spectral "replicas" (or periodicity) of the code. In other words, as the modulation code exhibits more "replicas", the performance in terms of weak-trip velocity recovery does not necessarily get worse as previously suspected. Another consideration is that the PNF width must be tailored to the specific code and cannot be designed with the idea of retaining spectral replicas since this concept of "replicas" stops working for longer code periodicities (i.e., when the number of

"replicas" increases with respect to the normalized spectrum width of the modulated signal).

4.2. Performance of SZ(*n*/64) codes

Next, simulations are used to evaluate the performance of this family of codes in a systematic way. Once again, performance is gauged in terms of weak-trip velocity recovery, which depends on the switching code and the PNF width. The performance for any given code-PNF width combination is quantified in terms of the size of the "recovery region". That is, on the power ratio vs. strong-trip spectrum width plane, we count the number of cases for which the standard deviation of weak-trip velocity estimates is less than 2 m/s for a true weak-trip spectrum width of 4 m/s (see Fig. 4.8). Note that the relaxed 2 m/s error benchmark reflects the recently established requirements for weak-trip velocity estimates obtained with the SZ-2 algorithm.

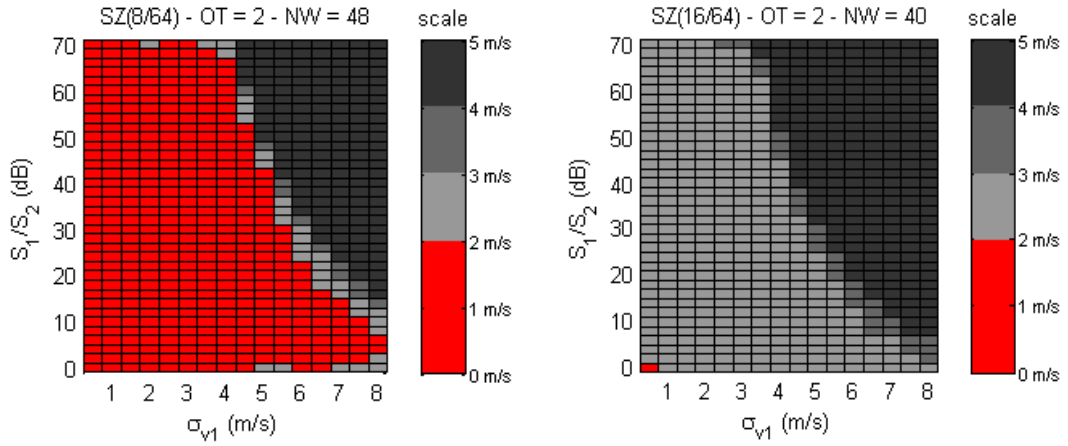

Fig. 4.8. Examples of good (left panel) and bad (right panel) phase code-PNF width combinations in terms of weak-trip recovery.

The simulation tested all codes in the SZ(n/64) family with two overlaid echoes and trip differences ranging from one to four. For each case, the PNF width was varied from 25% to 75% of the Nyquist co-interval. Signal parameters were varied as follows: the strong-to-weak signal overlaid ratio from 0 to 70 dB in steps of 2 dB; the strong-trip spectrum width from 0.5 to 8 m/s in steps of 0.5 m/s, and the overlaid signal velocities were chosen randomly in the Nyquist co-interval for each realization. The number of samples was M = 64, the weak-trip spectrum width was fixed at 4 m/s, the radar frequency was f = 2.8 GHz, the PRT was T = 780 μs, and the signal-to-noise ratio was high (more than 20 dB).

The performance for every phase code-PNF width combination is plotted in Fig. 4.9 for overlaid signals with 1, 2, 3, and 4 trip differences. Larger numbers ("warmer" colors) represent better performance (i.e., a larger weak-trip velocity recovery region).

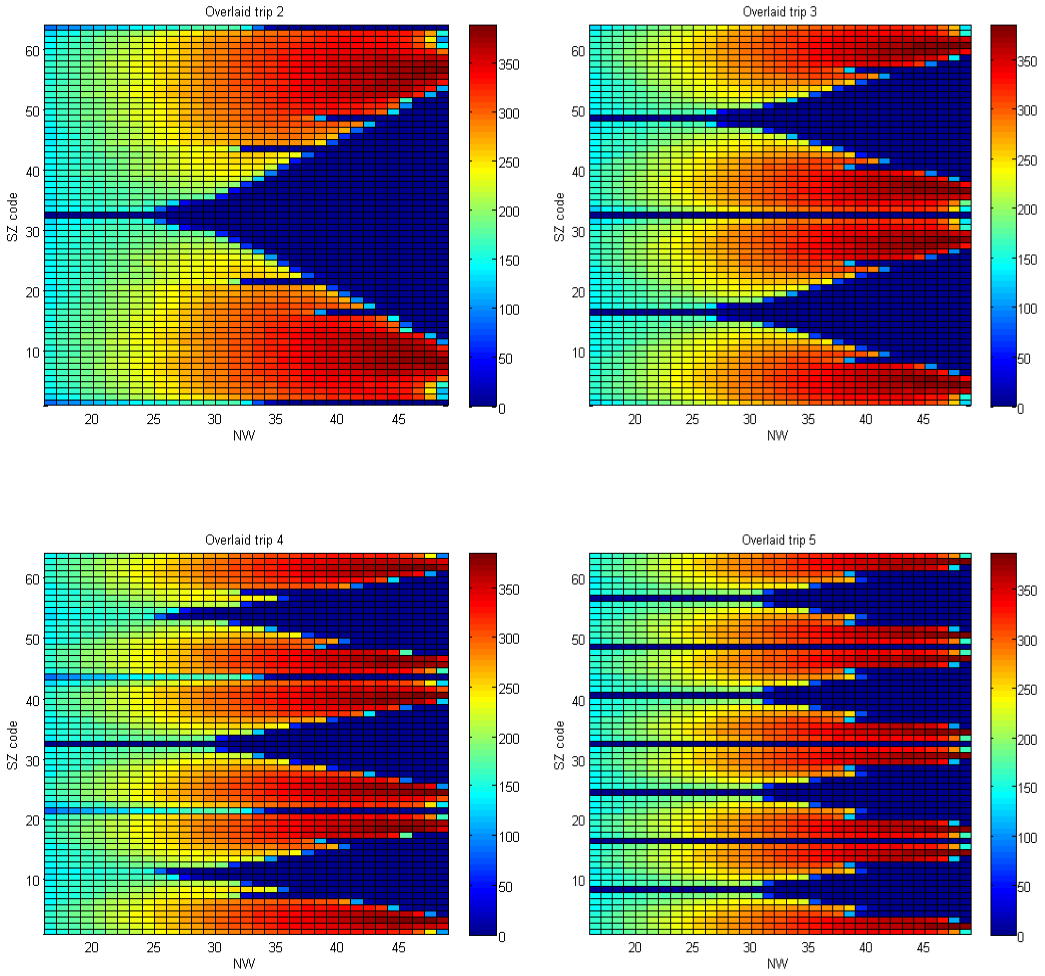

Fig. 4.9. Performance of SZ(*n*/64) codes for different PNF widths (*NW*) and overlaid cases with trip differences of 1 (top left), 2 (top right), 3 (bottom left), and 4 (bottom right). "Warmer" colors represent better performance.

Many interesting properties can be inferred from these plots. For example, the vertical symmetry about $n = 32$ would imply that codes of the form SZ(*n*/64) and SZ[(64–*n*)/64] are equivalent in terms of performance. Also, it is easy to spot codes that are not suitable for weak-trip velocity recovery, such as the SZ(32/64), which has a null recovery region for all PNF widths and overlay cases.

The performance of the SZ-2 algorithm can be obtained from this plot by looking at the rows with $n = 8$. For an overlaid trip difference of one, two, and three, the SZ-2 PNF

width is set at 48, 32, and 32, respectively. As expected, for an overlaid trip difference of four, no PNF width leads to recovery of the weak-trip velocity. Note that, as introduced earlier, SZ-2 is not the optimum for all overlay situations. The question arises then as to which codes are the best for each overlay case. Table 4.1 lists the best code-PNF width combinations for each overlay case and compares their performance to the current SZ-2 algorithm. For overlaid signals with one trip difference, the best code is SZ(56/64), which is statistically equivalent to the familiar SZ(8/64) (symmetry property). For other overlay cases, the optimum code-PNF width combinations can extend the size of the recovery region by more than 50%! However, there is no single switching code that is optimum for all overlaid cases.

	SZ(n/64)			SZ-2			
Trip difference	n	NW	Size of recovery region	n	NW	Size of recovery region	Improvement (%)
1	56	48	388	8	48	382	2
2	28	47	384	8	32	298	29
3	3	47	384	8	32	246	56
4	62	47	386	8	-	0	∞

Table 4.1. Comparison of best SZ(*n*/64) codes-PNF width combinations and SZ-2 for different overlay cases.

Fig. 4.11 shows the detailed performance of the best code-PNF width combinations. As a reference, Fig. 4.10 shows the same for the SZ-2 algorithm. Although the performances of the best combinations are appealing, it is not practical to consider different phase codes for different overlay cases. Hence, we are interested in finding the best set of combinations based on a single phase code. These are listed in Table 4.2, where the phase code with best overall performance is SZ(4/64). It is important to mention that the

determination of single-code best combinations was done considering overlay cases with trip differences of 1, 2, and 3 only. A trip difference of 4 is not possible with the WSR-88D PRTs. Still, the SZ(4/64) code can handle the overlay case with a trip difference of 4, which might be of interest for shorter-wavelength radars, such as the TDWRs. Fig. 4.12 shows the detailed performance of the single-code best combinations.

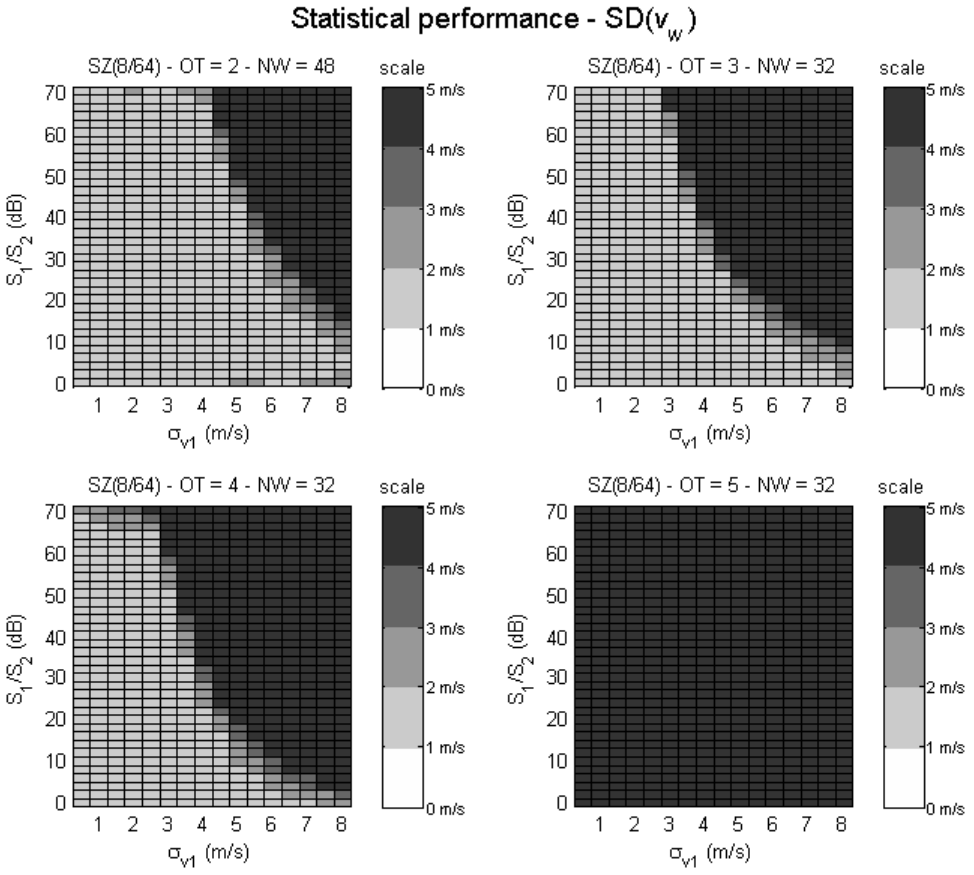

Fig. 4.10. Statistical performance of weak-trip recovery corresponding to the SZ-2 algorithm for all overlay cases.

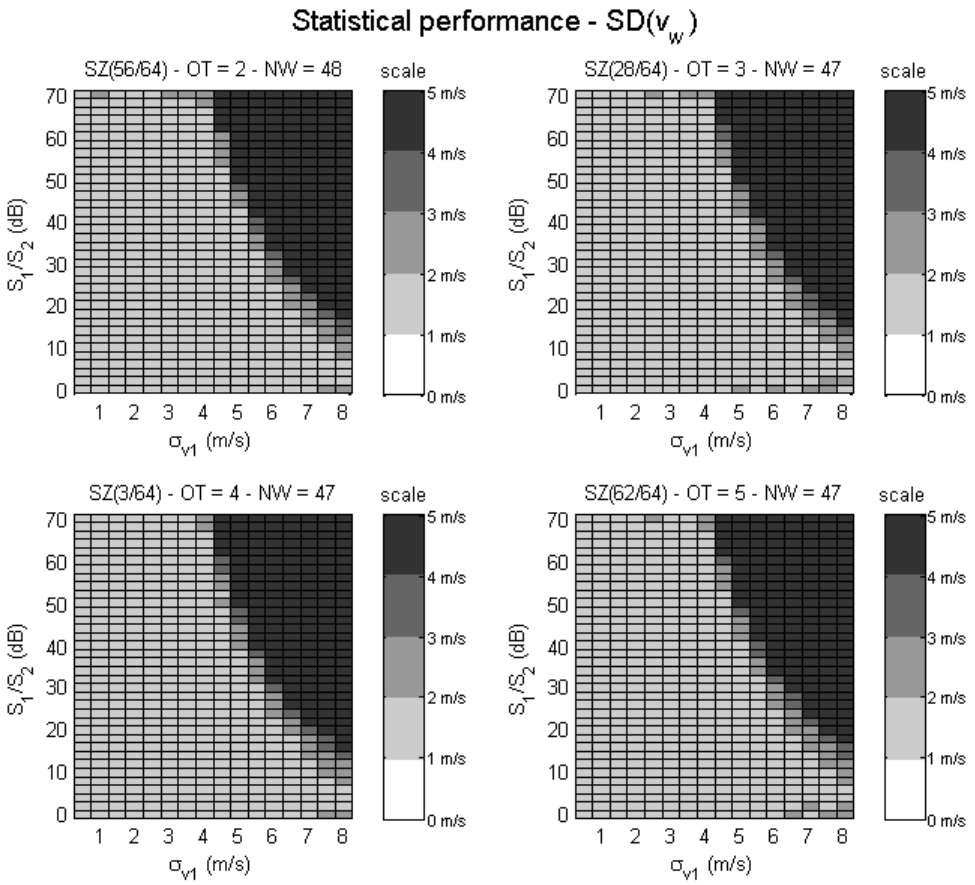

Fig. 4.11. Statistical performance of weak-trip recovery corresponding to the best code-PNF width combinations in Table 4.1 for all overlay cases. Note that each overlay case uses a different optimum phase code.

	SZ(n/64)			SZ-2			
Trip difference	n	NW	Size of recovery region	n	NW	Size of recovery region	Improvement (%)
1	4	41	343	8	48	382	-10
2	4	47	382	8	32	298	28
3	4	43	363	8	32	246	48
4	4	35	310	8	-	0	∞

Table 4.2. Comparison of single-code best combinations and SZ-2 for different overlay cases.

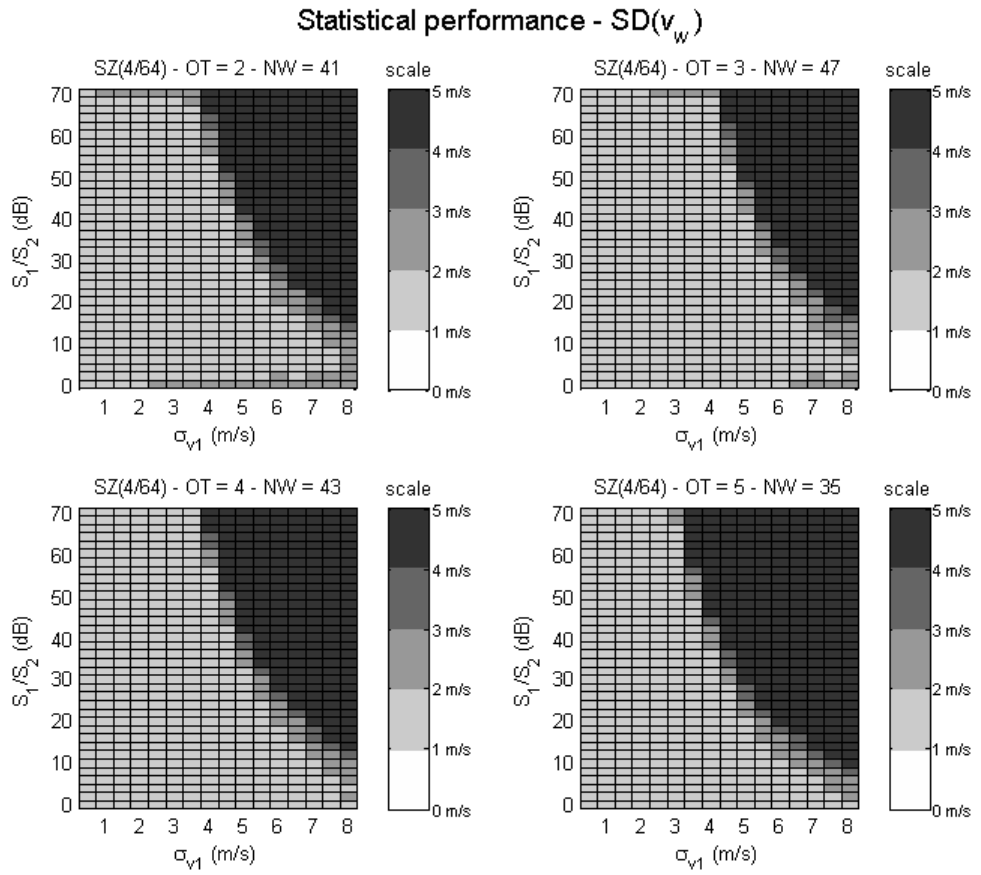

Fig. 4.12. Statistical performance of weak-trip recovery corresponding to the single-code best combinations in Table 4.2 for all overlay cases. Note that all overlay cases use the same phase code.

4.3. Effects of phase errors

The analysis in the previous section was done with ideal switching and modulation phase codes. However, it is known from our previous research that the size of the recovery region for weak-trip echoes is reduced if these codes have errors. Phase code errors contribute to a non-coherent spread of powers across the Nyquist co-interval that limits their usability for large strong-to-weak trip power ratios. Fig. 4.13 exemplifies this for the SZ(8/64) code.

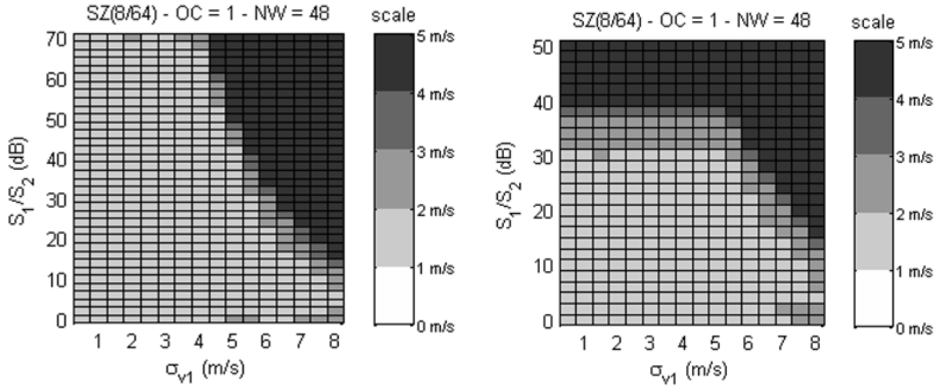

Fig. 4.13. Example of the effects of phase errors in the performance of the SZ(8/64) code. Weak-trip velocity statistics on the left panel correspond to ideal codes. The right panel shows the same for a case with phase errors.

In general, phase errors can be due to the phase shifter and/or measurements of the burst pulse. Phase shifter errors can be constant due to quantization errors (see NSSL report 7) or random due to jitter, voltage fluctuations, or variations in the signal paths (see NSSL reports 2 and 7). Burst pulse measurement errors are random by their nature. Modeling these errors mathematically is not difficult. For example, consider two overlaid radar signals and M samples in the dwell time. The individual signals can be generally denoted in vector form as $\mathbf{V}_t = \left[V_t(0),\ldots,V_t(M-1)\right]^T$, where t is the trip number and T stands for matrix transposition. Let the transmitter switching phases be $\psi(0),\ldots,\psi(M-1)$, so the re-cohering sequence for trip t can be formed in a vector as $\mathbf{\Psi}_t = [e^{j\psi(1-t)}, e^{j\psi(2-t)},\ldots, e^{j\psi(M-t)}]^T$. Without loss of generality, assume that strong signals come from the first trip and weak overlaid signals from the second trip. Hence, the received time series vector is

$$\mathbf{V} = \mathbf{V}_1^T\mathbf{\psi}_1 + \mathbf{V}_2^T\mathbf{\psi}_2 . \tag{4.4}$$

Further, let the receiver switching phases be $\psi'(0),\ldots,\psi'(M-1)$, where these do not necessarily have to be the same as the transmitter switching phases. The strong-trip cohered signal vector is

$$\mathbf{V}_1' = \mathbf{V}_1^T \boldsymbol{\psi}_1 \boldsymbol{\psi}_1'^* + \mathbf{V}_2^T \boldsymbol{\psi}_2 \boldsymbol{\psi}_1'^* . \tag{4.5}$$

To perfectly re-cohere the strong signal, it is required that $\boldsymbol{\Psi} = \boldsymbol{\Psi}'$, so

$$\mathbf{V}_1' = \mathbf{V}_1^T + \mathbf{V}_2^T \boldsymbol{\psi}_2 \boldsymbol{\psi}_1^* . \tag{4.6}$$

Moreover, for a perfect modulation of the weak-trip signal it is also required that the switching codes have the specific phases that result in no bias of the lag-1 autocorrelation estimate of $\mathbf{V}_1'$. That is, if $\boldsymbol{\Psi} = \boldsymbol{\Psi}' = SZ(n/64)$,

$$\mathbf{V}_1' = \mathbf{V}_1^T + \mathbf{V}_2^T \boldsymbol{\Phi} , \tag{4.7}$$

where $\boldsymbol{\Phi}$ is the ideal modulation code corresponding to the SZ(n/64) code.

Because all codes in the SZ(n/64) family are realizable with the existing phase shifter and these were proven to have a very high stability, a realistic simulation for the WSR-88D involves using the ideal phase codes on transmission, but adding random (burst pulse measurement) errors on reception. That is, $\boldsymbol{\Psi} = SZ(n/64)$ and $\boldsymbol{\Psi}' = SZ(n/64) + \boldsymbol{\Psi}_e$, where $\boldsymbol{\Psi}_e$ is a sequence of unit vectors with phases uniformly distributed within $\pm\theta$. In the following, θ was chosen as 0.5 deg, but this is probably an overestimation of the actual errors in operational WSR-88D radars.

Fig. 4.14 shows the performance of the SZ(n/64) phase code including phase errors as described above. As a reference, the same plots for ideal codes is in Fig. 4.15 (note that these two figures only show the relevant phase code-PNF width combinations; i.e., codes for n = 1 to 32 and PNF widths from 50 to 75%). As expected, the colors in Fig. 4.14 reflect reduced performance; i.e., smaller recovery regions.

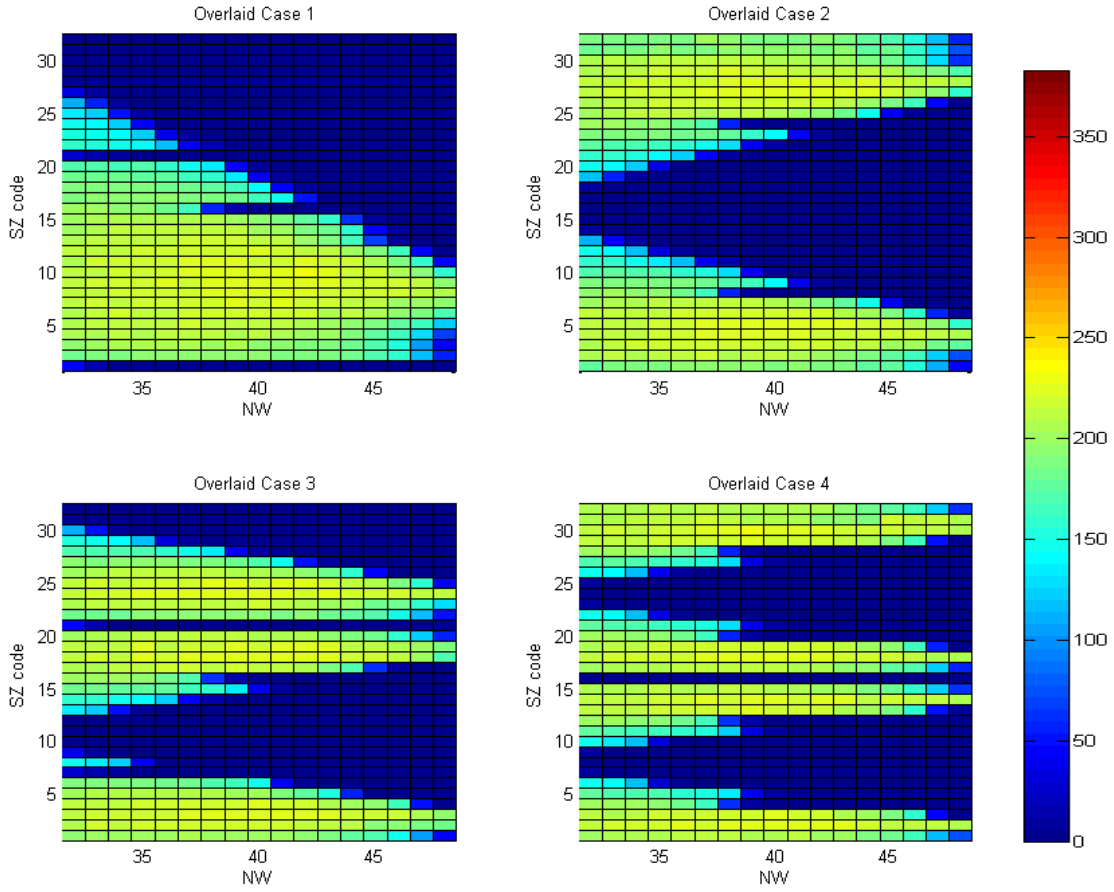

Fig. 4.14. Performance of SZ(n/64) codes with phase errors for different PNF widths (NW) and overlaid cases with trip differences of 1 (top left), 2 (top right), 3 (bottom left), and 4 (bottom right).

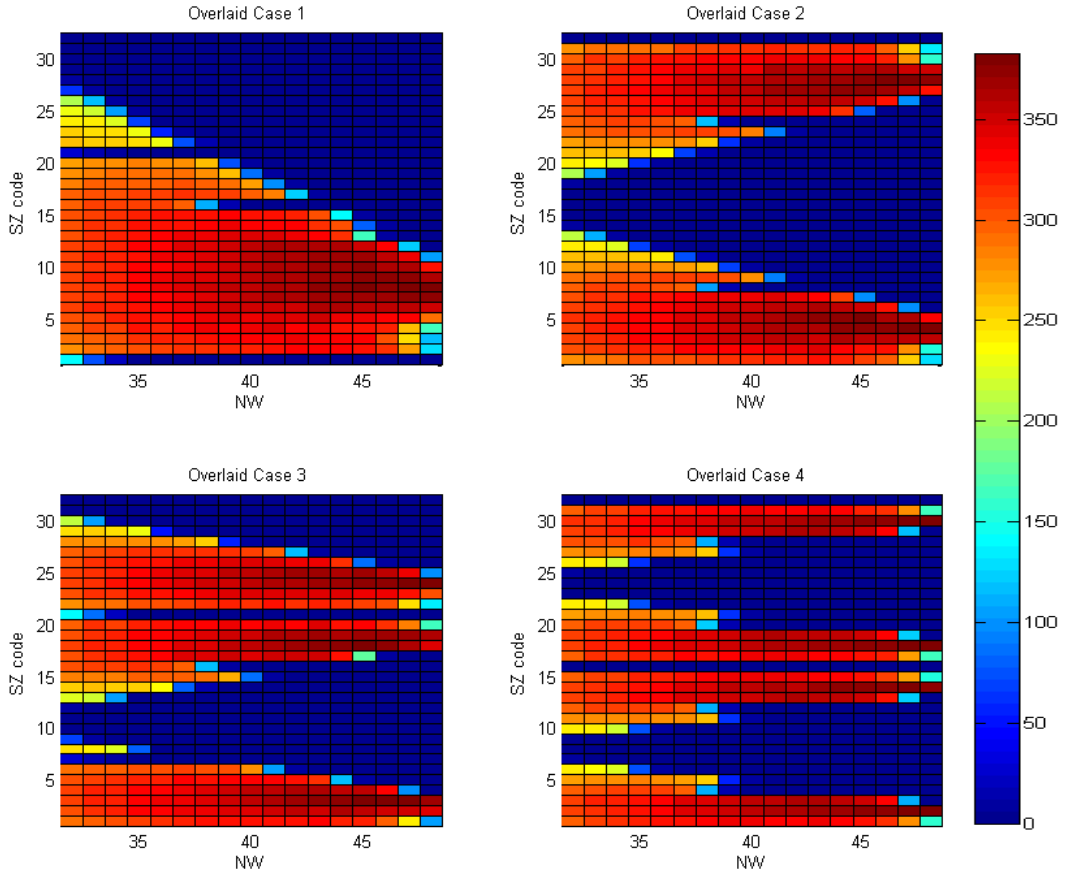

Fig. 4.15. Performance of SZ(*n*/64) codes with *no* phase errors for different PNF widths (*NW*) and overlaid cases with trip differences of 1 (top left), 2 (top right), 3 (bottom left), and 4 (bottom right).

Surprisingly, the best code-PNF width combinations are not the same when considering phase errors. Table 4.3 shows the best code-PNF width combinations for each overlay case and compares their performance to the current SZ-2 algorithm when phase errors are introduced in the receiver switching codes. For overlaid signals with one trip difference, the best code is SZ(10/64) and not SZ(8/64)! For other overlay cases, the optimum code-PNF width combinations are different, and, like before, no single switching code is optimum for all overlaid cases. It is interesting to note that in all cases with phase errors, the PNF widths are narrower than with ideal phase codes.

	SZ(n/64)			SZ-2			
Trip difference	n	NW	Size of recovery region	n	NW	Size of recovery region	Improvement (%)
1	10	42	229	8	48	207	11
2	5	41	227	8	32	197	15
3	3	40	226	8	32	146	55
4	30	39	228	8	-	0	∞

Table 4.3. Comparison of best SZ(*n*/64) codes-PNF width combinations and SZ-2 for different overlay cases when phase errors are introduced in the receiver switching codes.

Fig. 4.17 shows the detailed performance of the best code-PNF width combinations. As a reference, Fig. 4.16 shows the same for the SZ-2 algorithm. Once again, we are interested in finding the best set of combinations based on a single phase code. These are listed in Table 4.4, where the phase code with best overall performance is SZ(4/64). Note that SZ(4/64) is better than SZ(8/64) for all overlay cases when phase errors are present. Fig. 4.18 shows the detailed performance of the SZ(4/64) with optimum PNF widths for each overlay case.

	SZ(4/64)		SZ(8/64)		
Trip difference	NW	Size of recovery region	NW	Size of recovery region	Improvement (%)
1	37	214	48	207	3
2	38	225	32	197	14
3	40	222	32	146	52
4	33	201	-	0	∞

Table 4.4. Comparison of single-code best combinations and SZ-2 for different overlay cases.

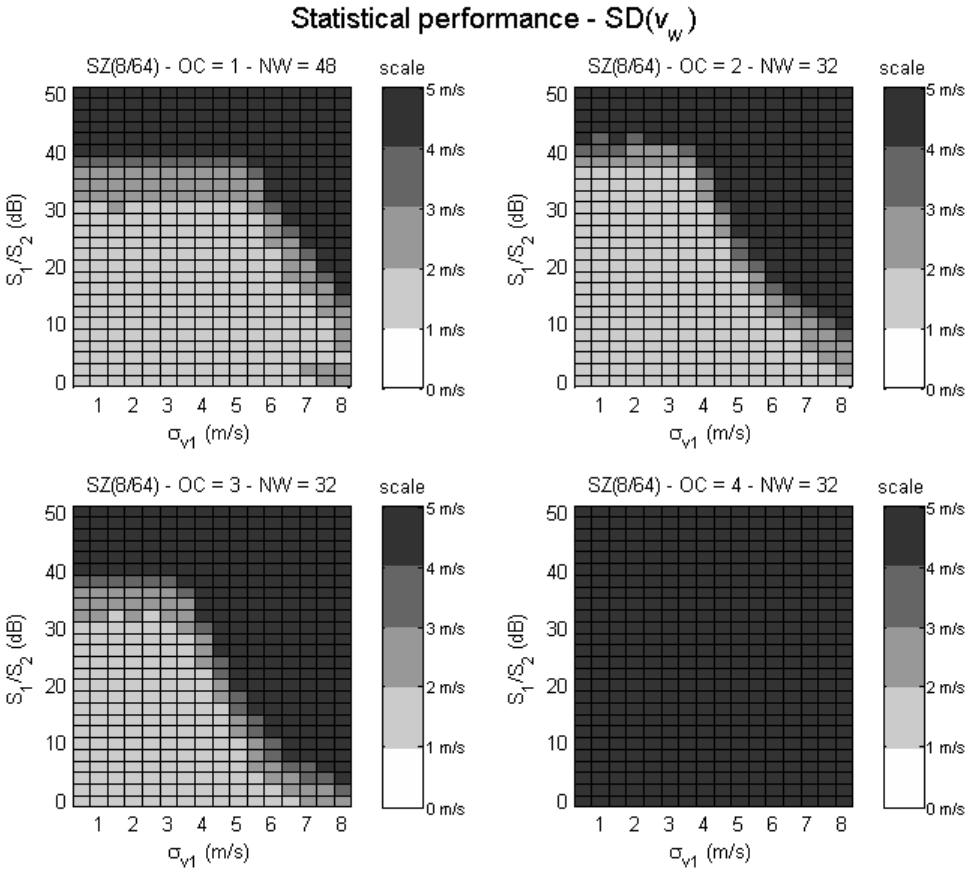

Fig. 4.16. Statistical performance of weak-trip recovery corresponding to the SZ-2 algorithm for all overlay cases when phase error is introduced in the receiver switching code.

It is obvious that this analysis is not comprehensive. However, these preliminary results justify further exploration of generalized phase codes. For example, it would be ideal to use the actual levels and types of phase errors encountered operationally on the NEXRAD network. These have not been measured systematically, except on the research KOUN radar before it was retrofitted with an ORDA. Also, it would be important to complement a simulation-based study with the analysis of multiple real-data cases collected with an ORDA.

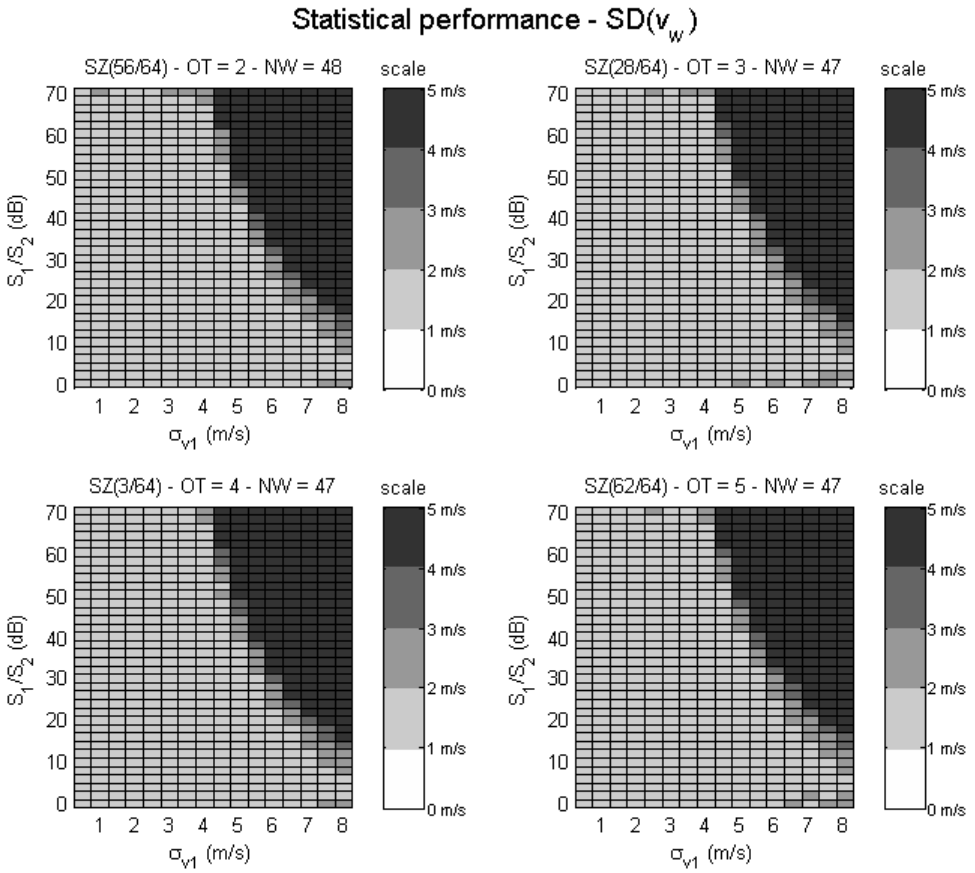

Fig. 4.17. Statistical performance of weak-trip recovery corresponding to the best code-PNF width combinations in Table 4.3 for all overlay cases when phase error is introduced in the receiver switching code.

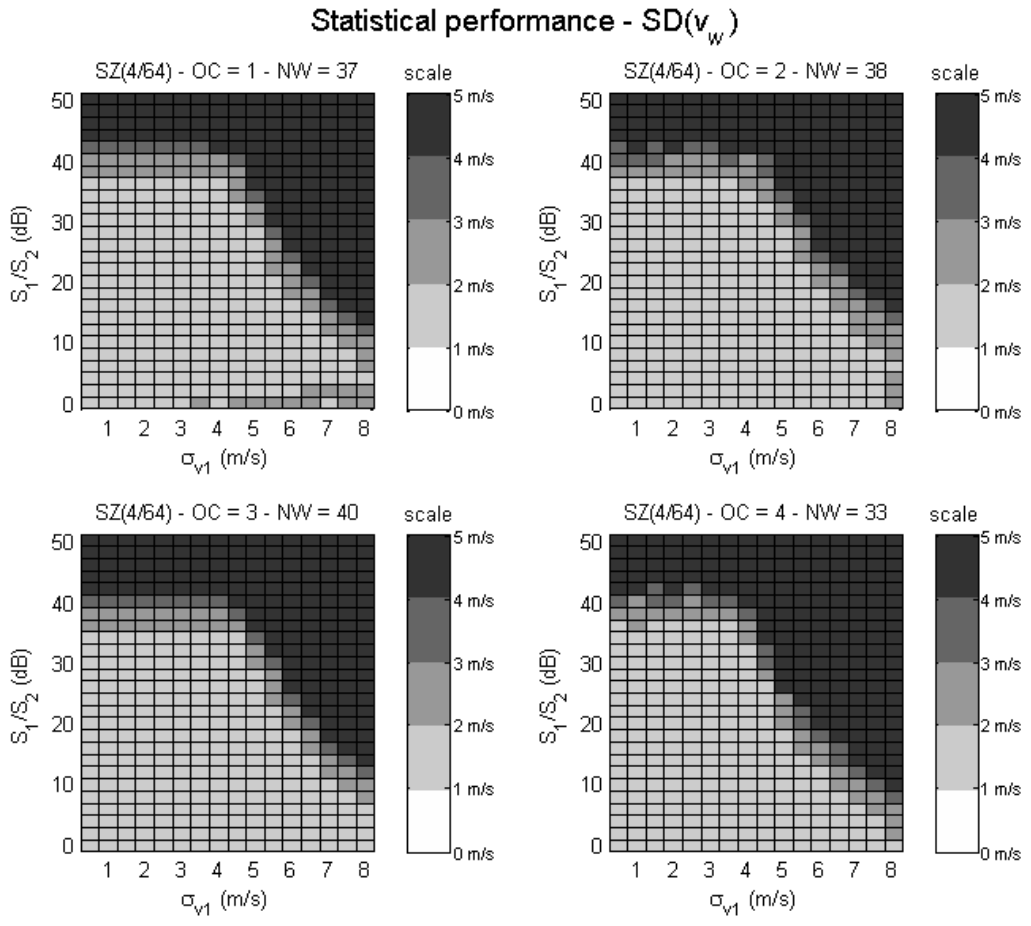

Fig. 4.18. Statistical performance of weak-trip recovery corresponding to the "single-code best" combinations in Table 4.2 for all overlay cases when phase error is introduced in the receiver switching code.

4.4. Generalization of the SZ-2 algorithm to handle SZ(*n*/64) codes

Although the SZ-2 algorithm was specifically designed to work with the SZ(8/64) code, it is not difficult to generalize it so that it can work with any code in the SZ(*n*/64) family. Fig. 4.19 shows a block diagram with the main steps in the SZ-2 algorithm. As discussed before, the WSR-88D transmitter phase shifter can handle any phase shifts that are multiples of π/64. At the receiver, each transmitter phase from the burst pulse is measured and stored for the signal processor (i.e., the switching code is part of the

metadata). Further, the current SZ-2 implementation uses the burst-pulse phases to generate the corresponding switching and modulation codes. Hence, the only change needed to transmit and receive a train of pulses encoded with any phase code in the SZ(*n*/64) family is to have the proper sequence of phases programmed into the real-time controller. Two algorithmic changes are needed to handle specific codes in the SZ(*n*/64) family. One of these changes consists of using the proper PNF width for each overlay case. The other one relates to the censoring rules for weak-trip velocities based on recovery region. As discussed in the previous sections, the size of the recovery region for each overlay case depends on the phase code-PNF width combination. Fortunately, with the changes proposed in the latest algorithm recommendation (NSSL report 11), the logic is in place to use different rules for each overlay case. Thresholds for each case could be changed very easily as they are part of each radar's adaptable parameter database. However, the determination of these thresholds requires, at least, simulation analyses that include realistic phase errors. In light of the results presented in this report and the simplicity of the required algorithm changes, we strongly recommend the evaluation of other phase codes on real weather data.

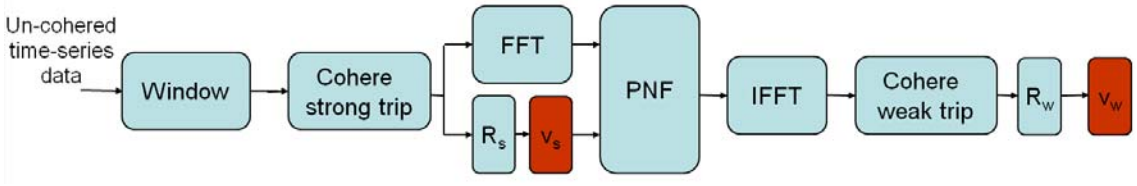

Fig. 4.19. Block diagram of the main steps in the SZ-2 algorithm.

4.5. Example of SZ(4/64) performance

To test the performance of the single-code best combinations in the SZ(*n*/64) family, we created an experimental VCP (VCP 2052) for KOUN's research RDA. VCP 2052 is described in section 2 and has a total of 10 tilts: 5 at 0.5 deg and 5 at 1.5 deg. For each elevation angle, the VCP executes: a surveillance scan, a non-phase coded Doppler scan, and three phase-coded Doppler scans using the SZ(8/64), SZ(4/64), and SZ(3/64) switching codes, respectively. On 11 September 2008 at approximately 20:45 UTC we collected a few volume scans with VCP 2052 and picked a "populated" radial for stationary antenna collection. The SZ-2 algorithm was modified as indicated in the previous section to process data collected with other SZ codes. The PNF widths were adjusted based on the previous analysis, but the recovery region thresholds were not modified; i.e., the currently recommended thresholds for the SZ(8/64) code were used.

An effort was made to have a variety of overlaid cases, especially with overlaid trip differences of two and three. However, we have not been able to get a good case to illustrate the advantages of using a phase code other than SZ(8/64). Herein, we present the results on this case, but these should be considered proof-of-concept results.

Fig. 4.20 shows the reflectivity PPI of the case under analysis at 0.5 deg. Fig. 4.21 and 4.22 show the corresponding Doppler velocity fields collected using the SZ(8/64) and SZ(4/64) codes, respectively. At this level of detail, these images look almost identical.

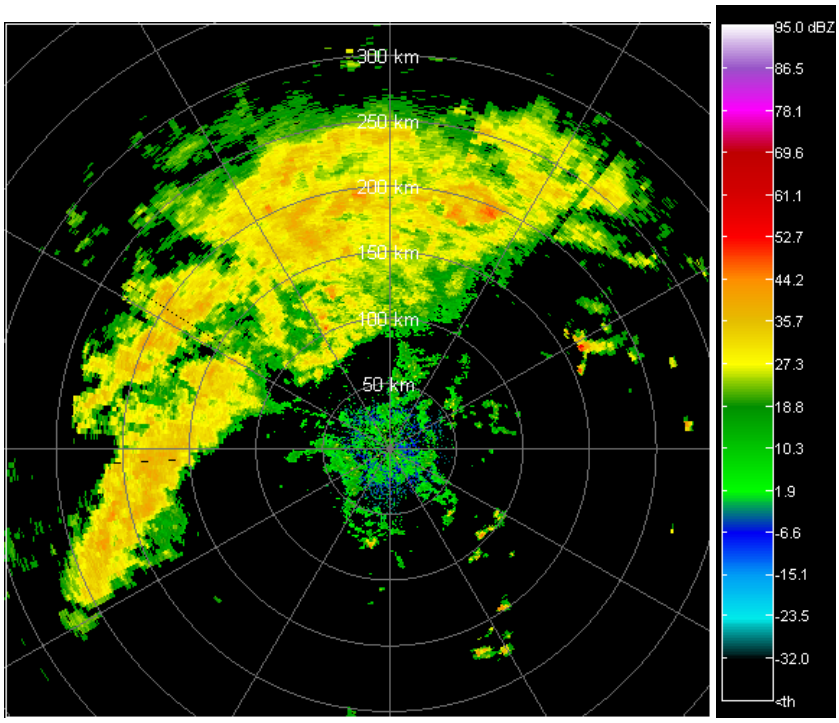

Fig. 4.20. Reflectivity PPI at 0.5 deg. Data was collected with the KOUN radar on 8 September 2008 at 20:47 UTC using the experimental VCP 2052.

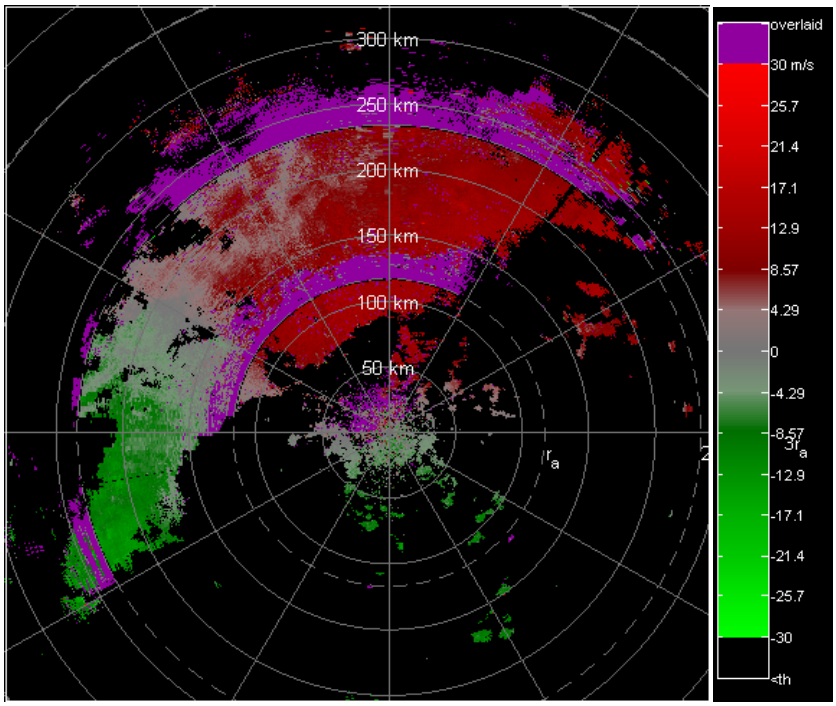

Fig. 4.21. Doppler velocity corresponding to the reflectivity in Fig. 4.20. Radar pulses were phase encoded with the SZ(8/64) code.

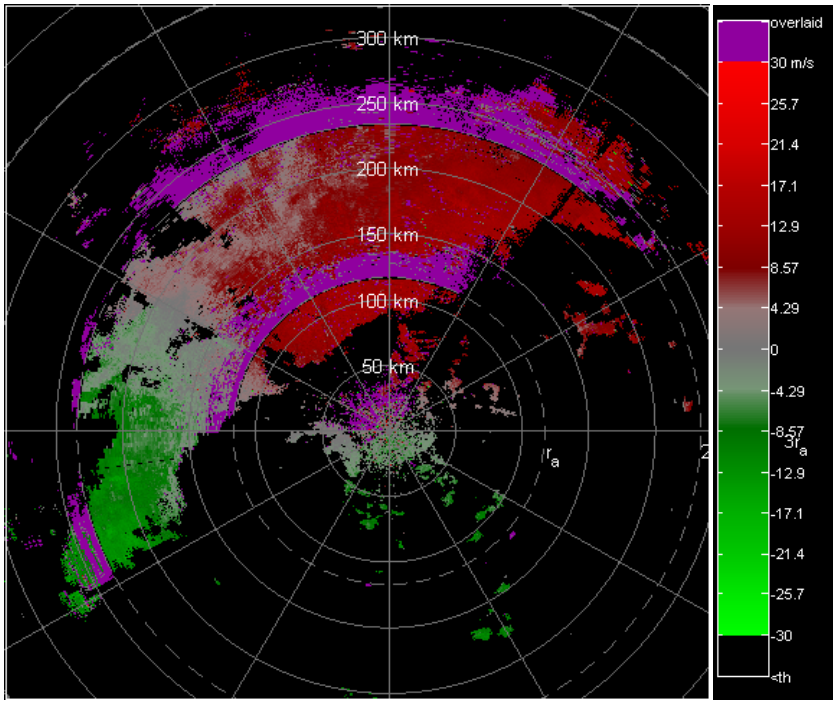

Fig. 4.22. Doppler velocity corresponding to the reflectivity in Fig. 4.20. Radar pulses were phase encoded with the SZ(4/64) code.

Fig. 4.23 shows the spatial distribution of strong and weak trip overlaid echoes. Further, Fig. 4.24 show the actual overlaid echo trip difference, where a positive (negative) trip difference indicates that the strong (weak) trip is at that location. Next, Fig. 4.25 zooms in a cell where the overlaid trip difference is mainly two. Doppler velocity fields for this cell using the SZ(8/64) and SZ(4/64) codes are shown in Fig. 4.26 and 4.27, respectively.

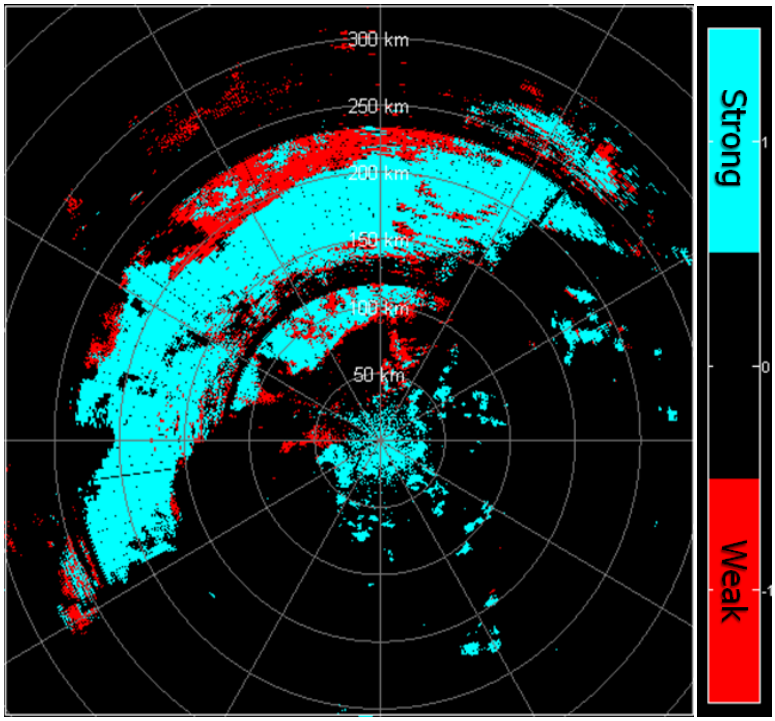

Fig. 4.23. Spatial distribution of strong and weak overlaid echoes corresponding to the reflectivity in Fig. 4.20.

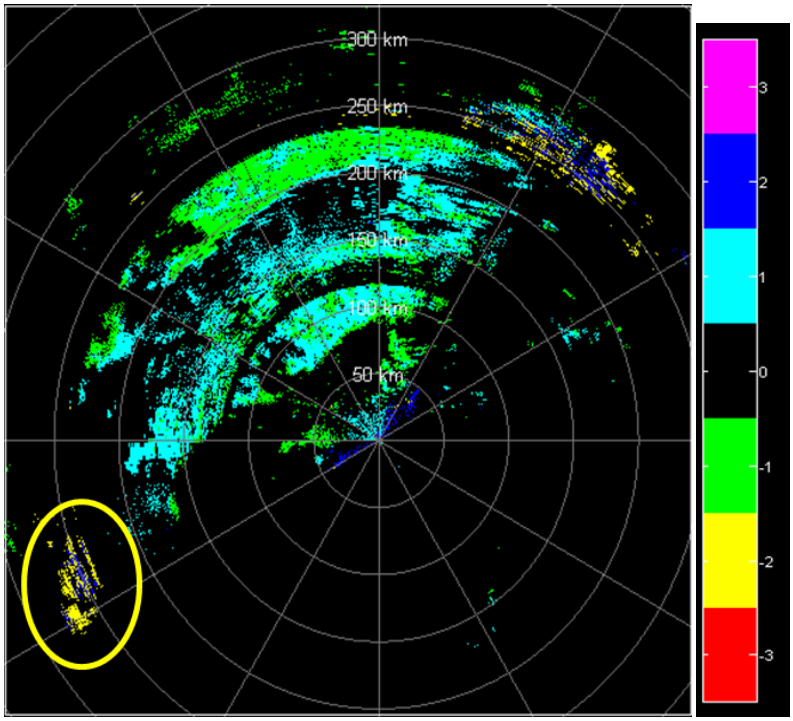

Fig. 4.24. Trip difference between overlaid echoes. A positive (negative) trip difference indicates that the strong (weak) trip is at that location.

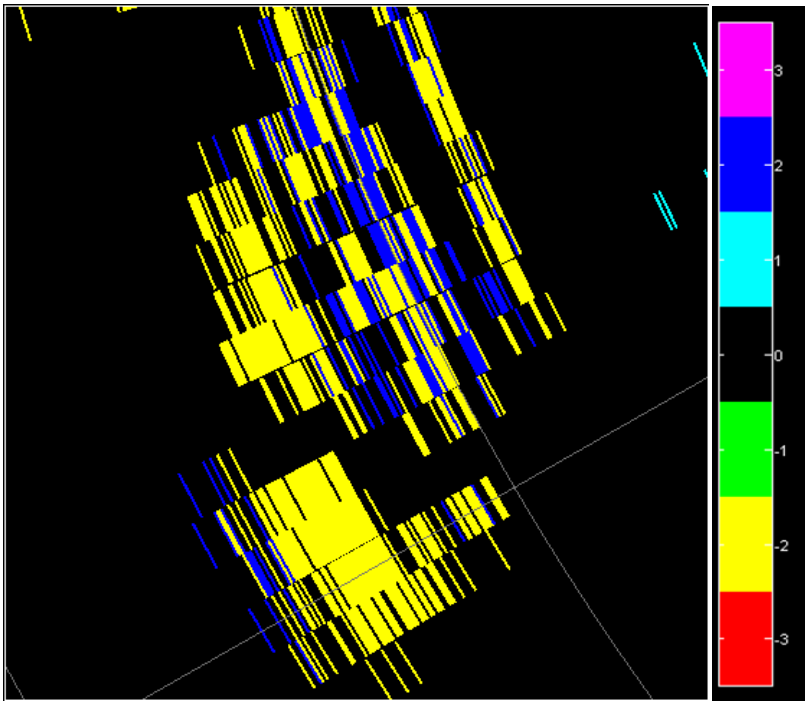

Fig. 4.25. Zoomed-in version of Fig. 4.24.

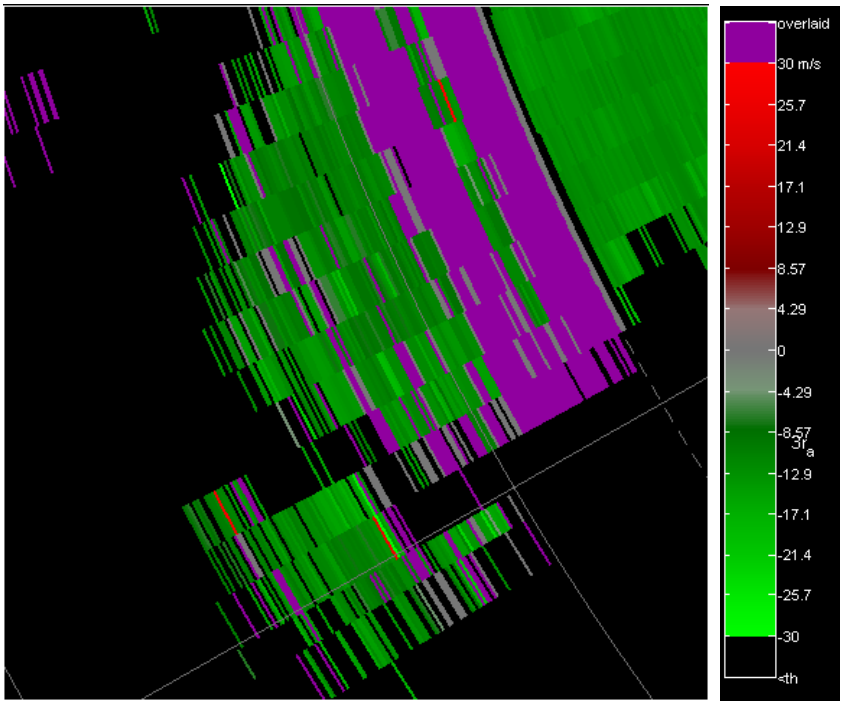

Fig. 4.26. Zoomed-in version of Fig. 4.21. Radar pulses were phase encoded with the SZ(8/64) code.

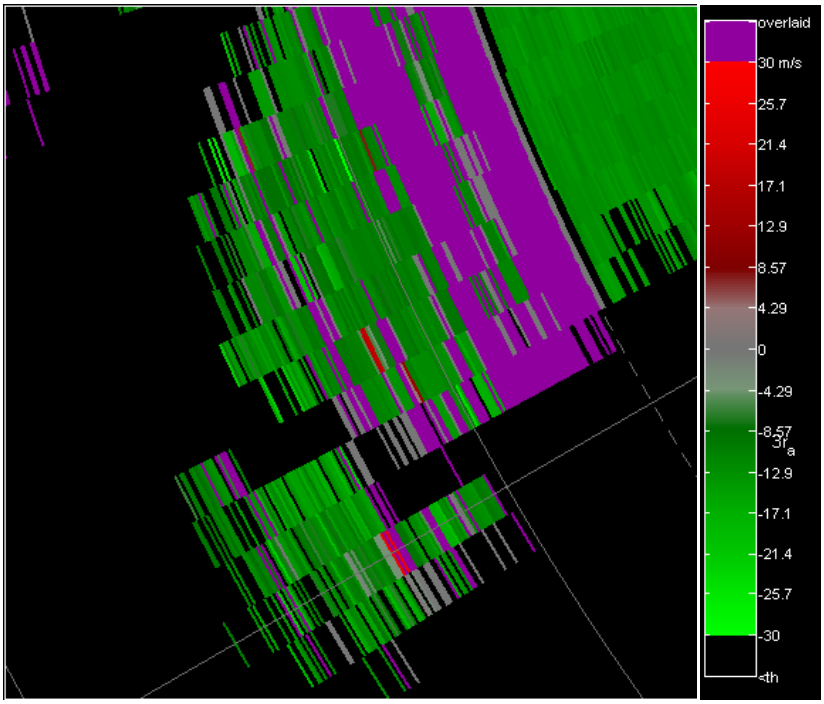

Fig. 4.27. Zoomed-in version of Fig. 4.22. Radar pulses were phase encoded with the SZ(4/64) code.

Although the zoomed-in images in Figs. 4.26 and 4.27 reveal some differences, it is not obvious which one is best. Ideally, we would have liked to find an example in which the SZ(4/64) code revealed lower errors (i.e., a smoother texture in the velocity field). However, as anticipated, this is not conveyed clearly in this case. We recommend that more data are collected with other phase codes, especially the SZ(4/64) so that a better assessment of the improvements can be done.

5. Advanced techniques

Herein, we describe a couple of mature techniques that could enhance performance of the WSR-88D. One concerns spectral densities of polarimetric variables, and the other is oversampling and decorrelating data in range. To mitigate range and velocity ambiguities in both cases will require careful adaptation of the existing techniques. Brief tutorials on the subjects follow.

5.1. Spectral densities of polarimetric variables

The power spectral density represents distribution of power (or energy) in a "signal" versus the frequency content. The term "signal" refers to an analogue physical quantity such as voltage, electric field, temperature, and so on. The distribution of the magnitude squared of such quantities versus the spatial wavelength or temporal frequency is described by their power spectral densities. Thus the precise pedantic name for the Doppler spectrum should be "Power Spectral Density (PSD) of reflectivity". We have purposely omitted any reference to the polarization of the field with which reflectivity is measured. A reader moderately cognizant of polarization principles will notice this omission and realize that the PSD of reflectivity needs a modifier specifying the polarization at which reflectivity is measured. Thus, there are two PSDs of reflectivity (i.e., Doppler spectra) one for horizontally polarized fields the other for vertically polarized fields. Generally, these two spectra would have similar shapes but would differ in magnitude if the backscattering cross sections of objects in the resolution volume depend on polarization. Further, they would have different mean velocity and/or width if the objects move at different velocities. The example in Fig. 5.1 is from a case where

insects and birds simultaneously occupy the resolution volume. The spectral peak at 10 m/s is due to the insects which are almost passive tracers advecting with the wind. The peak at 20 m s^{-1}, is attributed to birds that have substantial speed with respect to the wind.

The difference (in dBs) of the H and V spectral densities is defined as spectral density of differential reflectivity. Formally,

$$Z_{DR}(k) = 10\log_{10}\frac{|s_h(k)|^2}{|s_v(k)|^2}, \tag{5.1}$$

where k is a spectral coefficient number (corresponding of a Doppler velocity) that can be transformed to corresponding radial velocity in the interval from $-v_a$ to v_a, $s_h(k)$ and $s_v(k)$ constitute an H-V pair of complex spectral coefficients containing both the signal and the noise from the corresponding channels. To avoid bias at low SNRs the noise powers should be subtracted from the $|s_h(k)|^2$ and $|s_v(k)|^2$. The spectral density of differential reflectivity for the same data as in Fig. 5.1 is presented in the figure 5.2a. Note the increased values associated with the peak due to insects and lack of signature from the bird contribution.

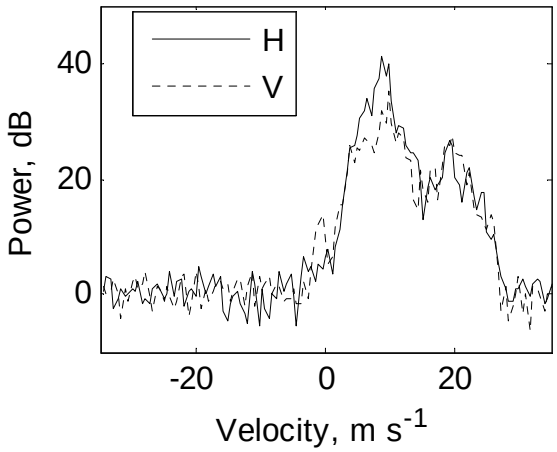

Fig. 5.1. Power spectral densities (Doppler spectra) of reflectivities at Horizontal and Vertical polarizations. These densities are averaged values of twenty spectra from consecutive range locations spaced 250 m apart between 30 and 35 km of the radar.

In a similar manner one can define the spectral density of the cross correlation coefficient $|\rho_{hv}|$ between horizontally and vertically polarized signals. Because this is a normalized (to the rms value) variable, it is not possible to estimate it from a single pair of spectral coefficients (the estimate would always equal one). At least two adjacent pairs are needed. We choose three adjacent pairs so that the estimate is representative of the centered pair. Thus, the spectral complex copolar correlation coefficient is estimated from a circular running 3 point average of the spectral coefficients as follows:

$$\rho_{hv}(k) = \frac{\sum_{m=<k-1>_M}^{<k+1>_M} s_h(m) s_v{}^*(m)}{\sqrt{\sum_{m=<k-1>_M}^{<k+1>_M} |s_h(m)|^2 \sum_{m=<k-1>_M}^{<k+1>_M} |s_v(m)|^2}}. \qquad (5.2)$$

In 5.2, M is the number of spectral coefficients in the PSD, k is an ordered index of spectral coefficient that takes values from 1 to M, and $<n>_M$ stands for n mod(M). Its magnitude and phase are the polarimetric spectral densities of interest. The example in

Fig. 5.2b illustrates the significantly larger $|\rho_{hv}|$ (about 0.95) from insects than birds (about 0.3 same as for noise).

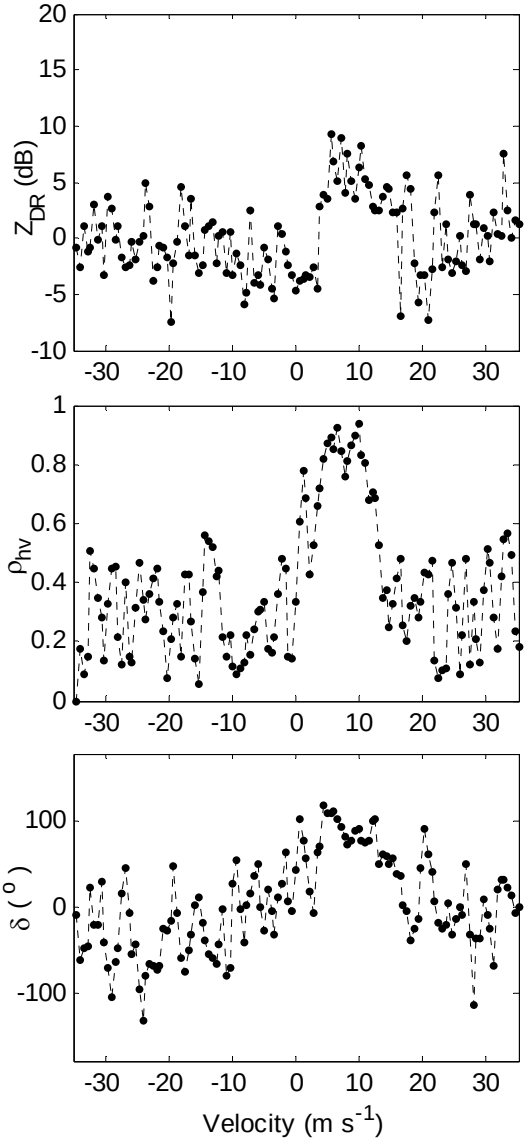

Fig. 5.2. Power spectral densities of differential reflectivity, cross correlation coefficient, and backscatter differential phase.

Last, the spectral density of the backscatter differential phase δ is simply the argument of (5.2). It can be also obtained from a single pair of spectral coefficients. Its value from insects differs from the background noise values whereas birds' values are indistinguishable from noise.

Detailed application of polarimetric spectral analysis for separating contribution from birds and insects can be found in the paper by Bachmann and Zrnić (2007) as well as in the report by Bachman (2007) which is on the NSSL's website.

5.1.1. *Application to adaptive ground clutter filtering*

A brief explanation how polarimetric spectral analysis (PSA) can be applied to recognize ground clutter is given herein. It is extracted from the report by Melnikov et al. (2008). The basic idea is to compute the polarimetric variables from the polarimetric spectral densities at and near the zero velocity where clutter, if present, would be confined. But weather signals having velocity close to zero will also be present. Nonetheless, combined use of the spectral densities increases the probability of detection while reducing false alarms. To demonstrate, histograms of the polarimetric variables and weather signals are plotted in Fig. 5.3. These overlap but by computing the polarimetric variables from the spectral coefficients near zero, most of the weather signal will be eliminated. Within the remainder a binary or fuzzy classification scheme can be used to identify clutter. This is explained next via an example.

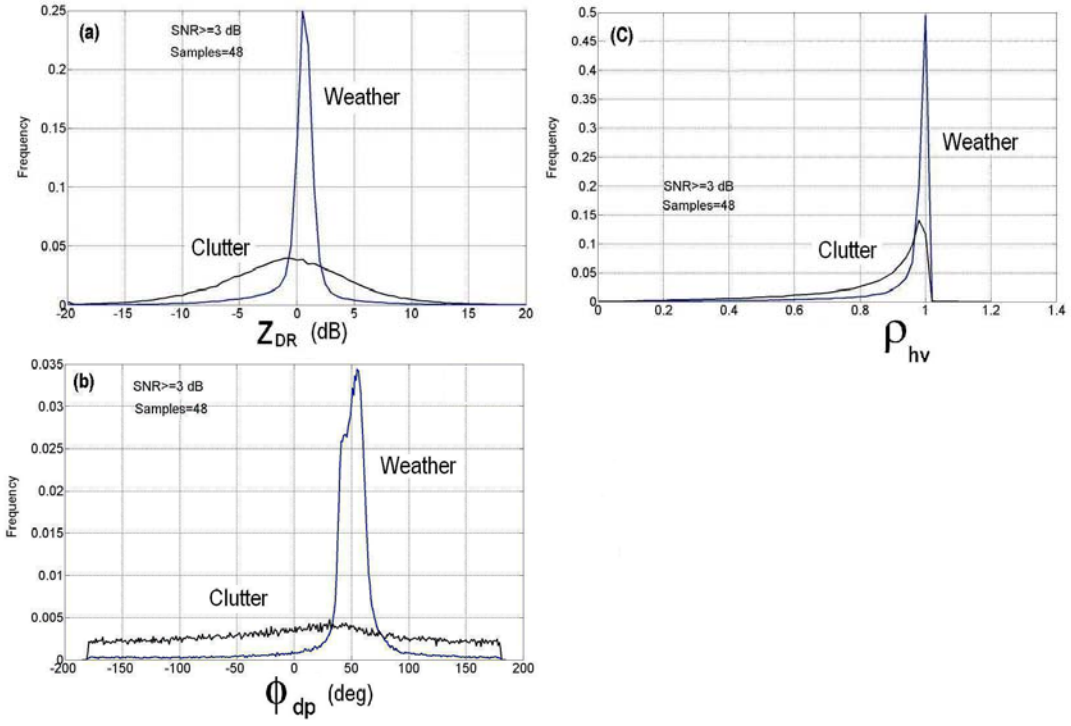

Fig. 5.3. Histograms of polarimetric variables from ground clutter and weather signals.

Four polarimetric variables are calculated using the 3-line spectra: differential reflectivity ($\widetilde{Z}_{DR}$), differential phase shift ($\widetilde{\varphi}_{dp}$), copolar correlation coefficient ($\widetilde{\rho}_{hv}$), and the power ($\widetilde{P}_h$). Radar parameters from the full spectrum will be denoted as Z_{DR}, φ_{dp}, ρ_{hv}, and P_h. The Von Hann spectral window has been applied to the time series data to obtain the spectra.

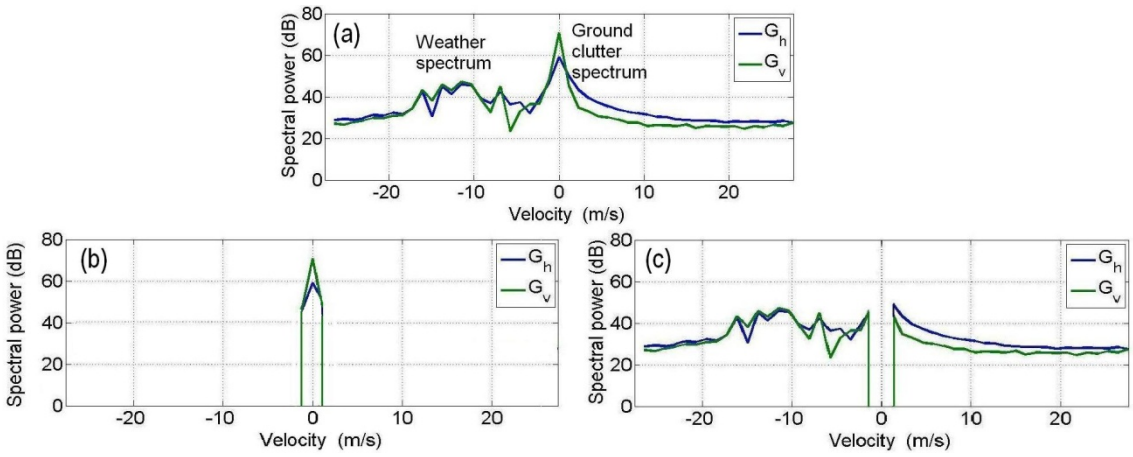

Fig. 5.4. (a): Spectra at H (blue line) and V (green line) polarizations recorded in snowfall on December 12, 2006, 0028:27; azimuth is 133°, elevation is 2.5°, PRF=1000 Hz, M=48. The spectral powers are in the internal processor units. (b): 3-line spectra obtained from the spectra in (a). (c): residual spectra obtained by removing the 3-line spectra shown in (b) from the full spectra in (a).

To recognize ground clutter, the following simple decision algorithm is applied at a given range location. The echo is considered as ground clutter if

$$\widetilde{Z}_{DR} > \widetilde{Z}_{DR2}, \text{ or } \widetilde{Z}_{DR} < \widetilde{Z}_{DR1} \quad \text{or}$$

$$\widetilde{\rho}_{hv} \le \widetilde{\rho}_{hv0}, \quad \text{or}$$

$$|\widetilde{\varphi}_{dp} - \overline{\varphi}_{dp}| \ge \widetilde{\varphi}_{dp0}, \quad \text{and}$$

$$S\widetilde{N}R_h \ge S\widetilde{N}R_{h0},$$

where $\widetilde{Z}_{DR1}$, $\widetilde{Z}_{DR2}$, $\widetilde{\varphi}_{dp0}$, $\widetilde{\rho}_{hv0}$ are predetermined thresholds, and $S\widetilde{N}R_{h0}$ is the SNR threshold which is imposed to avoid contamination from noise. Note that the thresholds are imposed on the 3-line spectrum not to the full spectrum. It means that signals with spectral component sufficiently far from zero velocity are not included in the analysis.

All the algorithm's thresholds are summarized in Table 5.1 and the radar parameters are in Table 5.2.

$\widetilde{SNR}_{h0}$, dB	$\widetilde{Z}_{DR1}$ / $\widetilde{Z}_{DR2}$, dB	$\widetilde{\rho}_{hv0}$	$\widetilde{\varphi}_{dp0}$, deg
3	-2 / 5	0.8	20

Table 5.1. Threshold parameters used in clutter recognition

Eevation, deg	Antenna rate, deg/s	Number of samples	Azimuthal resolution, deg	Pulse repetition frequency, Hz
0.5	20	48	1	1013

Table 5.2. Radar parameters used in data collection

Tests of clutter recognition with this scheme were performed on several data sets (Melnikov et al. 2008). The probability of clutter detection was larger than 93% and probability of false detection was about 5%.

Note that a fuzzy logic scheme whereby the weights would be matched to the clutter histogram might enhance recognition. Also combining this method with additional information could further improve it.

5.2. Oversampling of weather echoes in range

This is a condensed tutorial presented at the 2008 Fall technical interchange interchange meeting. The figures and text are taken directly from that presentation, and discussion is kept to a minimum. The decrease in variance due to oversampling, filtering, and averaging is explained. General theory and details about techniques to reduce errors by decorrelating the samples is contained in the papers by Torres and Zrnić (2003a, and 2003b) and Ivić et al. (2003).

Oversampling in range occurs if sample spacing is smaller than the pulse width. Oversampled signals are correlated, but if properly processed, can be used to reduce the variance of estimates. In the WSR-88D system signals are digitized at IF and oversampled. They are filtered with a "matched" filter and decimated to produce spacing equal to the pulse length. The schematic in Fig. 5.5 illustrates this transformation from the IF signal to digital signal (*I, Q*).

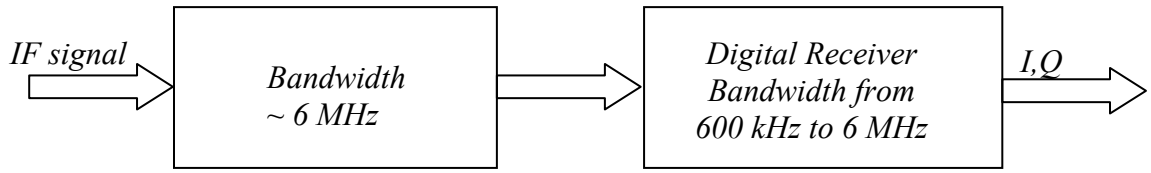

Fig. 5.5. Down conversion of the analogue IF signal to digital *I,Q* samples.

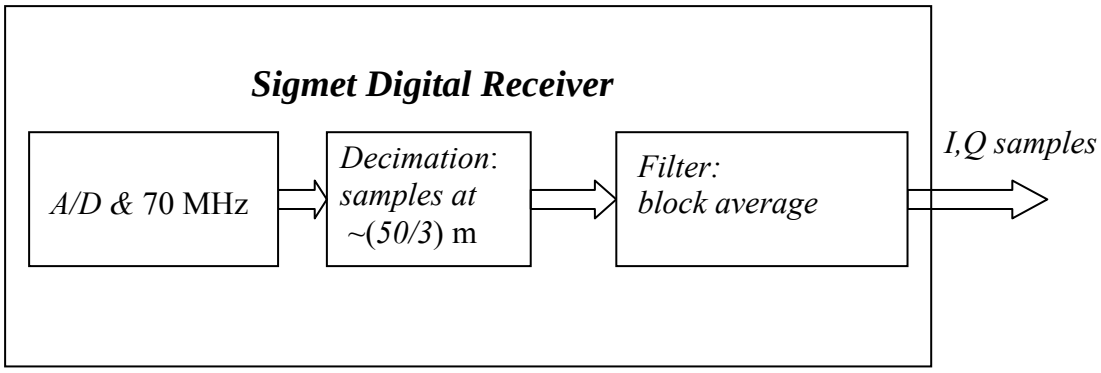

Fig. 5.6. Sigmet digital receiver.

The flow in the Sigmet Sigmet digital receiver is in Fig. 5.6. Conversion to digital values is the first step; it is followed by decimation and filtering. Next, by way of examples we will indicate how much the variance can be reduced by averaging and what the effective range weighting function looks like. First the following summarizes notation:

Signal correlation = $\rho(m)$

Power correlation = $\rho^2(m)$

Equivalent number of independent samples L_I is

$$L_I = \frac{L}{\sum_{m=1-L}^{L-1} (1 - |m| / L)\rho^2(m)} \tag{5.3}$$

Range weighting functions:

$$W_p(\text{power}) = |W_s(\text{signal})|^2$$

Estimation of power (and autocorrelations) is from sums of signal magnitudes squared. Therefore the correlation of power samples is needed to compute the reduction in variance and to determine the range weighting function.

5.2.1. *Example 1: Oversampling and averaging – wide receiver bandwidth*

Consider oversampling by $L = 5$, and a wide receiver bandwidth. This means that in the WSR-88D case the five samples are spaced 50 m apart (Fig. 5.7).

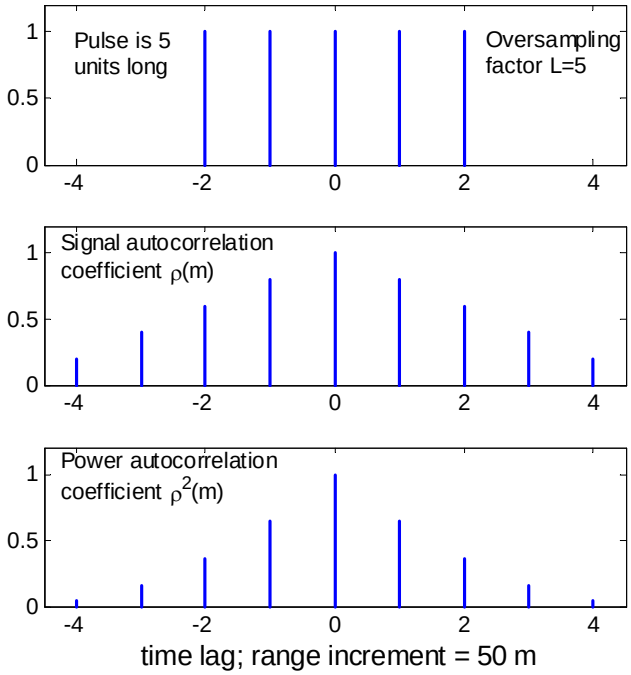

Fig. 5.7. Oversampling by a factor of $L = 5$. In the top figure the pulse length is five units and there are five samples within that pulse. The signal and power autocorrelation functions of the five sample burst (top figure) are plotted in the middle and bottom figures respectively.

In this case the autocorrelation coefficient for power $\rho^2(m=1 \text{ to } 9)$ = (0.04, 0.16, 0.36, 0.64, 1, 0.64, 0.36, 0.16, 0.04), hence

$$\sum_{m=1-L}^{L-1} (1-|m|/L)\rho^2(m) = 2.6, \tag{5.4}$$

and the equivalent number of independent samples is $L_I = 5/2.6 = 1.92$.

5.2.2. *Example 2: Oversampling, filtering, and averaging*

In this example the oversampled signals are filtered by a three point running summation. This process and the corresponding correlation functions are indicated in Fig. 5.8a and b.

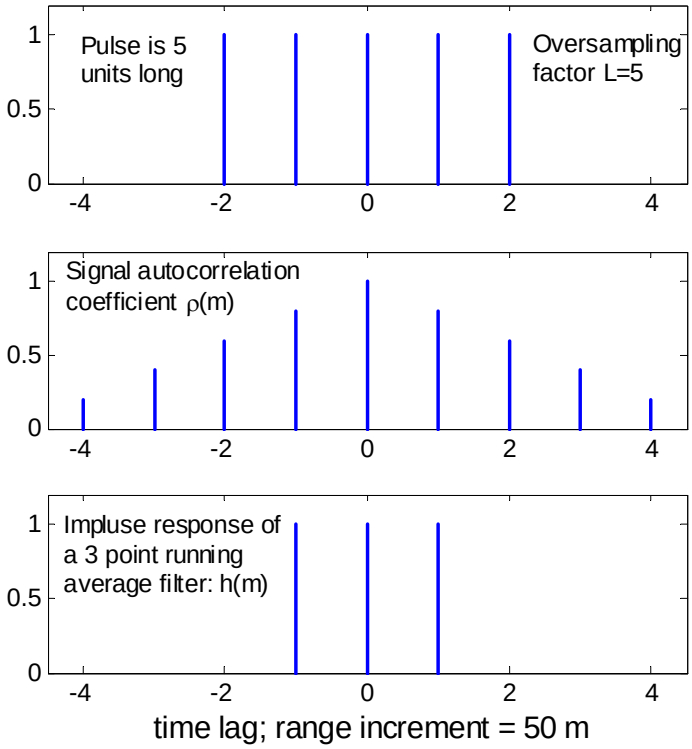

Fig. 5.8.a. Oversampling by a factor of $L = 5$, filtering, and averaging. In the top figure the pulse length is five units and there are five samples within that pulse. The autocorrelation function $\rho(m)$ of these five samples is in the middle plot and the impulse response $h(m)$ of the three point running filter is at the bottom.

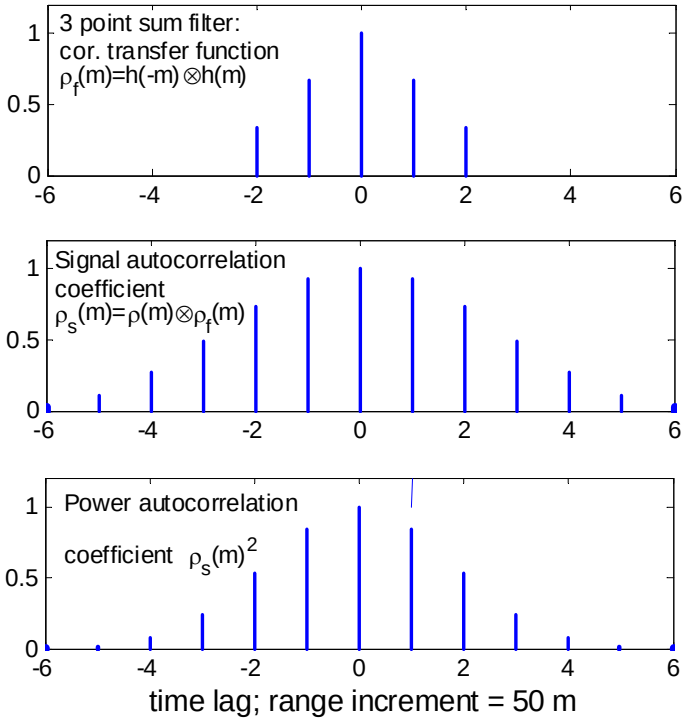

Fig. 5.8.b. Oversampling by a factor of L = 5, filtering, and averaging. In the top figure the transfer function in the autocorrelation domain of the three point running average is plotted. It is a convolution of the impulse response with its mirror image (indicated with the equation). This transfer function convolves with the signal autocorrelation coefficient (middle graph in 5.7.a) to produce the autocorrelation coefficient of the filtered signal (middle graph in this figure). In the bottom figure is the power autocorrelation coefficient.

The oversampling factor is L = 5, and assuming that the power is estimated from the sum of L_s = 5 consecutive samples, the integral $\sum_{m=1-L_s}^{L_s-1}(1-|m|/L_s)\rho^2(m)=3.2$. Therefore the number of independent samples is $L_I = L_s /3.2 = 5/3.2 = 1.56$.

Under similar conditions, oversampling by L= 5 followed with a 3-point averaging filter and then summing L_s = 7 consecutive magnitudes squared (i.e., power is computed) from seven samples $L_I = L_s /3.54 = 7/3.54 \sim 2$.

The increase of the number of independent samples is at the expense of range resolution. This is illustrated in Fig. 5.9 where the power range weighting function of the perfect matched filter to the 250-m pulse (dashed line) has narrowest width (best resolution). If five samples of powers are averaged over range and there is no prior filter, the range weighting function has a triangular shape (red graph). If the wide band samples are coherently added (3 points running filter) and then 5 consecutive power samples are averaged, the range weighting function further widens (blue curve). The dotted purple graph is obtained in the same manner as the blue curve except the running filter was 5 rather than 3 units long, i.e., it is a matched filter after which five consecutive power samples are averaged. Finally, in the case of the black curve, the oversampling factor L is 7, the running average filter is over 3 points, but the sum of powers is over 5 units.

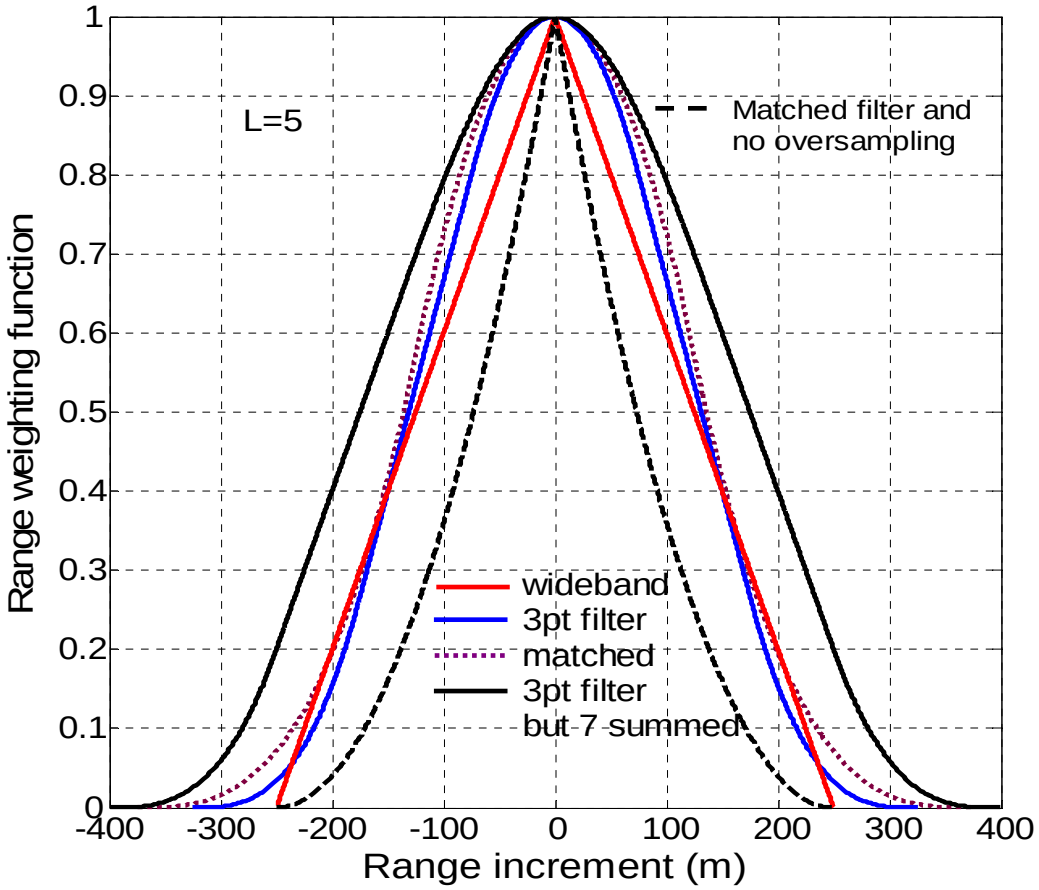

Fig. 5.9. Range weighting functions, normalized to the peak.

A summary of the pertinent parameters in the cases of oversampling, filtering, and averaging is in the Table 5.3. In this table, the noise power N is the total wide band noise corresponding to the bandwidth which is reciprocal of the sample spacing of the oversampled signals. Oversampling factor L=5. If the number of averaged consecutive power samples equals 5 (i.e., L) the highest number of independent samples (1.92) is for no filtering of the oversampled signals prior to averaging.

Property Method	Noise power	Number of Independent samples L_I	Range weighting function
Wide band	N	1.92	Triangle $2L$ base
Filter 3 pts	$N/3$	1.5 (L=L_s=5) ~ 2 (L=5; L_s=7)	Slightly larger
Filter matched	$N/5$	1.16 (L= L_s =5)	Still larger

Table 5.3. Properties in the results of various processing schemes

In the second row, a three point running average is applied to the complex samples and then five (L_s = 5) or seven (L_s =7) consecutive power samples are averaged. The range weighting function width is described qualitatively. Exact shapes for several are in Fig. 5.9. The range weighting function for the case (L = 5; L_s = 7) is not plotted but plotted is the function for (L = 7; L_s = 5) where a three point filter is applied first before summing 5 consecutive power samples to obtain estimates.

6. References

Bachman, S., 2007: Spectral Analyses of the Dual Polarization Doppler Weather Radar Data, NOAA/NSSL Report.

Bachmann, S., and D. Zrnić, 2007: Spectral Density of Polarimetric Variables Separating Biological Scatterers in the VAD Display. *J. Atmos. Oceanic Technol*. **24**, 1186–1198.

Doviak, R. J. and Zrnić, D., *Doppler Radar and Weather Observations*, 2nd Edition, 1999. Academic Press, pp 134.

Federal Meteorological Handbook, Number 11, 1989. Part B, Doppler radar theory and meteorology.

Ice, R., D. Warde, D. Sirmans, D. Rachel, Report on Open RDA – RVP8 Signal Processing, Part 1 – Simulation Study, WS-88D Radar Operations Center Report, January 2004. 87 pp.

Ivić, R.I., D.S. Zrnić, and S. M. Torres, 2003: Whitening in range to improve weather radar spectral moment estimates. Part II: Experimental evaluation. *J. Atmos. Oceanic Technol.*, **20**, 1449-1459.

Melnikov, V. M., P. Zhang, D. S. Zrnić, and A. Ryzhkov, 2008: Recombination of Super Resolution Data and Ground Clutter Recognition for the Polarimetric WSR-88D, NOAA/NSSL Report.

Sachidananda, M., 1999: Signal Design and Processing Techniques for WSR-88D Ambiguity Resolution, NOAA/NSSL Report, Part 3, 81 pp.

Sirmans, D., and Bill Bumgarner, 1975: Numerical comparison of five mean frequency estimators. Journal of Applied Meteorology, vol.14, No.6, 991-1003.

Sirmans, D., Clutter Filtering in the WSR-88D, OSF Internal Report, October 1992. 125 pp.

Sirmans, D., D. Zrnić, and B. Bumgarner, 1976: Extension of maximum unambiguous Doppler velocity by use of two sampling rates. Preprints, 17th Conf. on Radar Meteorology, Seattle, WA, Amer. Meteor. Soc., 23–28.

Sirmans, D., Patel, N., Leatherman, R., ORDA Clutter Filtering Options Assement and Recommendation, Office of Science and Technology, Open RDA Project, Internal Report, January 2003.

Torres S., M. Sachidananda, and D. Zrnić, 2005: Signal Design and Processing Techniques for WSR-88D Ambiguity Resolution: Phase coding and staggered PRT. NOAA/NSSL Report, Part 9, 112 pp.

Torres S., M. Sachidananda, and D. Zrnić, 2007: Signal Design and Processing Techniques for WSR-88D Ambiguity Resolution: Staggered PRT and updates to the SZ-2 algorithm. NOAA/NSSL Report, Part 11, 146 pp.

Torres, S., D. Zittel, and D. Saxion, 2009: Update on Development of Staggered PRT for the NEXRAD Network. Preprints, 25th International Conference on Interactive Information and Processing Systems (IIPS) for Meteorology, Oceanography, and Hydrology, Phoenix, AZ, Amer. Meteor. Soc., Paper 11B.2.

Torres, S., Y. Dubel, and D. S. Zrnić, 2004: Design, implementation, and demonstration of a staggered PRT algorithm for the WSR-88D. *J. Atmos. Oceanic Technol*., **21**, 1389-1399.

Torres, S.M., and D.S. Zrnić, 2003a: Whitening in range to improve weather radar spectral moment estimates. Part I: Formulation and simulation. *J. Atmos. Oceanic Technol.*, **20**, 1443-1448.

Torres, S.M., and D.S. Zrnić, 2003b: Whitening of signals in range to improve estimates of polarimetric variables. *J. Atmos. Oceanic Technol.*, **20**, 1776-1789.

WSR-88D System Specifications 2810000H, 25 April 2008, Radar Operations Center, 160 pp.

Zrnić, D. S., 1975: Simulation of weather like Doppler spectra and signals, *Journal of Applied Meteorology*, **14**, No. 4, 619-620.

LIST OF NSSL REPORTS FOCUSED ON POSSIBLE UPGRADES

TO THE WSR-88D RADARS

Torres S., M. and D. Zrnić, 2007: Signal Design and Processing Techniques for WSR-88D Ambiguity Resolution: Evolution of the SZ-2 Algorithm. NOAA/NSSL Report, Part 11, 145 pp.

Zrnić, D.S., Melnikov, V. M., J. K. Carter, and I. Ivić, 2007: Calibrating differential reflectivity on the WSR-88D, (Part 2). NOAA/NSSL Report, 34 pp.

Torres S., M. and D. Zrnić, 2006: Signal Design and Processing Techniques for WSR-88D Ambiguity Resolution: Evolution of the SZ-2 Algorithm. NOAA/NSSL Report, Part 10, 71 pp.

Torres S., M. Sachidananda, and D. Zrnić, 2005: Signal Design and Processing Techniques for WSR-88D Ambiguity Resolution: Phase coding and staggered PRT. NOAA/NSSL Report, Part 9, 112 pp.

Zrnić, D.S., Melnikov, V.M., and J.K. Carter, 2005: Calibrating differential reflectivity on the WSR-88D. NOAA/NSSL Report, 34 pp.

Torres S., M. Sachidananda, and D. Zrnić, 2004: Signal Design and Processing Techniques for WSR-88D Ambiguity Resolution: Phase coding and staggered PRT: Data collection, implementation, and clutter filtering. NOAA/NSSL Report, Part 8, 113 pp.

Zrnić, D., S. Torres, J. Hubbert, M. Dixon, G. Meymaris, and S. Ellis, 2004: NEXRAD range-velocity ambiguity mitigation. SZ-2 algorithm recommendations. NCAR-NSSL Interim Report.

Melnikov, V, and D Zrnić, 2004: Simultaneous transmission mode for the polarimetric WSR-88D – statistical biases and standard deviations of polarimetric variables. NOAA/NSSL Report, 84 pp.

Bachman, S., 2004: Analysis of Doppler spectra obtained with WSR-88D radar from non-stormy environment. NOAA/NSSL Report, 86 pp.

Zrnić, D., S. Torres, Y. Dubel, J. Keeler, J. Hubbert, M. Dixon, G. Meymaris, and S. Ellis, 2003: NEXRAD range-velocity ambiguity mitigation. SZ(8/64) phase coding algorithm recommendations. NCAR-NSSL Interim Report.

Torres S., D. Zrnić, and Y. Dubel, 2003: Signal Design and Processing Techniques for WSR-88D Ambiguity Resolution: Phase coding and staggered PRT: Implementation, data collection, and processing. NOAA/NSSL Report, Part 7, 128 pp.

Schuur, T., P. Heinselman, and K. Scharfenberg, 2003: Overview of the Joint Polarization Experiment (JPOLE), NOAA/NSSL Report, 38 pp.

Ryzhkov, A, 2003: Rainfall Measurements with the Polarimetric WSR-88D Radar, NOAA/NSSL Report, 99 pp.

Schuur, T., A. Ryzhkov, and P. Heinselman, 2003: Observations and Classification of echoes with the Polarimetric WSR-88D radar, NOAA/NSSL Report, 45 pp.

Melnikov, V., D. Zrnić, R. J. Doviak, and J. K. Carter, 2003: Calibration and Performance Analysis of NSSL's Polarimetric WSR-88D, NOAA/NSSL Report, 77 pp.

NCAR-NSSL Interim Report, 2003: NEXRAD Range-Velocity Ambiguity Mitigation SZ(8/64) Phase Coding Algorithm Recommendations.

Sachidananda, M., 2002: Signal Design and Processing Techniques for WSR-88D Ambiguity Resolution, NOAA/NSSL Report, Part 6, 57 pp.

Doviak, R., J. Carter, V. Melnikov, and D. Zrnić, 2002: Modifications to the Research WSR-88D to obtain Polarimetric Data, NOAA/NSSL Report, 49 pp.

Fang, M., and R. Doviak, 2001: Spectrum width statistics of various weather phenomena, NOAA/NSSL Report, 62 pp.

Sachidananda, M., 2001**:** Signal Design and Processing Techniques for WSR-88D Ambiguity Resolution, NOAA/NSSL Report, Part 5, 75 pp.

Sachidananda, M., 2000**:** Signal Design and Processing Techniques for WSR-88D Ambiguity Resolution, NOAA/NSSL Report, Part 4, 99 pp.

Sachidananda, M., 1999**:** Signal Design and Processing Techniques for WSR-88D Ambiguity Resolution, NOAA/NSSL Report, Part 3, 81 pp.

Sachidananda, M., 1998**:** Signal Design and Processing Techniques for WSR-88D Ambiguity Resolution, NOAA/NSSL Report, Part 2, 105 pp.

Torres, S., 1998: Ground Clutter Canceling with a Regression Filter, NOAA/NSSL Report, 37 pp.

Doviak, R. and D. Zrnić, 1998**:** WSR-88D Radar for Research and Enhancement of Operations: Polarimetric Upgrades to Improve Rainfall Measurements, NOAA/NSSL Report, 110 pp.

Sachidananda, M., 1997**:** Signal Design and Processing Techniques for WSR-88D Ambiguity Resolution, NOAA/NSSL Report, Part 1, 100 pp.

Sirmans, D., D. Zrnić, and M. Sachidananda, 1986**:** Doppler radar dual polarization considerations for NEXRAD, NOAA/NSSL Report, Part I, 109 pp.

Sirmans, D., D. Zrnić, and N. Balakrishnan, 1986**:** Doppler radar dual polarization considerations for NEXRAD, NOAA/NSSL Report, Part II, 70 pp.

Appendix A. Staggered PRT Algorithm Description (May 2008)

A.1. Assumptions

1) The transmission sequence alternates two pulse repetition times (PRT) as: T_1, T_2, T_1, T_2, … for a total of M pulses.

2) The PRT ratio $\min(T_1,T_2)/\max(T_1,T_2) = \kappa_m/\kappa_n$ is larger than 1/3, where κ_m and κ_n are relatively prime integers.

3) All range gates are available and there is a perfect alignment of range gates between the two PRTs (i.e., a given range gate represents the same resolution volume in space for every transmitted pulse). Also, the number of range gates for each PRT is: $N_1 = T_1/\tau_s$ and $N_2 = T_2/\tau_s$, where τ_s is the sampling period.

4) There are no significant echoes beyond $\max(r_{a1}, r_{a2})$, where r_{ai} is the maximum unambiguous range corresponding to T_i

5) It is *not* assumed that M is even or that $T_1 < T_2$.

A.2. Inputs

1) Complex time-series data:

$V(n,m) = I(n,m) + jQ(n,m)$, where $0 \leq n < N_1$ for even m, $0 \leq n < N_2$ for odd m, and $0 \leq m < M$. Note that n indexes the range gates and m the sweeps (or pulses).

2) Associated metadata:

N is the noise power in linear units
dBZ0 is the system calibration constant in dB
ATMOS is the elevation-dependent atmospheric attenuation in dB/km

3) Ground clutter filter bypass map:

$B(n)$, where n indexes the range bins with the same resolution as the time-series data along a radial, and the map corresponds to the elevation and azimuth of the radial being processed. B is 0 if clutter filtering is required and 1 otherwise.

A.3. Outputs

1) Reflectivities, Doppler velocities, and spectrum widths:

$Z(n)$	for $0 \leq n < \max(N_1,N_2)$,
$v(n)$ and $w(n)$	for $0 \leq n < \max(N_1,N_2)$.

2) Signal-to-noise ratio and overlaid censoring flags:

$NS_Z(n)$, $NS_V(n)$ and $NS_W(n)$	for $0 \leq n < \max(N_1,N_2)$,
$OV_V(n)$ and $OV_W(n)$	for $0 \leq n < \max(N_1,N_2)$.

A.4. High-level Algorithm description

If the PRT ratio has changed
1. Pre-computation of velocity de-aliasing rules

End
For each range bin n, where $0 \leq n < \max(N_1,N_2)$
2. Clutter filtering
3. Power and correlation computations for each PRT

End
4. Short/long PRT data swap

For each range bin n, where $0 \leq n < N_2$
5. Combined power computation

End
6. Strong point clutter canceling

For each range bin n, where $0 \leq n < N_2$
7. Signal power computation
8. Reflectivity computation
9. Velocity computation
10. Spectrum width computation
11. Determination of significant returns for reflectivity
12. Determination of significant returns for velocity
13. Determination of significant returns for spectrum width

End
For each range bin n, where $0 \leq n < N_2$
14. Determination of overlaid returns for velocity and spectrum width

End

A.5. Step-by-step algorithm description

1. *Pre-computation of velocity de-aliasing rules*

This method is described in the paper "Design, Implementation, and Demonstration of a Staggered PRT Algorithm for the WSR-88D" by Torres et al. (2004). Herein, VDA_c are the normalized velocity difference transfer function (VDTF) constant values and VDA_p are the normalized number of Nyquist co-intervals for de-aliasing.

A set of velocity de-aliasing rules could be pre-computed for <u>each new PRT ratio</u> as follows:

(Compute type-I and II positive (VDTF) discontinuity points. κ_m and κ_n are the integers in the PRT ratio)
$p = 0$
While $2p + 1 < \kappa_m$
    $D_1(p) = (2p + 1)/\kappa_m$
    $TYPE_1(p) = 1$
    $p = p + 1$
End
$q = 0$
While $2q + 1 < \kappa_n$
    $D_2(q) = (2q + 1)/\kappa_n$
    $TYPE_2(q) = 2$
    $q = q + 1$
End

(Create TYPE by combining and sorting and both sets of discontinuity points)
Concatenate D_1 and D_2 to create D with $p + q$ elements.
Concatenate $TYPE_1$ and $TYPE_2$ to create $TYPE$ with $p + q$ elements.
Sort $TYPE$ in a "slave" mode using D as the "master".

(Compute VDTF constants and de-aliasing factors for non-negative discontinuity points)
$VDA_c(p + q) = 0$
$VDA_p(p + q) = 0$

For $0 \le k < p + q$
    If $TYPE(k) = 1$
        $VDA_c(p + q + k + 1) = VDA_c(p + q + k) - 2/\kappa_m$
        $VDA_p(p + q + k + 1) = VDA_p(p + q + k) + 1/\kappa_m$
    Else
        $VDA_c(p + q + k + 1) = VDA_c(p + q + k) + 2/\kappa_n$
        $VDA_p(p + q + k + 1) = VDA_p(p + q + k)$
    End
End

(Compute VDTF constants and de-aliasing factors for negative discontinuity points)
For $-(p + q) \le k < 0$
    $VDA_c(p + q + k) = -VDA_c(p + q - k)$
    $VDA_p(p + q + k) = -VDA_p(p + q - k)$
End

2. *Clutter filtering*

The clutter filtering algorithm removes the mean (or DC) component of V in those locations where the site-dependent clutter filter bypass map B indicates the need for clutter filtering (here, it is assumed that B corresponds to the azimuth and elevation of the current time-series data). V_m is the DC component of V computed using all sweeps where available, and only long-PRT sweeps beyond the short PRT.

If $B(n) = 0$
    (Clutter filtering is required)
    $V_{sum} = 0$
    $K = 0$
    If $n < N_1$
        (Accumulate even pulses, if available)
        $$V_{sum} = V_{sum} + \sum_{m=0}^{K_s^{(1)}-1} V(n, 2m)$$
        $$K = K + K_s^{(1)}$$
    End
    If $n < N_2$
        (Accumulate odd pulses, if available)
        $$V_{sum} = V_{sum} + \sum_{m=0}^{K_s^{(2)}-1} V(n, 2m+1)$$
        $$K = K + K_s^{(2)}$$
    End

(Compute mean using total number of pulses accumulated)
$V_m = V_{sum} / K$
Else
(Clutter filtering is not required)
$V_m = 0$
End

(Apply ground clutter filtering, if needed)
If $n < N_1$
(Subtract mean from even pulses, if available)
For $0 \le m < K_s^{(1)}$
$V_F(n, 2m) = V(n, 2m) - V_m$
End
End
If $n < N_2$
(Subtract mean from odd pulses, if available)
For $0 \le m < K_s^{(2)}$
$V_F(n, 2m+1) = V(n, 2m+1) - V_m$
End
End

3. *Power and correlation computations for each PRT*

If $n < N_1$
(Compute power from even pulses, if available)

$$P_1(n) = \frac{1}{K_s^{(1)}} \sum_{m=0}^{K_s^{(1)}-1} \left| V_F(n, 2m) \right|^2$$

End
If $n < N_2$
(Compute power from odd pulses, if available)

$$P_2(n) = \frac{1}{K_s^{(2)}} \sum_{m=0}^{K_s^{(2)}-1} \left| V_F(n, 2m+1) \right|^2$$

End

If $n < \min(N_1, N_2)$
(Compute lag-1correlations from all pulses, if available)

$$R_1(n) = \frac{1}{K_p^{(1)}} \sum_{m=0}^{K_p^{(1)}-1} V_F^*(n, 2m) V_F(n, 2m+1)$$

$$R_2(n) = \frac{1}{K_p^{(2)}} \sum_{m=0}^{K_p^{(2)}-1} V_F^*(n, 2m+1) V_F(n, 2m+2)$$

End

In the previous equations, K_s is the number of sweeps (pulses) used in the power computations, and K_p is the number of pairs used in the lag-1 correlation computations. These constants depend on the total number of sweeps M, and they may differ for short and long PRT estimates depending on the parity of M as

$$K_s^{(1)} = \begin{cases} \frac{M}{2} & \text{if } M \text{ is even} \\ \frac{M+1}{2} & \text{if } M \text{ is odd} \end{cases}, \quad K_s^{(2)} = \begin{cases} \frac{M}{2} & \text{if } M \text{ is even} \\ \frac{M-1}{2} & \text{if } M \text{ is odd} \end{cases},$$

$$K_p^{(1)} = \begin{cases} \frac{M}{2} & \text{if } M \text{ is even} \\ \frac{M-1}{2} & \text{if } M \text{ is odd} \end{cases}, \text{ and } \quad K_p^{(2)} = \begin{cases} \frac{M-2}{2} & \text{if } M \text{ is even} \\ \frac{M-1}{2} & \text{if } M \text{ is odd} \end{cases}.$$

4. *Short/long PRT data swap*

This step is done to simplify the logic of the algorithm by making all variables with subscript 1 correspond to the short PRT, and variables with subscript 2 correspond to the long PRT.

If $T_2 < T_1$
    Swap P_1, R_1, T_1, and N_1 with P_2, R_2, T_2, and N_2 , respectively
End

5. *Combined power computation*

To use as much information as possible, data are extracted from the two power arrays with different rules for each of the three segments depicted in Fig. 1. For segment I, data are extracted only from P_1, since P_2 may be contaminated on those range bins with overlaid powers. An average of P_1 and P_2 is extracted for segment II, given that both power vectors are "clean" there. Finally, segment III data are obtained from P_2. In algorithmic form,

If $n < \min(N_1, N_2 - N_1)$
    (Segment I)
    $P(n) = P_1(n)$
ElseIf $n < N_1$
    (Segment II)
    $P(n) = \frac{1}{2}\left[P_1(n) + P_2(n)\right]$
Else
    (Segment III)
    $P(n) = P_2(n)$
End

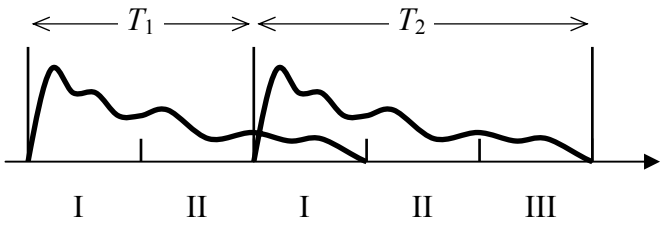

Fig. A.1. Signal powers in the staggered PRT algorithm. Roman numerals indicate segment numbers.

6. ***Strong point clutter canceling***

Processing is as in the current system. Strong-point clutter canceling is applied to P, R_1, and R_2 based on P powers.

7. ***Signal power computation***

If $P(n) < N$
    $S = 0$
Else
    $S = P(n) - N$
End

N is the noise power in linear units

8. ***Reflectivity computation***

(Range in km)
$R = n\Delta R + \Delta R/2$
(Reflectivity in dBZ)
$Z(n) = 10\log_{10}(S) + dBZ0 + R\ ATMOS + 20\log_{10}(R) - 10\log_{10}(N)$,

where ΔR is the spacing between range gates in km ($\Delta R = c\,\tau_s/2$), *dBZ0* is the system calibration constant in dB, *ATMOS* is the atmospheric attenuation in dB/km depending on the antenna elevation angle, and N is the noise power in linear units.

9. *Velocity computation*

If $n < N_1$

(Compute Doppler velocities for each PRT using the corresponding correlation estimates)

$$v_1 = -\frac{\lambda}{4\pi T_1}\arg\left[R_1(n)\right]$$

$$v_2 = -\frac{\lambda}{4\pi T_2}\arg\left[R_2(n)\right]$$

(Compute extended Nyquist velocity)

$$v_a = \frac{\lambda \kappa_m}{4T_1}$$

(De-alias velocity using pre-computed rules)

$$l = \arg\min_k \left| v_1 - v_2 - VDA_c(k) v_a \right|$$

$$v(n) = v_1 + 2v_a \ VDA_p(l)$$

Else

(This value is irrelevant)

$v(n) = 0$

End

10. *Spectrum width computation*

The spectrum width estimator corresponds to the algorithm implemented in the legacy WSR-88D signal processor. N is the noise power in linear units.

If $n < N_1$

If $S = 0$

(Spectrum width of white noise)

$$w(n) = \frac{\lambda}{4\sqrt{3}T_1}$$

ElseIf $S < \left|R_1(n)\right|$

(Spectrum width of a constant)

$w(n) = 0$

Else

$$w(n) = \frac{\lambda}{2\sqrt{2}\pi T_1}\sqrt{\ln\left(\frac{S}{\left|R_1(n)\right|}\right)}$$

End

Else
    (This value is irrelevant)
    $w(n) = 0$
End

11. ***Determination of significant returns for reflectivity***

The non-significant return indicator array (*NS*) is a binary array where 0 indicates "significant" and 1 indicates "non-significant"

If $S < N10^{0.1T_Z}$
    $NS_Z(n) = 1$
Else
    $NS_Z(n) = 0$
End

T_Z is the reflectivity threshold in dB and N is the noise power in linear units.

12. ***Determination of significant returns for velocity***

The non-significant return indicator array (*NS*) is a binary array where 0 indicates "significant" and 1 indicates "non-significant"

If $S < N10^{0.1T_V}$
    $NS_V(n) = 1$
Else
    $NS_V(n) = 0$
End

T_V is the velocity threshold in dB and N is the noise power in linear units.

13. ***Determination of significant returns for spectrum width***

The non-significant return indicator array (*NS*) is a binary array where 0 indicates "significant" and 1 indicates "non-significant"

If $S < N10^{0.1T_W}$
    $NS_W(n) = 1$
Else
    $NS_W(n) = 0$
End

T_W is the spectrum width threshold in dB and N is the noise power in linear units.

14. *Determination of overlaid returns for velocity and spectrum width*

Censoring of velocity and spectrum width data is only necessary in segment I. This is done by analyzing P in segment I (P_1) and P in segment III (P_2) (see Fig. 1). The idea is to determine whether second trip signals mask first trip signals in segment I of P_2. While such overlaid echoes appear in every other pulse and do not bias velocity estimates at those range locations, overlaid powers act as noise. Therefore, when second trip powers in segment I of P_2 are above a preset fraction of their first trip counterparts, the corresponding velocity and spectrum width estimates exhibit very large errors and must be censored. The overlaid indicator array (OV) is a binary array where 0 indicates "not overlaid" and 1 indicates "overlaid". Herein, T_O is the overlaid threshold in dB which is sometimes referred to as TOVER.

If $n < \min(N_1, N_2 - N_1)$
    (Segment I: Range gates that may or may not have overlaid echoes)
    (Check power ratio first)
    If $P(n) > P(n + N_1)\ 10^{0.1T_O}$
        $OV_V(n) = 0$
        $OV_W(n) = 0$
    Else
        (Power ratio not met, but consider non-significant returns as non existent)
        If $NS_V(n + N_1) = 1$
            $OV_V(n) = 0$
        Else
            $OV_V(n) = 1$
        End
        If $NS_V(n + N_1) = 1$
            $OV_W(n) = 0$
        Else
            $OV_W(n) = 1$
        End
    End

ElseIf $n < N_1$

(Segment II: Range gates that, based on our assumptions, never have overlaid echoes)

$OV_V(n) = 0$

$OV_W(n) = 0$

Else

(Segment III: Range gates that are always unrecoverable)

$OV_V(n) = 1$

$OV_W(n) = 1$

End

Note that when processing the overlaid and significant return flags, the overlaid flags take a lower priority. That is, if a range bin is tagged as non significant and also as overlaid, the overlaid indication is ignored and the gate is treated as a non-significant return only (e.g., painted black as opposed to purple).

Appendix B. Staggered PRT VCP Definitions

Table B.2 contains the recommended VCP for staggered PRT based on the criteria presented in Section 3.2. This VCP is based on the operational VCP 12 but the dwell times at the intermediate and upper elevations have been about doubled to meet spectral moment standard error and ground clutter filter requirements. With these longer dwell times, the VCP time is about 5 minutes and 48 seconds. Note that the PRTs for the SPRT waveform are indexed from Table B.1.

PRI	T_1 (μs)	T_2 (μs)
1	1740	2610
2	1617	2426
3	1494	2241
4	1371	2057
5	1248	1872
6	1125	1688
7	1002	1503
8	882	1323

Table B.1. PRI table for the SPRT waveform.

Unlike with other ORDA techniques, the performance of SPRT is intimately tied to the VCP definition. Hence, designing effective VCPs that exploit SPRT is a crucial task. We recommend that the ROC implements this VCP and uses it for data collection on the KCRI testbed as soon as possible.

As future work, we will do similar modifications to other operational range-and-velocity-ambiguity-mitigation VCPs so that the Batch mode and contiguous Doppler tilts are replaced with SPRT.

VCP X

Angle (°)	AZ Rate (deg/s)	Period (sec)	WF Type	PRI #	No. Pulses	PRI #	No. Pulses	T_1 (ms)	T_2 (ms)	DT (ms)	$r_{a,S}$ (km)	$r_{a,D}$ (km)	v_a (m/s)	$\sigma_{v,max}$ (m/s)	SD(Z) (dB)*	SD(v) (m/s)	r_{max} (km)
0.50	21.46	16.78	CS	1	15			3.11		46.60	466				0.62		533
0.50	25.34	14.21	CD			5	40		0.99	39.47		148	26.7	16.3		1.07	533
0.90	21.46	16.78	CS	1	15			3.11		46.60	466				0.62		484
0.90	25.34	14.21	CD			5	40		0.99	39.47		148	26.7	16.3		1.07	484
1.30	21.46	16.78	CS	1	15			3.11		46.60	466				0.62		440
1.30	25.34	14.21	CD			5	40		0.99	39.47		148	26.7	16.3		1.07	440
1.80	16.30	22.08	SPRT			1	28	1.75	2.63	61.34	394	263	30.0	8.7	0.56	0.99	392
2.40	16.62	21.66	SPRT			3	32	1.50	2.26	60.16	338	225	35.0	10.4	0.56	0.99	344
3.10	16.10	22.36	SPRT			4	36	1.38	2.07	62.10	310	207	38.1	11.5	0.54	0.97	298
4.00	16.06	22.41	SPRT			6	44	1.13	1.70	62.26	255	170	46.5	14.4	0.54	0.99	252
5.10	15.12	23.81	SPRT			8	60	0.88	1.32	66.15	198	132	59.6	19.2	0.51	1.00	211
6.40	15.12	23.81	SPRT			8	60	0.88	1.32	66.15	198	132	59.6	19.2	0.51	1.00	175
8.00	15.12	23.81	SPRT			8	60	0.88	1.32	66.15	198	132	59.6	19.2	0.51	1.00	145
10.00	15.12	23.81	SPRT			8	60	0.88	1.32	66.15	198	132	59.6	19.2	0.51	1.00	118
12.50	15.12	23.81	SPRT			8	60	0.88	1.32	66.15	198	132	59.6	19.2	0.51	1.00	96
15.60	15.12	23.81	SPRT			8	60	0.88	1.32	66.15	198	132	59.6	19.2	0.51	1.00	78
19.50	15.12	23.81	SPRT			8	60	0.88	1.32	66.15	198	132	59.6	19.2	0.51	1.00	63
	VCP Time	*5.80*	*min*														

Table B.2. Recommended VCP for SPRT based on the tilts of VCP 12 (VCP X). PRI numbers for the SPRT waveform (WF) are listed in Table B.1. Standard deviations of reflectivity and Doppler velocity are approximated. Standard deviation of reflectivity estimates are based on the worst case scenario and include range averaging. The maximum range of storms (r_{max}) is for a maximum storm height of 70 kft.

Appendix C. 2008 European Radar Conference Paper

(Paper follows next in its original format)

Range and velocity ambiguity mitigation on the US NEXRAD network: performance and improvements of the SZ-2 phase coding algorithm

Sebastián M. Torres,
University of Oklahoma/CIMMS and NOAA/National Severe Storms Lab, Norman, Oklahoma, USA

1. Introduction

It is well known that for Doppler radars transmitting uniformly spaced pulses there is a coupling between the maximum unambiguous range and velocity. That is, one can only be increased at the expense of a proportional decrease of the other. Because this fundamental limitation hinders observation of severe weather phenomena, the Radar Operations Center of the US National Weather Service has sponsored the National Severe Storms Laboratory (NSSL) and the National Center for Atmospheric Research (NCAR) to develop methods for mitigating the effects of velocity and range ambiguities on the NEXRAD network. In a joint effort, NSSL and NCAR have recently recommended an algorithm for the initial deployment of range and velocity ambiguity mitigation techniques on the radars' new signal processors. The algorithm, referred to as SZ-2, is based on systematic phase coding that uses the SZ(8/64) code and operates at the lowest elevation angles of the antenna beam.

This paper shows the performance of the SZ-2 algorithm, discusses a few surprises that surfaced after its operational implementation, and describes proposed improvements.

2. The SZ-2 Algorithm

Sachidananda and Zrnić (1999) proposed the SZ phase code as a better alternative to random codes (e.g., Laird 1981). SZ phase coding is similar to random phase coding except that the transmitted pulses are phase-modulated with a systematic code consisting of M phases that repeat periodically. These codes exhibit properties that make them attractive for the separation of overlaid signals in the spectral domain. That is, if the received signal is cohered for a given trip, the spectra of all out-of-trip echoes consist of evenly spaced replicas of their corresponding coherent spectra. Hence, out-of-trip echoes do not bias the mean Doppler velocity estimate of the coherent signal. Once the velocity is recovered for the strong-trip, the coherent signal is notched out such that the two least contaminated replicas of the out-of-trip (i.e., the weak trip) echo remain. These two replicas are sufficient to reconstruct (or "recohere") the weak-trip echo and recover its mean Doppler velocity. From the family of SZ(n/M) codes, the SZ(8/64) code was selected for NEXRAD as it gives the best performance in terms of recovery of overlaid signals that are separated by one trip (Sachidananda et al. 1998).

Recovery of strong and weak trip signals can proceed in a stand-alone manner (referred to as the SZ-1 algorithm) or with the aid of an extra scan at the same elevation angle using a long pulse repetition time (PRT) (referred to as the SZ-2 algorithm). Although the latter results in longer acquisition times due to the extra scan, long-PRT data provides non-overlaid power information that is essential in the determination of the location and strength of overlaid trips for the short-PRT scan. Having the long-PRT information available makes the SZ-2 algorithm computationally simpler and more effective than its stand-alone counterpart. Whereas the long-PRT data provides the reflectivity free of range ambiguities, the short-PRT data is used to compute Doppler velocities associated with the two strongest overlaid signals.

The SZ-2 algorithm, which is currently implemented on the US network of weather surveillance radars since the Spring of 2007 (Saffle et al. 2007), incorporates a set of censoring rules to maintain data quality under situations that preclude the recovery of one or more overlaid echoes (Saxion et al. 2007, Ellis et al. 2005). Base data displays characterize this failure by encoding those range locations with overlaid powers using a purple color, normally referred to as the "purple haze".

3. Performance of the SZ-2 Algorithm

Fig. 1 shows an example of the reduction in range folded Doppler velocity data using the SZ-2 algorithm in VCP 212 (right) in comparison with the legacy VCP 12 (left). The VCP 212 data at the 0.5 deg elevation was collected by the KCRI radar (a test WSR-88D) in Norman, Oklahoma. The VCP 12 data at the 0.5 deg elevation was collected at nearly the same time on the KTLX radar at Twin Lakes, Oklahoma. A clear tornado signature is visible in the VCP 212 data whereas it is unfortunately obscured by purple haze on the VCP 12 data.

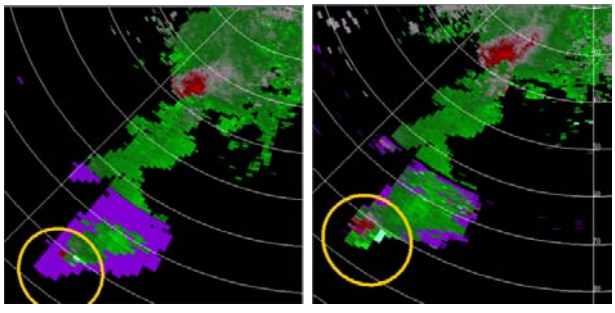

Fig. 1. Doppler velocity fields for 0.5 deg elevation collected on April 25, 2006 at about 01:33 UTC during a tornado event in central Oklahoma. The image on the left comes from the operational KTLX (legacy) and the one on the right from the test KCRI (SZ-2).

Corresponding address: Sebastian Torres, CIMMS and NSSL, Norman, OK. Sebastian.Torres@noaa.gov.

Fig. 2 illustrates the first operational selection of a scanning strategy based on the SZ-2 algorithm. The event corresponds to a mesoscale convective system (MCS) observed by the KTLX radar from Twin Lakes, OK on March 30, 2007 at about 19:40 UTC. The two Doppler velocity fields shown in this figure correspond to the times before and after switching from VCP 12 (legacy) to VCP 212 (SZ-2). As expected, Doppler velocity displays obtained with legacy-type processing are significantly obscured by the purple haze which indicates the presence of unresolvable overlaid echoes. On the other hand, the SZ-2 algorithm successfully recovers velocities of the two strongest overlaid echoes.

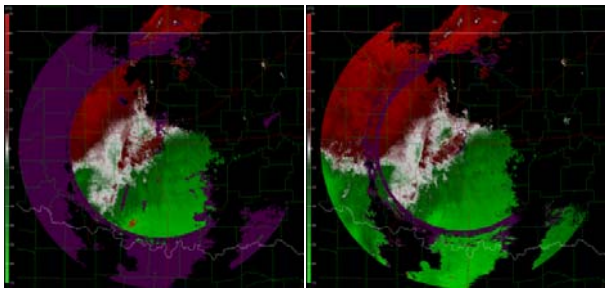

Fig 2. KTLX Doppler velocity fields for 0.5 deg elevation collected operationally on March 30, 2007 at 19:37 and 19:42 UTC during a severe storm event in central Oklahoma. The image on the left corresponds to a legacy VCP and the one on the right to an SZ-2 VCP.

4. Updates to the SZ-2 Algorithm

As mentioned before, the SZ-2 algorithm has been implemented and is now operational providing significant reduction of obscuration (purple haze) at the lower elevation angles on the NEXRAD network. Although the initial algorithm recommendation was extensively tested in a research environment (Torres 2005), a number of issues arose during 2007, after its operational implementation. These are discussed next.

4.2. Fourth-Trip Overlaid Echoes

One significant issue reported from the field was related to noisy velocities observed by the KCRI radar in Norman, OK for two cases in June of 2007. The common thread in these two cases was the occurrence of 4th and 1st trip overlaid echoes. The reflectivity field shown in Fig. 3 can be used to verify that indeed, this is a case of 4th and 1st trip overlaid echoes with no significant 2nd or 3rd trips, a situation that may be common operationally, but that had not occurred before in our test cases. The corresponding Doppler velocity field is also shown in Fig 2 in which the patch of noisy velocities to the west of the radar is evident. With a little detective work, we can see that the patch of noisy velocities correspond to a 4th-trip strong signal and a 1st-trip weak signal; hence, the noisy velocities that we observe in the 1st trip correspond to weak-trip recovery.

In SZ-2, a processing notch filter (PNF) is designed to remove most of the strong-trip signal while leaving two replicas of the weak-trip modulated signal for further recovery. In the case of 1st and 2nd trip overlay (herein referred to as 1-2 overlay), the modulated weak trip has eight replicas, so a PNF that removes ¾ of the spectrum and retains ¼ is ideal. In the case of 1st and 3rd trip overlay (herein referred to as 1-3 overlay), the modulated weak trip has four replicas, so the PNF has to be adjusted to remove only ½ of the spectrum to retain the required two replicas. Finally, for the case of 1st and 4th trip overlay (herein referred to as 1-4 overlay), the modulated weak trip has eight replicas and, again, a ¾ notch is feasible. Fig. 4 depicts the placement and width of the PNF for the 1-2, 1-3, and 1-4 overlay situations. Also, this figure shows the spectrum of the re-cohered 2nd trip weak signal. Note that the main lobe corresponds to the true placement of the weak signal spectrum; however, there are decaying sidebands that do not bias the weak-trip velocity estimate but act as white noise, increasing the errors of estimates. Closer examination of one of the range locations with evident noise reveals that the recovered 1st trip spectrum (weak trip) does not seem to have the expected main lobe with decaying sidelobes! (see Fig. 5).

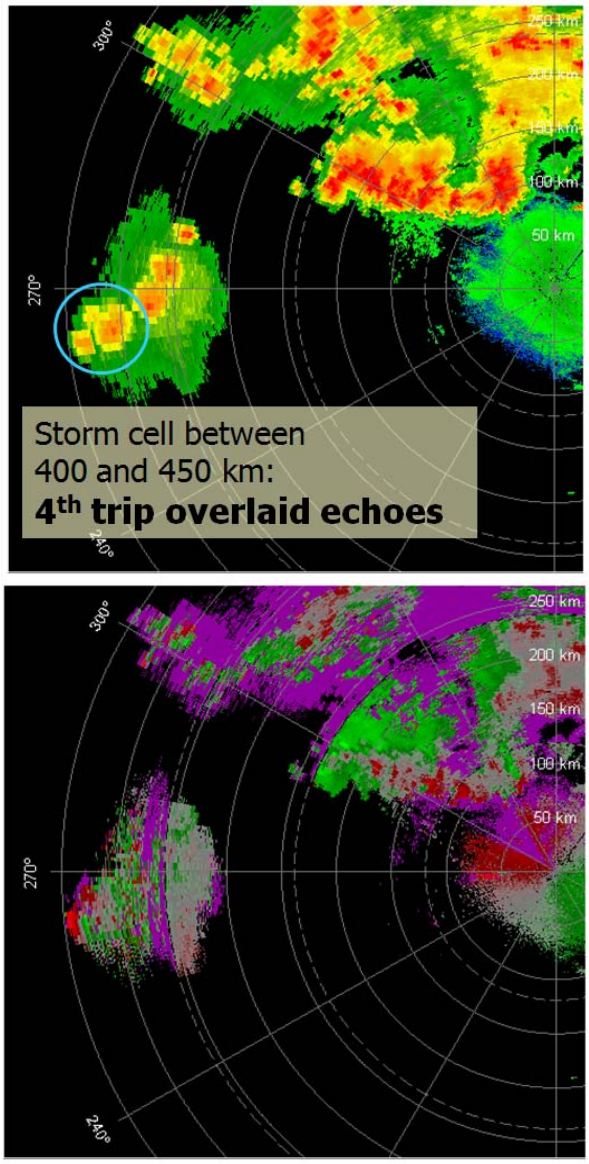

Fig. 3. Reflectivity (top) and Doppler velocity (bottom) fields collected with the KCRI radar in Norman, OK on June 20, 2007.The maximum unambiguous ranges corresponding to the long and short PRTs are 471 and 119 km.

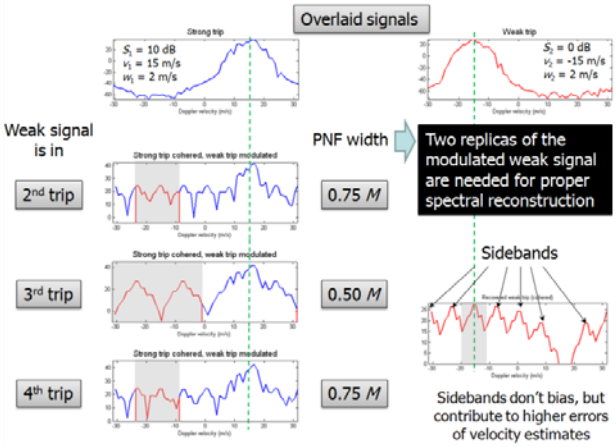

Fig. 4. Application of the processing notch filter (PNF) for different overlay cases in the SZ-2 algorithm to reconstruct the weak-trip signal spectrum.

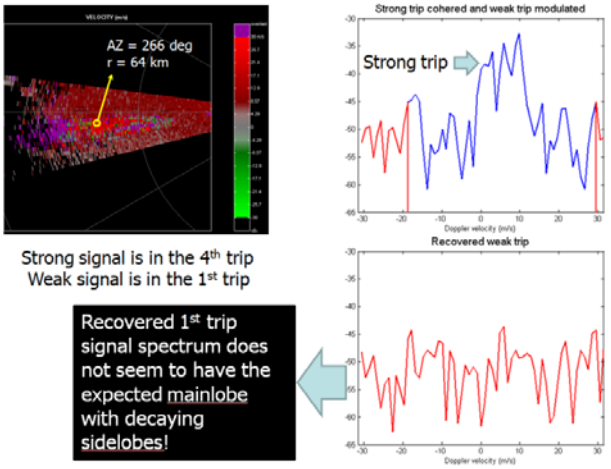

Fig. 5. Spectra corresponding to a range gate with noisy velocity. The top-right panel shows the spectrum of the strong-trip cohered signal and the lower-right panel shows the spectrum of the recovered weak-trip signal.

A closer look at the spectra of the recovered weak trip in the 1-2, 1-3, and 1-4 overlay situations reveals the key to this problem. Fig. 6 shows the spectra of the modulation phase codes before and after the application of the PNF. Whereas, the 1-2 and 1-3 overlay cases exhibit *decaying* sidebands, this is not true for the 1-4 overlay case. Further, a statistical analysis of the recovery of weak-trip velocities reveals that if strong and weak signals are 3 trips apart (e.g., 1st and 4th trips), recovery of the weak-trip velocity is not possible (i.e., errors of estimates are very large). This can be intuitively explained by computing the normalized spectrum width of the modulation code of the recovered weak trip signal. This number is a good indicator of the "spread" of the spectrum, which in turn is associated with the errors of velocity estimates. For the 1-2, 1-3, and 1-4 overlay cases, the normalized spectrum width (σ_{vn}) is 0.1855, 0.1855, and 0.5305, respectively. Hence, the normalized spectrum width in the 1-4 overlay case is about 3 times larger than in the 1-2 or 1-3 cases, which explains the much larger errors of estimates observed both in simulations and real data.

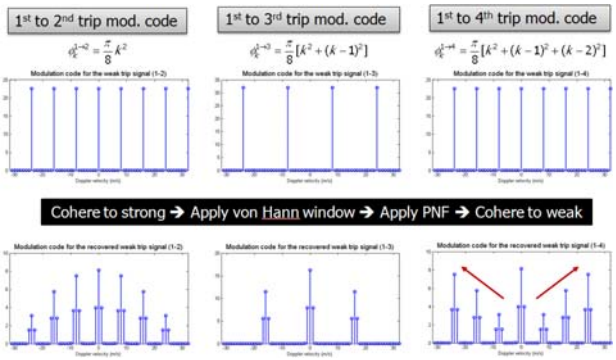

Fig. 6. Spectra of the modulated code for the weak-trip signal and for the recovered weak-trip signal after windowing, notching, and re-cohering for different overlay cases.

An easy solution to this problem consists on reducing the PNF notch width to reduce the normalized spectrum width of the modulation code of the recovered weak signal. A PNF notch width of 5*M*/8 results in an even larger value, σ_{vn} = 0.5610, whereas a notch width of *M*/2 (same as in the 1-3 overlay case) results in σ_{vn} = 0.2637, which is much closer to the values observed in the 1-2 and 1-3 overlay cases. With this simple change, it is now possible to recover the weak-trip velocity if the overlaid signals are three trips apart.

In summary, proper recovery of the weak trip in the case of 1-4 overlay requires a processing notch filter narrower than initially assumed. This change is currently being implemented for future releases of the operational signal processing software. The change will improve the recovery of weak overlaid echoes in those cases where the strong-to-weak trip difference is three. Fig. 7 shows the same case in Fig. 3 processed with and without this change. It is evident that recovery of the weak 1st trip velocities is now feasible. However, we can still observe noisy velocities in this and in other areas of the field. This issue is addressed next.

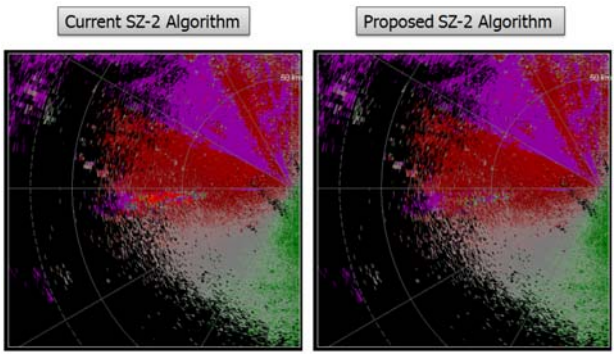

Fig. 7. Doppler velocity fields for the June 20, 2007 case using the current and modified SZ-2 algorithms.

4.3. Recovery Region Censoring

Since its operational implementation, Doppler velocity fields produced with the SZ-2 algorithm have been characterized by users as "noisier". On one hand, it was accepted that errors of weak-trip velocity estimates would be larger. In fact, never before had the NEXRAD system

been able to recover Doppler velocities of weak-trip overlaid echoes. Due to the great operational gain associated with the SZ-2 algorithm, the NEXRAD Technical Requirement (NTR) for errors of weak-trip velocity estimates was waived. The normal requirement of standard errors of velocity less than 1 m/s for a true spectrum width of 4 m/s and a signal-to-noise ratio larger than 8 dB was changed to a maximum allowable standard error of 2 m/s. Nonetheless, it is apparent that the SZ-2 algorithm produces estimates with errors much larger than that (e.g., see Fig. 7).

A closer look at the weak trip number for the 06/20/07 case reveals that most of the noisy velocities come from the weak trip. Therefore, any censoring that should occur would be given by the power-ratio recovery-region censoring rules. Originally, the thresholds for this type of censoring were based on plots of errors of weak-trip velocity as a function of the strong-to-weak trip power ratio and the strong-trip spectrum width, with the weak-trip spectrum width as a parameter (Ellis et al. 2005). However, those plots only considered the 1-2 overlay case. A more thorough analysis is presented next.

Fig. 8 shows the standard error of weak-trip velocity estimates on the strong-to-weak power ratio vs. strong-trip spectrum width plane, with the weak-trip spectrum width as a parameter (ranging from 1 to 8 m/s) for the 1-2, 1-3, and 1-4 overlay situations, respectively. These statistics were computed for the nominal transmitter frequency of 2800 MHz, a short PRT of 780 μs, and large SNR. Comparing these figures, it is evident that the different overlay situations exhibit different power-ratio recovery regions. Furthermore, for wide weak-trip spectrum widths, acceptable recovery of weak-trip velocities is not possible (i.e., errors of weak-trip velocity are unacceptably large).

Closer examination of these plots indicates that the current recovery region thresholds are not aggressive enough. We propose expanding the set of thresholds to accommodate all expected overlay cases and to modify the rules so that three weak-trip spectrum width regions are considered: narrow, medium, and wide. For the narrow and medium weak-trip spectrum widths, thresholds should be different, and for wide weak-trip spectrum widths, immediate censoring should be applied. Fig. 9 depicts the effects of the different censoring approach on the 06/20/07 case. Note that the current censoring scheme is not aggressive enough, producing a large number of noisy velocities. The proposed censoring scheme mitigates this problem but not completely. Evidently, we could apply an even stronger censoring scheme, but there is a trade-off between preserving data quality by censoring unreliable estimates and recovering as much as we can by not censoring valid data.

A comprehensive analysis is needed before establishing a permanent set of censoring thresholds. Ideally, we should examine a variety of cases collected from several operational radars. However, this type of analysis requires level-I phase-coded data which is not available. Whereas the determination of optimum censoring thresholds would take significant time, the SZ-2 code will be modified right away to include the upgraded rules for recovery region censoring. Having the additional functionality in place, the thresholds will be set so that the algorithm behaves exactly the same as in the current implementation. The thresholds will be updated in later releases after a thorough censoring threshold evaluation with little impact to the system. This would minimize the occurrence of noisy velocities when using SZ-2 at the expense of increasing the number of gates with purple haze.

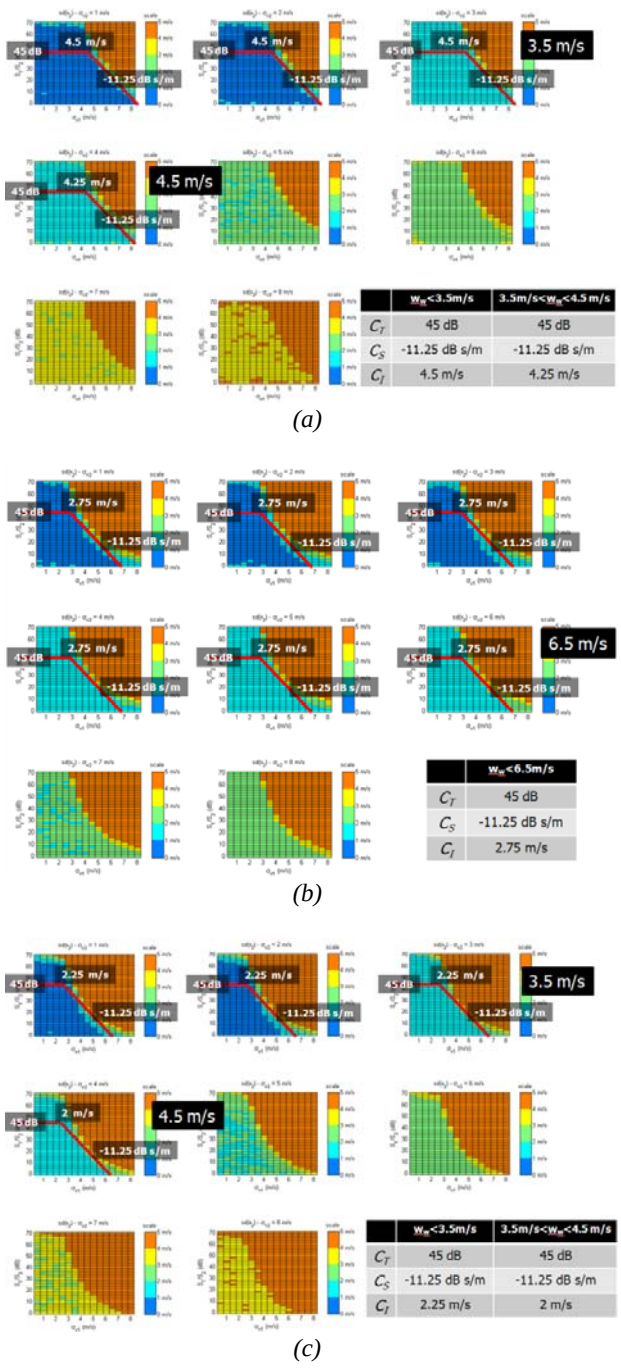

Fig. 8. Standard deviation of weak-trip velocities for the SZ-2 algorithm as a function of the power ratio (S_1/S_2) and the strong-trip spectrum width (σ_{v1}) for the 1-2 (a), 1-3 (b), 1-4 (c) overlay cases, high SNR, and weak-trip spectrum widths (σ_{v2}) between 1 and 8 m/s.

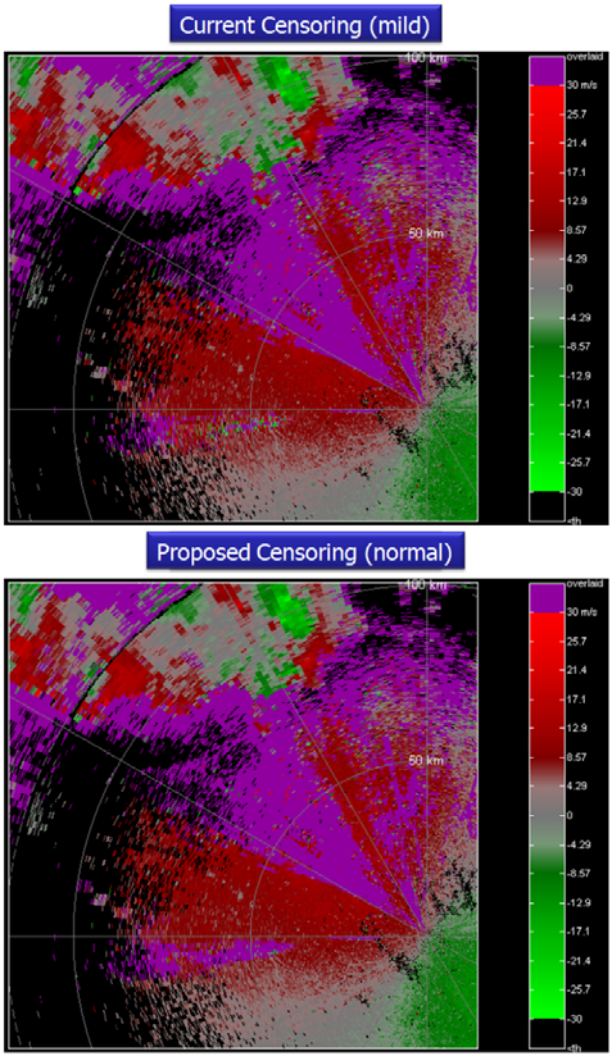

Fig. 9. Doppler velocity fields for the June 20, 2007 case using current and proposed recovery region censoring threshold.

5. Conclusions

This work demonstrated the performance of the SZ-2 algorithm as currently implemented on the NEXRAD network. Despite a few limitations and issues that arouse after the initial implementation, comparisons with previous "legacy" algorithms demonstrate the ability of the SZ-2 algorithm to effectively mitigate range and velocity ambiguities on the US network of weather surveillance radars.

Acknowledgment

This conference paper was prepared by Sebastián Torres with funding provided by NOAA/Office of Oceanic and Atmospheric Research under NOAA-University of Oklahoma Cooperative Agreement #NA17RJ1227, U.S. Department of Commerce. The statements, findings, conclusions, and recommendations are those of the author(s) and do not necessarily reflect the views of NOAA or the U.S. Department of Commerce.

References

Ellis, S. M., M. Dixon, G. Meymaris, S. Torres, and J. Hubbert, 2005: Radar range and velocity ambiguity mitigation: Censoring methods for the SZ-1 and SZ-2 phase coding algorithms. Preprints, *21st International Conf. on Interactive Information and Processing Systems (IIPS) for Meteorology, Oceanography, and Hydrology*, San Diego, CA, Amer. Meteor. Soc., Paper 19.3.

Laird, B. G., 1981: On ambiguity resolution by random phase processing. Preprints, *20th Conf. on Radar Meteorology*, Boston, MA, Amer. Meteor. Soc., 327–331.

Sachidananda, M., D. S. Zrnić, R. J. Doviak, and S. M. Torres, 1998: Signal design and processing techniques for WSR-88D ambiguity resolution, Part 2. NOAA/NSSL Report.

Sachidananda, M. and D. S. Zrnić, 1999: Systematic phase codes for resolving range overlaid signals in Doppler weather radar. *J. Amos. Oceanic Technol.*, **16**, 1351-1363.

Saffle, R. E., M. J. Istok, and G. Cate, 2007: NEXRAD product improvement – update 2007. Preprints, *23rd International Conference on Interactive Information and Processing Systems (IIPS) for Meteorology, Oceanography, and Hydrology*, San Antonio, TX, Amer. Meteor. Soc., Paper 5B.1.

Saxion, D. S., R. D. Rhoton, R. L. Ice, D. A. Warde, O. E. Boydstun, S. Torres, G. Meymaris, and W. D. Zittel, 2007: New science for the WSR-88D: implementing a major mode on the SIGMET RVP8. Preprints, *23rd International Conference on Interactive Information and Processing Systems (IIPS) for Meteorology, Oceanography, and Hydrology*, San Antonio, TX, Amer. Meteor. Soc., Paper P2.9.

Torres, S., 2005: Range and velocity ambiguity mitigation on the WSR-88D: Performance of the SZ-2 phase coding algorithm. Preprints, *21st International Conference on Interactive Information and Processing Systems (IIPS) for Meteorology, Oceanography, and Hydrology,* San Diego, CA, Amer. Meteor. Soc., Paper 19.2.

Appendix D. Ground Clutter Recognition using Polarimetric Spectral Parameters

D.1. Introduction

Ground clutter complicates interpretation of spectral moments and polarimetric variables; hence it is desirable to filter it out. Several approaches have been explored for such filtering on single-polarization radars: prerecording a power clutter map and then subtracting it from observed data (e.g., Steiner and Smith, 2002; Yo-Han Cho et al., 2006), applying Doppler filters (Siggia and Passarelli, 2004; Ice et al., 2004; Kessinger et al., 2003; Berenguer et al., 2006), and a combination of both as has been implemented on the WSR-88D network in the USA, i.e., a Doppler filter is applied at range gates selected from a prerecorded clutter map. Problems with the latest approach are changes in clutter returns over time due to changes of ambient parameters, formation of clutter returns via anomalous propagation of radio waves, and the creation of new clutter areas in rain. This necessitates an adaptive approach for clutter filtering. The Gaussian model adaptive processing, GMAP, for clutter filtering (Siggia and Passarelli 2004) is a very successful application of such approach. On the WSR-88D network, GMAP is applied according to a fixed (static) clutter map. Herein we describe a procedure that can be used to adaptively generate a dynamic "clutter map".

The US National Weather Service is planning to upgrade the WSR-88D radar network with dual polarization (Saffle et al., 2007). Thus significant new capability including recognition of echoes from ground clutter will become available. Thus far recognition of

clutter was based on the values of polarimetric variables (e.g., Zrnić et al., 2001) and their texture, i.e., spatial variations of polarimetric parameters (Dixon et al., 2006, Gourley et al. 2007). These approaches have high probability of clutter recognition in areas with no rain. The presence of rain decreases correct recognition. Herein we do not consider the textures of polarimetric parameters and focus on clutter recognition in a single range gate. We show that the few Doppler spectral lines around zero velocity can be used to recognize clutter in cases with and without rain, i.e., we describe an approach which allows adaptive clutter filtering at a single range location.

Ground clutter cancellation is most needed at low elevations wherein clutter is strongest. Currently, volume coverage pattern #11, VCP11, is most frequently used on the WSR-88D. Two lowest elevations of VCP11 are at 0.5^o and 1.45^o. At each there is a surveillance sweep with the samples M = 17 and the pulse repetition frequency 320 Hz (PRI=1) followed by the Doppler sweep with PRF of about 1000 Hz and the number of samples between 48 and 51 depending on the exact PRF. Ground clutter recognition and cancellation must be applied to both sweeps. We present our results first on the Doppler scan and then compare with those obtained on the surveillance scan.

D.2. The algorithm

We use three polarimetric variables: differential reflectivity, Z_{DR}, the differential phase φ_{dp} , and copolar correlation coefficient ρ_{hv}, the definitions of which can be found in Doviak and Zrnić, 2006. Fig. 1 illustrates differences in polarimetric parameters of ground clutter and weather. The data were obtained with the polarimetric prototype of the WSR-88D, i.e., KOUN, situated in Norman, OK. The clutter data were collected in clear

air and weather ones were collected at distances beyond 50 km to avoid possible clutter contamination. Visual inspection of the weather data shows that echoes due to anomalous propagation were absent. It is seen in Fig.1 that all variables form clutter have significantly wider distributions than the variables from weather. Thus polarimetric variables from clutter are frequently outside intervals occupied by values from weather. Despite obvious difference in distributions in weather and clutter there are large areas where there is overlap so that no one of the parameters can recognize clutter with high probability at a single range location. Averaging over few range locations makes such recognition more satisfactory (e.g., Zrnić et al., 2001). No spatial averaging is considered herein.

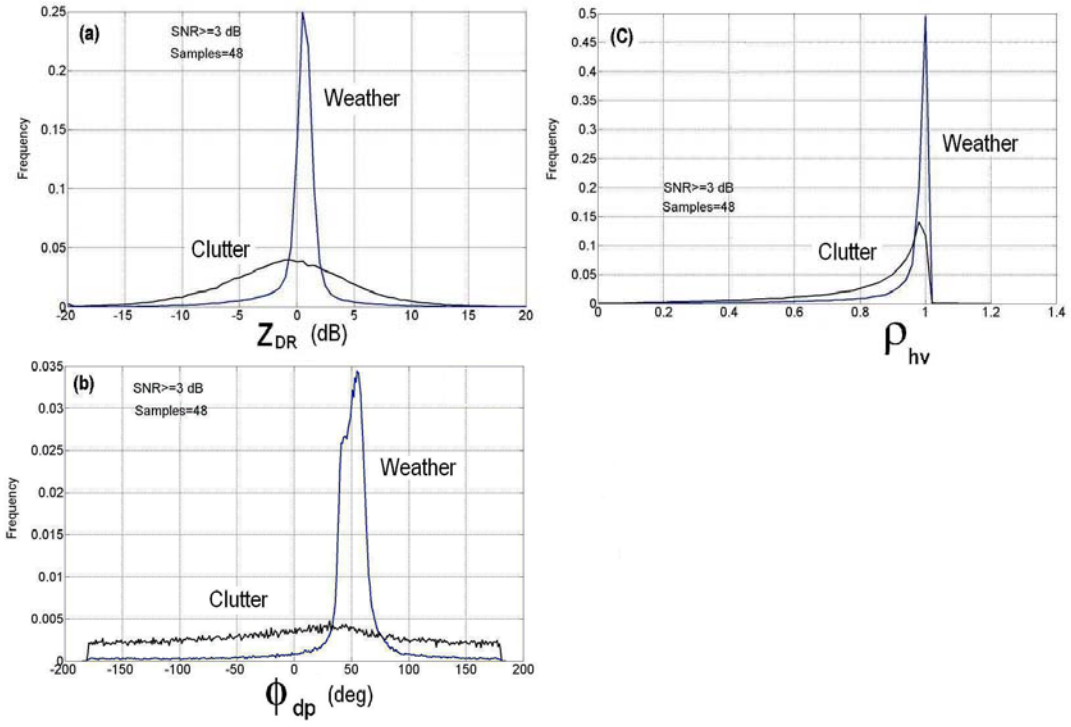

Fig. D.1. Distributions of polarimetric parameters for weather and clutter. Weather data were recorded on June 26, 2007 at 1217 UT and clutter on December 19, 2007 at 0136 UT. Elevation is 0.5°. SNR >=3 dB, *M*=48. WSR-88D KOUN.

It is known that the Doppler spectra of clutter returns are narrow (e.g., Beglesley, 2001), i.e., the main spectral lobe occupies few central lines. In contrast to clutter, weather spectra are usually broader with nonzero mean Doppler velocities. So to recognize clutter, the polarimetric information in the central Doppler spectral lines can be analyzed. That is, polarimetric spectral densities are introduced and examined.

We studied the polarimetric properties of three central spectral lines of the surveillance and Doppler scans. In the Doppler mode of the WSR-88D, these three lines occupy velocity interval of 2.4 m s^{-1} with the center at zero velocity (velocity unambiguous interval is ±27.6 m s^{-1} and the number of spectral lines is M= 48). Vast majority of clutter's spectrum widths are in this interval so we expect that the three lines might represent clutter spectra well. In Fig. D.2a, spectra at H- and V-polarizations are shown; the data were collected in snowfall on December 12th, 2006. In Fig. D.2b are 3-line spectra at both polarizations centered at zero velocity. In Fig. D.2c are the residual spectra obtained by subtracting the 3-line spectra from the full spectra in Fig. D.2a. Four polarimetric variables are calculated using the 3-line spectra: differential reflectivity ($\widetilde{Z}_{DR}$), differential phase shift ($\widetilde{\varphi}_{dp}$), copolar correlation coefficient ($\widetilde{\rho}_{hv}$), and the power ($\widetilde{P}_h$). Radar parameters from the full spectrum are denoted as Z_{DR}, φ_{dp}, ρ_{hv}, and P_h. The Von Hann spectral window has been applied to the time series data.

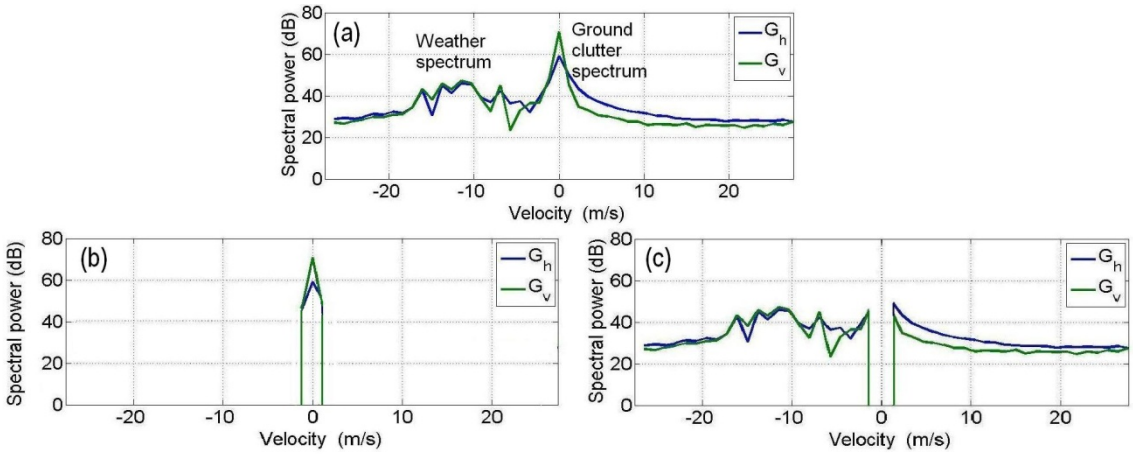

Fig. D.2. (a) Spectra at H (blue color) and V (green color) polarizations recorded in snowfall on December 12, 2006, 0028:27; azimuth is 133°, elevation is 2.5°, PRF=1000 Hz, *M*=48. The spectral powers are in the internal processor units. (b): 3-line spectra obtained from the spectra in Fig. D.2(a). (c): residual spectra obtained by removing the 3-line spectra shown in Fig. D.2(b) from the full spectra in Fig. D.2(a).

To recognize ground clutter, the following algorithm has been applied. At a given range location, the measured polarimetric moments of the 3-line spectra are compared with predetermined thresholds $\widetilde{P}_{h0}$, $\widetilde{Z}_{DR0}$, $\widetilde{\rho}_{hv0}$, and $\widetilde{\varphi}_{dp0}$. The echo is considered to be ground clutter if

$$\widetilde{Z}_{DR} > \widetilde{Z}_{DR2}, \text{ or } \widetilde{Z}_{DR} < \widetilde{Z}_{DR1} \text{ or} \tag{1}$$

$$\widetilde{\rho}_{hv} \le \widetilde{\rho}_{hv0}, \text{ or} \tag{2}$$

$$|\widetilde{\varphi}_{dp} - \overline{\varphi}_{dp}| \ge \widetilde{\varphi}_{dp0}, \tag{3}$$

provided

$$S\widetilde{N}R_h \ge S\widetilde{N}R_{h0} \ . \tag{4}$$

Inequality (4) is a SNR threshold to avoid contamination from noise. Note that it imposes a threshold to the 3-line spectrum not to the full spectrum. It means that signals with

spectral component sufficiently far from zero velocity are not included in the analysis. This is schematically shown in Fig. 3. The full weather spectrum G(v) has strong total power with its peak located away from zero velocity. The three spectrum lines G_{-1}, G_0 , and G_1 constitute $\widetilde{P}$ = G_{-1} + G_0 + G_1 power. G_0 is the spectral line at zero Doppler velocity. SNR threshold $S\widetilde{N}R$ is calculated as:

$$S\widetilde{N}R \geq \frac{\widetilde{P} - 3N/M}{3N/M}, \tag{5}$$

where N is the noise power in the channel. The mean noise power at one spectral line is N/M, so the noise power at three spectral lines is $3N/M$. SNR threshold (5) is calculated for the H- and V-channels using their mean noise powers.

The polarimetric parameters for the 3-line spectrum are calculated as follows. Differential reflectivity is

$$\widetilde{Z}_{DR} = \frac{\widetilde{P}_h - 3N_h/M}{\widetilde{P}_v - 3N_v/M}. \tag{6}$$

The differential phase and copolar correlation coefficient are calculated in frequency domain using the complex amplitudes g_{-1}, g_0, and g_1 of the three spectral lines in the polarimetric channels:

$$\widetilde{\varphi}_{dp} = \arg(g_{-1(h)}g^*_{-1(v)} + g_{0(h)}g^*_{0(v)} + g_{1(h)}g^*_{1(v)}). \tag{7}$$

$$\widetilde{\rho}_{hv} = \frac{|\, g_{-1(h)}g^*_{-1(v)} + g_{0(h)}g^*_{0(v)} + g_{1(h)}g^*_{1(v)} \,|}{[(\widetilde{P}_h - 3N_h/M)(\widetilde{P}_v - 3N_v/M)]^{1/2}}. \tag{8}$$

$$\widetilde{P}_h = g_{-1(h)}g^*_{-1(h)} + g_{0(h)}g^*_{0(h)} + g_{1(h)}g^*_{1(h)} = G_{-1(h)} + G_{0(h)} + G_{1(h)}, \quad (9a)$$

$$\widetilde{P}_v = g_{-1(v)}g^*_{-1(v)} + g_{0(v)}g^*_{0(v)} + g_{1(v)}g^*_{1(v)} = G_{-1(v)} + G_{0(v)} + G_{1(v)}, \quad (9b)$$

where the asterisk denotes complex conjugate.

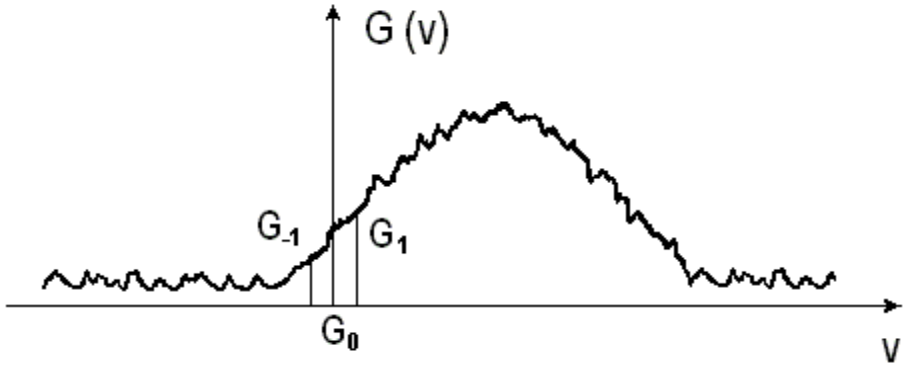

Fig. D.3. Sketch of a weather velocity spectrum with zero velocity line G_0 and two nearest lines G_{-1} and G_1.

Inequality (1) sets threshold on differential reflectivity. Observations on the WSR-88D KOUN show that hydrometeors' Z_{DR} lay in the interval -2 to 5 dB (most frequently, -1 to 4 dB) so that inequality (1) is based on these observations. In (1) we use $\widetilde{Z}_{DR1}$=-2 dB, $\widetilde{Z}_{DR2}$=5 dB. Negative Z_{DR} are observed sometimes at the tops of severe thunderstorms where strong electric fields align cloud crystals vertically. This effect can be neglected in ground clutter recognition because we consider lowest elevation angles. Negative Z_{DR} can also be caused by strong differential attenuation. To mitigate this effect, a correction of differential reflectivity should be applied using measured specific differential phase. Presently the algorithm makes no such correction of Z_{DR}. Z_{DR} of 5 dB and higher can be

measured in the presence of insects and birds so for weather echoes 5 dB was chosen for upper Z_{DR} threshold.

$\widetilde{\rho}_{hv0}$ threshold (2) for weather was set to 0.8. Weather signals have correlation coefficient larger than this threshold. However in the bright band, ρ_{hv} can occasionally drop to 0.8 and this can affect the algorithm when the melting layer is very close to the ground. Data analysis might be needed to resolve such situations.

Inequality (3) sets a threshold for the differential phase. Note that in Fig. 1(b) the differential phases are plotted with the system phase that should be subtracted in differential phase measurements. Inequality (3) expresses a limitation on phase fluctuations so the threshold $\widetilde{\varphi}_{dp0}$ can be obtained from the standard deviation, SD, of differential phases (Melnikov and Zrnić, 2007):

$$SD(\varphi_{dp}) = \frac{180}{\pi(2M)^{1/2}\rho_{hv}}\left(\frac{SNR_h + SNR_v + 1}{SNR_h\, SNR_v} + \frac{1-\rho_{hv}^2}{\pi^{1/2}\sigma_{vn}}\right)^{1/2} \text{(deg)}, \qquad (10)$$

where σ_{vn} is the normalized spectrum width, i.e., a ratio of the spectrum width and unambiguous Doppler velocity: $\sigma_{vn} = \sigma_v/v_u$. Using threshold $\widetilde{\rho}_{hv0}$ = 0.8, $\widetilde{SNR}_{h0}$ = 3 dB, M = 48, σ_v = 1 m s^{-1}, we get SD = 19^o. The distribution of $\varphi_{dp} - \overline{\varphi}_{dp}$ is nearly symmetrical so we use $\widetilde{\varphi}_{dp0} \approx$ SD = 20^o. Weather ρ_{hv} is usually greater than 0.95 therefore most of $|\varphi_{dp} - \overline{\varphi}_{dp}|$ will be smaller than 20^o.

For weather spectra, $\widetilde{Z}_{DR}$, $\widetilde{\rho}_{hv}$ or $\widetilde{\varphi}_{dp}$ can be of "clutter" values due to natural signal fluctuation, i.e., some weather echoes are recognized as clutter. So the algorithm should

also be characterized with the false alarm rate for true weather echoes. Probability of such occurrences increases with the decrease of $\widetilde{SNR}$. It is shown in the Appendix that if the weather power exceeds the clutter power by 30 dB or more, the clutter contribution to the polarimetric moments can be neglected, the echo can be considered as "weather like" and its location can be excluded from clutter recognition. This can save some processing time. For now, the algorithm is applied "off line" and does not include this option.

All the algorithm's thresholds are summarized in Table D.1 and the radar parameters are in Table D.2.

$\widetilde{SNR}_{h0}$, dB	$\widetilde{Z}_{DR1}$ / $\widetilde{Z}_{DR2}$, dB	$\widetilde{\rho}_{hv0}$	$\widetilde{\varphi}_{dp0}$, deg	ΔS, dB
3	-2 / 5	0.8	20	-30

Table D.1. Threshold parameters used in clutter recognition

Elevation, deg	Antenna rate, deg/s	Number of samples	Azimuthal resolution, deg	Pulse repetition frequency, Hz
0.5	20	48	1	1013

Table D.2. Radar parameters of data collection

D.3. Recognition results

a) Ground clutter and insects

To justify the thresholds used in clutter recognition (Table D.1), data were collected in clear air. Clear air returns are different for warm and cold seasons as demonstrated in Fig. D.4. The right panel of the figure exhibits more echo due to insects. The insects' echoes have significant SNR at close distance so they pass criterion (4) and are analyzed by the algorithm (1)-(3).

Distributions of the polarimetric parameters for the cold and warm seasons are shown in Fig. D.5. It is seen that insects make the distributions wider in the warm season. Clutter recognition rates based on a single parameter and rules (1)-(3) are shown in Table D.3. One can see that probability of clutter detection via (1)-(3) is mostly larger than 93% for both cold and warm seasons in Oklahoma. For a single polarimetric parameter, the differential phase exhibits the best recognition performance of about 83%.

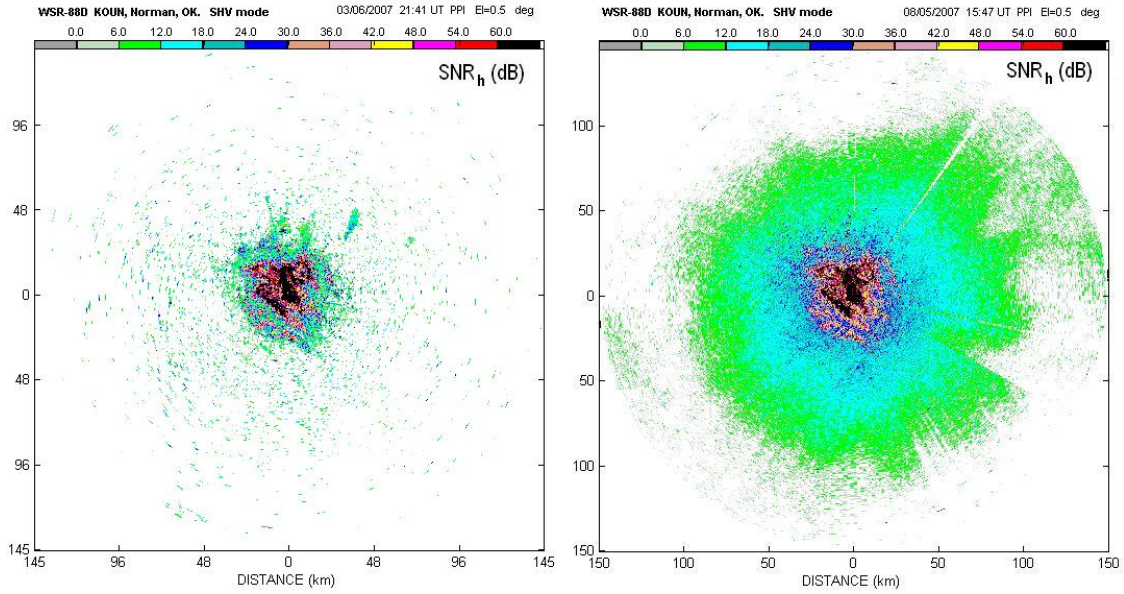

Fig. D.4. Clear air returns on 6 March, 2007 at 2141 UT (left panel) and 5 August 2007 at 1547 (right panel) UT. El=0.5^o, M = 48. WSR-88D KOUN.

Date	Z_{DR}		ρ_{hv}		φ_{dp}		Combined	
	Full spect.	3-line spect.	Full spect.	3-line spect.	Full spect	3-line spect.	Full spect	3-line spect.
16 January, 2007	0.56	0.56	0.20	0.16	0.81	0.81	0.92	0.92
6 March, 2007	0.56	0.58	0.24	0.17	0.84	0.85	0.94	0.94
5 August, 2007	0.72	0.75	0.65	0.37	0.89	0.89	0.99	0.98
21 Septem., 2007	0.48	0.57	0.54	0.24	0.77	0.82	0.92	0.91
19 Decemb., 2007	0.54	0.57	0.30	0.18	0.84	0.84	0.93	0.93
17 February, 2008	0.59	0.60	0.28	0.21	0.83	0.83	0.94	0.93

Table D.3. Frequencies of clutter recognition via algorithm (1) – (3).

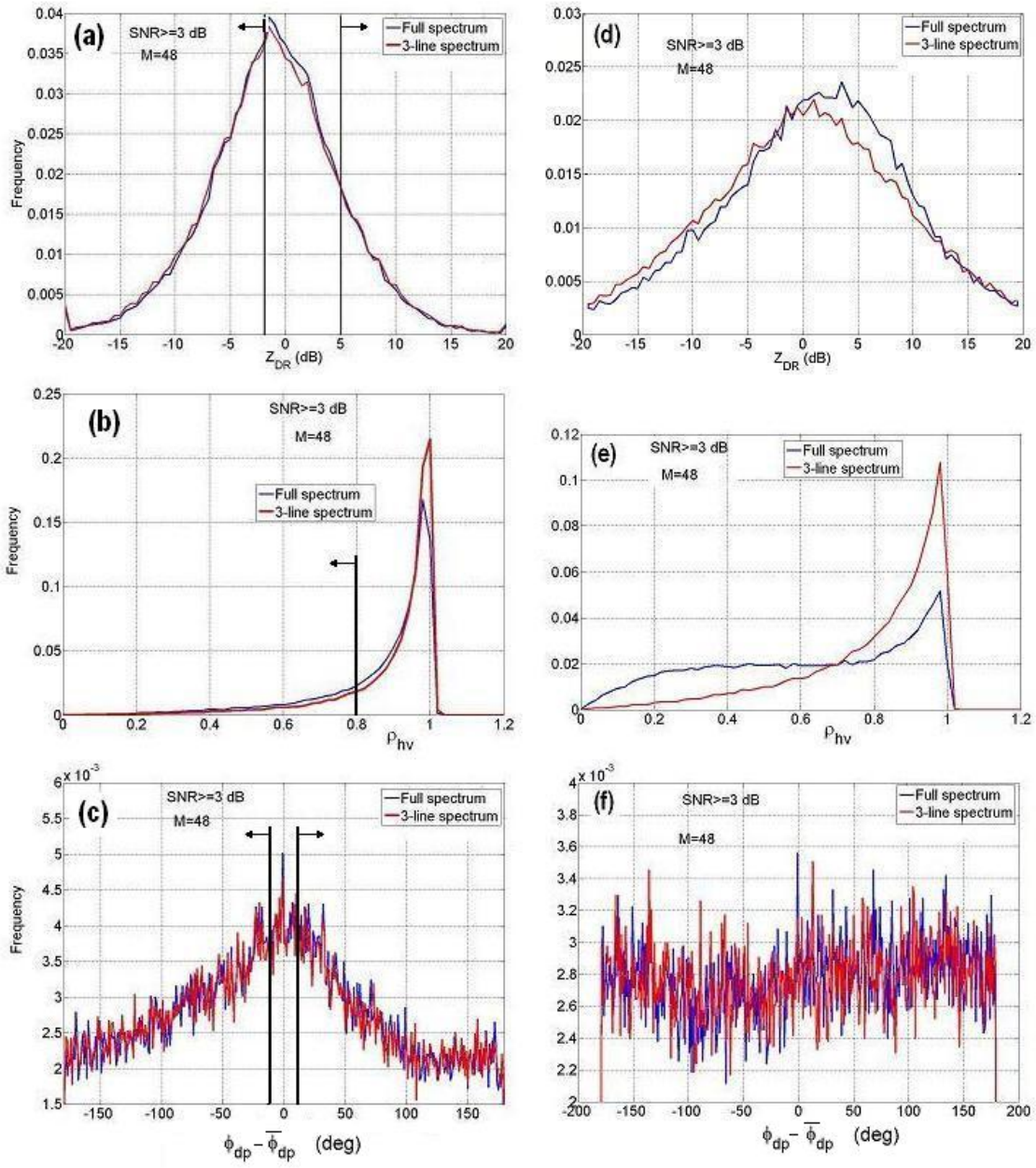

Fig. D.5. Distributions of the polarimetric parameters for clutter in the cold (a, b, c) and warm (d, e, f) seasons in central Oklahoma. The black vertical lines in (a, b, c) show the thresholds imposed by the algorithm (1)-(3).

b) Weather echoes

Algorithm (1)-(3) applied to weather echoes results in nonzero probability that actual weather echoes are classified as ground clutter. This probability is a false alarm rate of the algorithm and should be as little as possible. To obtain the false alarm rate, radar data beyond 50 km have been analyzed. At KOUN site, ground clutter is observed within 47 km so 50 km was considered as distance beyond which echoes are from precipitation. In precipitation, relative humidity is close to 100% so favorable conditions for anomalous propagation, AP, of electromagnetic waves can be present. To avoid obvious AP echoes, we have inspected echoes visually. This is not perfect because some AP echoes can be inside precipitation and thus can be masked. Fig. D.6 presents an example of a superposition of weather echoes and ground clutter. One can see that the φ_{dp} field has usual radial patterns and to apply rule (3), the differential phase has to be obtained. The phase was calculated by averaging the measured differential phase over 2 km in range (8 range consecutive samples). No attenuation correction has been made for Z_{DR} because attenuation was insignificant. Distributions of the polarimetric parameters are shown in Fig. D.7 and the false alarm rates for the case are presented in Table D.4.

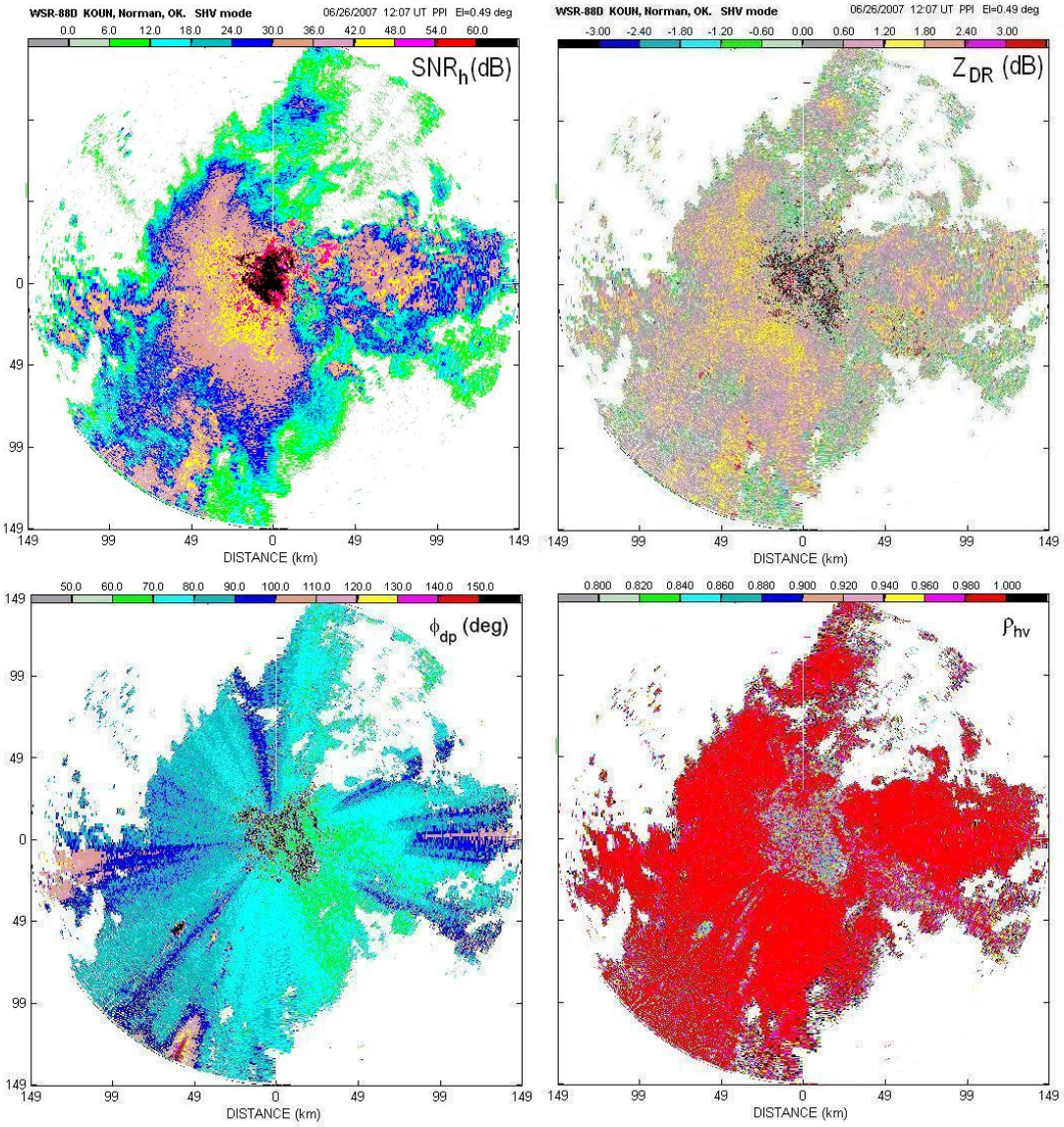

Fig. D.6. Fields of SNRh, Z_{DR}, φ_{dp} and ρ_{hv} on June 26, 2007 at 1207. El=0.5°.

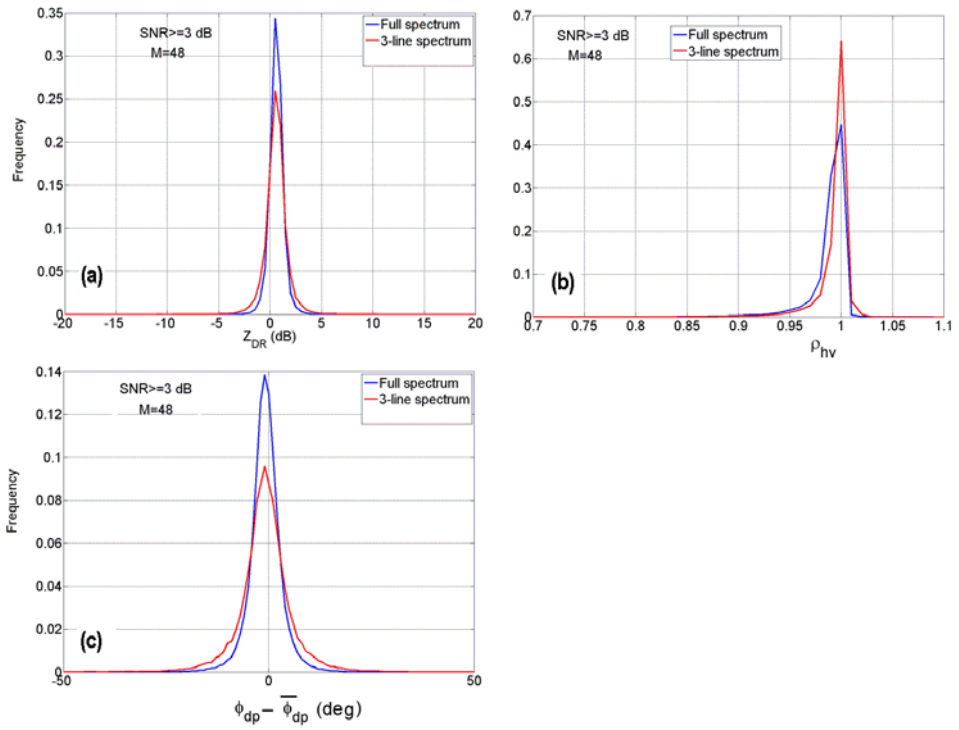

Fig. D.7. Distributions of Z_{DR}, ρ_{hv} and φ_{dp} for precipitation shown in Fig. D.6.

Date	Z_{DR}		ρ_{hv}		φ_{dp}		Combined	
	Full spect.	3-line spect.	Full spect.	3-line spect.	Full spect.	3-line spect.	Full spect	3-line spect.
12 January, 2007	0.001	0.02	0.001	0.002	0.001	0.01	0.003	0.03
	0.001	0.01	0.001	0.001	0.001	0.01	0.002	0.02
	0.002	0.02	0.002	0.003	0.001	0.01	0.004	0.02
	0.001	0.02	0.001	0.002	0.001	0.01	0.002	0.03
	0.001	0.01	0.001	0.001	0.001	0.01	0.002	0.02
	0.001	0.01	0.001	0.001	0.001	0.01	0.002	0.02
14 January, 2007	0.002	0.01	0.003	0.002	0.004	0.01	0.01	0.02
	0.004	0.02	0.004	0.004	0.006	0.02	0.01	0.04
	0.003	0.02	0.003	0.003	0.005	0.02	0.01	0.04
	0.002	0.01	0.002	0.001	0.005	0.02	0.01	0.02
15 Febr., 2007	0.030	0.05	0.020	0.003	0.10	0.14	0.08	0.11
26 June, 2007	0.003	0.02	0.004	0.007	0.01	0.05	0.01	0.04
19 August, 2007	0.008	0.03	0.009	0.012	0.01	0.05	0.02	0.07
22 Dec., 2007	0.004	0.01	0.004	0.001	0.003	0.02	0.01	0.03
	0.004	0.02	0.003	0.002	0.005	0.03	0.01	0.04

Table D.4. False alarm rates of algorithm (1)-(3) for precipitation.

It is follows from Table D.4 that the false alarm rate is usually lower than 5%. On 15th February, 2007 the rate was 11%. Data analysis showed that this was a snowfall with large areas of SNR lower than 10 dB and a vast majority of false recognitions occurs in such areas. Table 4 shows that the majority of false alarm rates is less than 5% even in winter precipitation.

c) Anomalous propagation echoes

Anomalous propagation, AP, of electromagnetic waves results in clutter echoes at locations where there was no echo at normal refraction conditions. Examples of SNR and Z_{DR} fields in the presence of AP echoes are shown in Fig. D.8. The left panels contains AP in the absence of precipitation whereas AP in the right panels occurred behind the band of precipitation that moved SE. Polarimetric parameters of AP echoes have been analyzed inside areas indicated in Fig. D.8 with the black sectors. To get rid of echoes from insects, SNR threshold of 20 dB was applied, i.e., threshold $\widetilde{SNR}_{h0}$ in (4) was changed from 3 to 20 dB.

Distributions of the polarimetric variables from AP echoes are in Fig. D.9 and probabilities of detection are in Table D.5. It is seen from the table that the probability of detection (POD) of the AP echoes are about 90% which is slightly less than the POD of regular close by clutter shown in Table D.3.

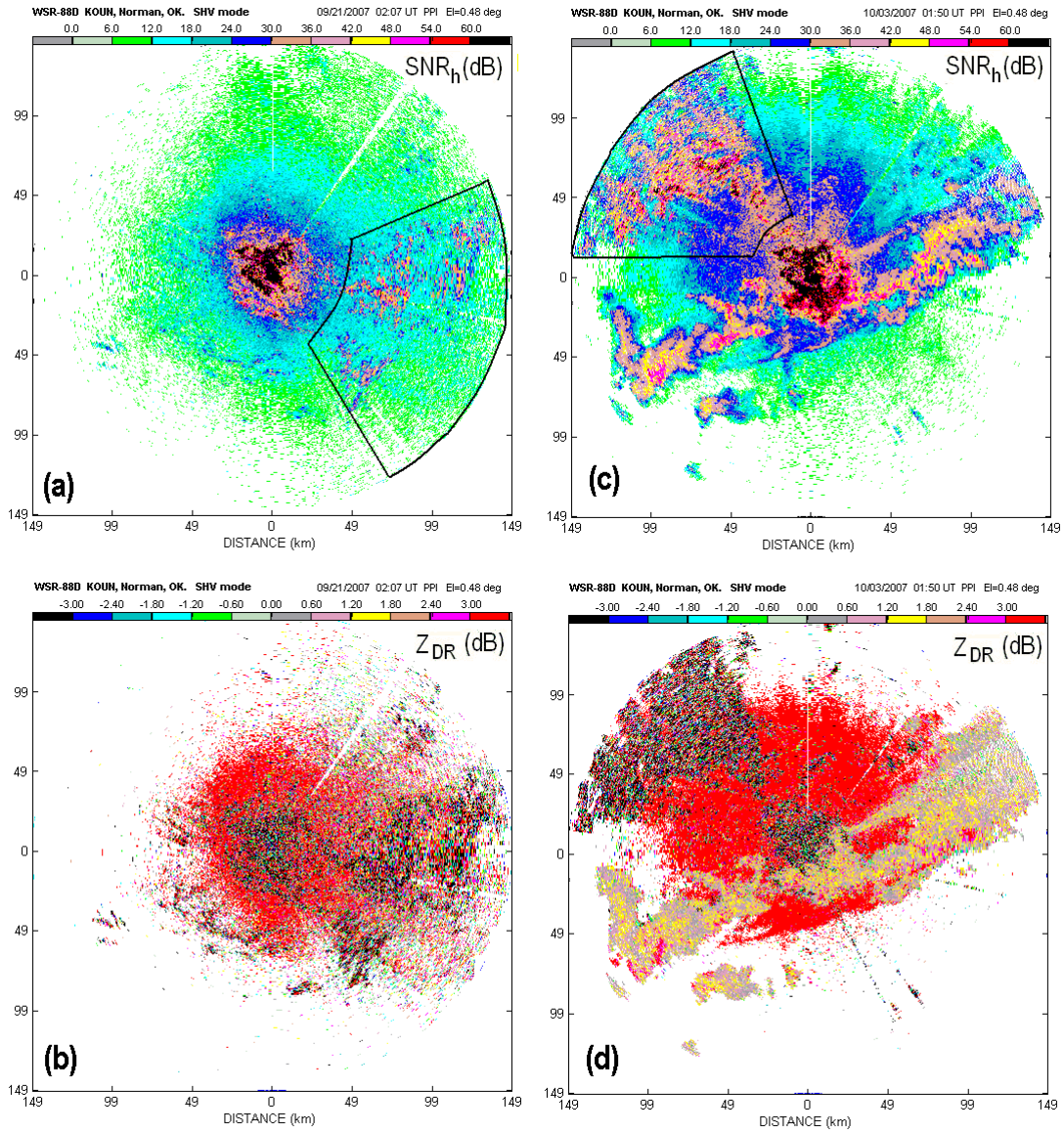

Fig. D.8. AP echoes on 21 September, 2007 (a, b) and 3 October, 2007 (c, d). The black sectors are areas wherein polarimetric parameters of AP echoes have been analyzed.

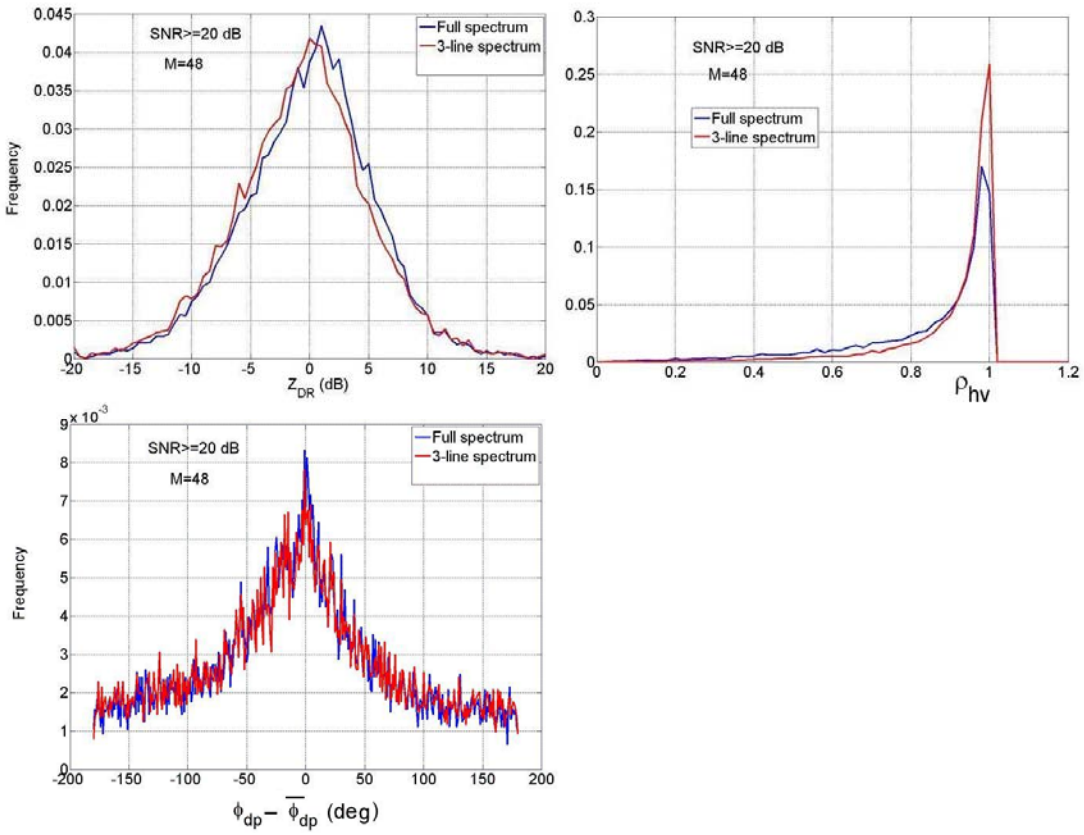

Fig. D.9. Distributions of Z_{DR}, ρ_{hv}, and φ_{dp} for AP echoes on 3 October, 2007.

Date	Z_{DR}		ρ_{hv}		φ_{dp}		Combined	
	Full spect.	3-line spect.	Full spect.	3-line spect.	Full spect	3-line spect.	Full spect	3-line spect.
21 Sept., 2007	0.53	0.56	0.16	0.09	0.81	0.81	0.91	0.91
3 October, 2007	0.53	0.56	0.26	0.13	0.77	0.78	0.89	0.89
	0.53	0.57	0.28	0.14	0.77	0.78	0.89	0.89

Table D.5. Frequencies of AP echoes recognition via algorithm (1) – (3).

d) Mixtures of ground clutter and weather echoes

Clutter recognition algorithm is meant to work in situations with superimposed precipitation and clutter. It is important to obtain the relative powers of weather and clutter at which clutter recognition is of a given probability. We obtained these probability combining simulation and radar data. Weather signals can be simulated easily

using algorithm of Jenkins and Watts, 1964. Simulation data correspond to statistics of dual-polarization signals very well down to SNR = 2 dB (e.g., Melnikov and Zrnić 2007). Simulation of clutter is more complicated because its signal can consist of coherent and non coherent components (Billingsley 2001). The coherent component is caused by stationary objects (ground itself, buildings, and big tree trunks). The non coherent component is produced by objects like leaves, grass, tree branches responding to the wind. Instead of simulating clutter with the two components, we used real clutter signals recorded in clear air, i.e., I and Q components. A mixture of weather and clutter signal has been obtained by superposing simulated I-Q components of weather with I-Q components of clutter from the KOUN site. By appropriately scaling the relative powers of weather and clutter signal we can span a range of Clutter-to-Signal Ratios, CSR. In the analysis, we could use real weather signals recorder outside regions contaminated by clutter but such signals are less versatile for the analysis. Weather signals can be simulated precisely for any polarimetric parameters and this allows more freedom in the analysis of the mix signals.

On the KOUN, weather echoes have ρ_{hv} greater than 0.95 and the coefficient is often higher than 0.99. Fig. 10 depicts the frequency of ground clutter recognition in the mixtures with "weather" ρ_{hv}=0.95 and 0.99 for different mean Doppler velocities and spectrum widths as a function of CSR. It is seen from the figure that for ρ_{hv}=0.99 the clutter is recognized in the mixture with POD larger than 90% at CSR greater than 4 dB even if weather echo has zero Doppler velocity. For ρ_{hv}=0.95, the recognition rate is higher.

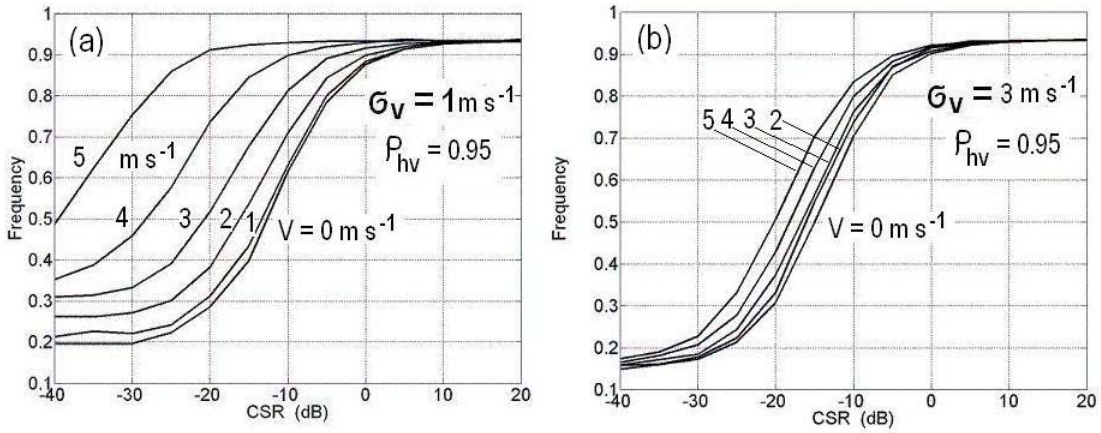

Fig. D.10. Frequency of clutter recognition for a mixture of clutter and weather as a function of CSR for $\rho_{hv} = 0.95$.

In Fig. D.11 clutter recognition areas are indicated with the red dots for the situation shown in Fig. D.6. The weather echo is presented with blue color. It is seen that the clutter region follows closely to clutter map recorded in clear air. There are some radials with excessive number of clutter dots in weather areas, e.g., radials at azimuths 200^o to 220^o. Analysis of these echoes uncovered that such dots aroused from contamination by the second trip echoes. Therefore the algorithm (1)-(3) should be applied after range ambiguity resolution which will be done on dual-polarization WSR-88D.

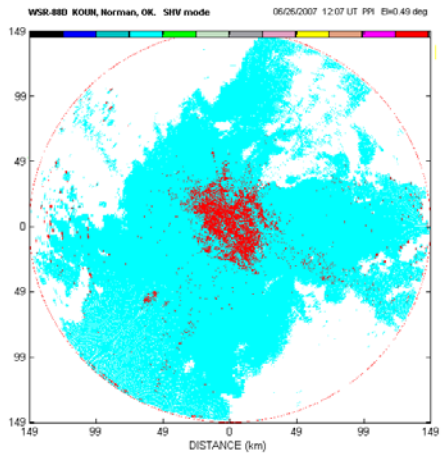

Fig. D.11. Recognized clutter (red dots) on the weather background (blue). June 26, 2007 at 1207. El=0.5^{o}

e) Surveillance scans

The lowest elevation scans of VCP11 consist of the surveillance scan (PRI=1) followed by the Doppler scan (PRI=5) at the same elevation. Both require the clutter map to activate the ground clutter filter. In the previous sections, clutter recognition was considered for the Doppler scan. That is the "instantaneous" clutter map is generated after the surveillance scan has been completed. This "instantaneous" clutter map can be applied to the subsequent surveillance scan (i.e., at the next VCP) with a delay of about 6 min assuming that there are no major changes to the clutter location. On the other hand, algorithm (1)-(3) can be applied to the surveillance scan. This possibility is described herein.

The surveillance scan is done with PRI=1, i.e, PRF of 320 Hz which has long unambiguous range but a short Niquist velocity interval ± 8.8 m s^{-1}. Weather echoes with velocities slightly larger than ±17.6 m s^{-1} will be aliased with nearly zero Doppler velocities and such weather echoes will mask the ground clutter. This makes the Doppler

scan necessary for checking the presence of aliased velocities. We consider herein a situation with no velocity aliasing. The number of samples in the surveillance mode is 17 which makes 3-line spectral interval of 2*17.6/17 = 2.1 m s^{-1}, i.e., very close to 2*55.2/48 = 2.3 m s^{-1} for the Doppler mode with 48 samples. Of course, spectra at the surveillance and Doppler modes near zero velocities are different but closeness of the 3-line central intervals makes it possible to consider the above algorithm for the surveillance scan.

Two types of data have been used in the analysis. The first type are data collected with 17 samples per 1^o azimuthal resolution with PRI #1 (321 Hz), i.e., in true surveillance scan. The second type are data collected with 48 samples and PRI#5 (1013 Hz) but processed every third pulse. Taking for processing every third pulse we closely mimic PRI#1; the pulse repetition interval becomes 1013/3 = 337.7 Hz which is sufficiently close to 321 Hz. There must be no second trip echoes in the second data type that can result from the actual higher PRF. It is satisfied for ground clutter in the absence of AP. The algorithm (1)-(3) has been applied to such data with the same thresholds as in Table D.1. Frequencies of true clutter recognition are in Table D.6 and these are very similar to ones for the Doppler mode (see Table D.3). False alarm rates for the mode are listed in Table D.8. It is seen that this rate is 9 to 14% which is noticeably larger than those for the Doppler mode, i.e., 3 to 4% in the mean (see Table D.4).

Date	Z_{DR}		ρ_{hv}		φ_{dp}		Combined	
	Full spect.	3-line spect.	Full spect.	3-line spect.	Full spect	3-line spect.	Full spect	3-line spect.
12 Decemb., 2007	0.57	0.61	0.28	0.18	0.83	0.83	0.93	0.93
5 August, 2007	0.56	0.61	0.52	0.25	0.78	0.81	0.94	0.92
16 January, 2007	0.55	0.56	0.20	0.17	0.81	0.81	0.92	0.92
6 March, 2007	0.56	0.57	0.22	0.17	0.84	0.84	0.93	0.93
5 August, 2007	0.71	0.75	0.66	0.37	0.89	0.89	0.99	0.98
21 Sept., 2007	0.49	0.58	0.52	0.23	0.77	0.82	0.92	0.91

Table D.6. Frequencies of clutter recognition via algorithm (1) – (3) in the surveillance scan

Date	Z_{DR}		ρ_{hv}		φ_{dp}		Combined	
	Full spect.	3-line spect.	Full spect.	3-line spect.	Full spect	3-line spect.	Full spect	3-line spect.
21 Sept., 2007	0.54	0.56	0.17	0.09	0.82	0.81	0.92	0.91
3 October, 2007	0.52	0.55	0.21	0.10	0.76	0.77	0.87	0.87
	0.52	0.56	0.24	0.12	0.77	0.78	0.89	0.88

Table D.7. Frequencies of AP echoes recognition via algorithm (1) – (3) in the surveillance scan

Date	Z_{DR}		ρ_{hv}		φ_{dp}		Combined	
	Full spect.	3-line spect.	Full spect.	3-line spect.	Full spect.	3-line spect.	Full spect	3-line spect.
29 June,2007	0.04	0.07	0.04	0.02	0.04	0.08	0.08	0.13
3 March, 2008	0.004	0.04	0.004	0.01	0.006	0.05	0.01	0.09
	0.01	0.04	0.004	0.01	0.006	0.05	0.01	0.09
6 March, 2008	0.01	0.04	0.005	0.002	0.02	0.06	0.03	0.09
	0.01	0.04	0.005	0.001	0.02	0.06	0.03	0.10
18 March, 2008	0.008	0.06	0.02	0.04	0.01	0.07	0.03	0.14
	0.007	0.06	0.02	0.04	0.01	0.07	0.03	0.14

Table D.8. False alarm rates of algorithm (1)-(3) for precipitation

D.4. Clutter filtering

The main purpose of this report is ground clutter recognition, i.e., the first step of clutter mitigation. The second step is ground clutter suppression which is done on the legacy system with the GMAP filter. Distributions of the clutter powers in two polarimetric channels at the KOUN site are shown in Fig. D.12. It is seen that the 3-line spectrum can

have very strong SNR exceeding 100 dB. That is clutter filtering has to be done in a wide range of CSRs of about 100 dB. There is no technique that effectively filters clutter over such a wide interval. One of the best existing techniques for a single channel radars is the GMAP filtering having clutter suppression of 30 to 50 dB (Ice et al., 2004).

In Fig. D.13 are the polarimetric fields obtained by applying GMAP filter independently in the H- and V-channels. Comparing Figs. D.6 and D.13 it is seen that the filter suppresses large areas of echoes with the Doppler velocities close to zero. It is also seen that the filter destroys Z_{DR} and ρ_{hv} fields (it affects also the differential phase that is not shown in Fig. 13). Fig. D.14 presents results of ground clutter filtering that have been obtained using algorithm (1)-(3). The filtering was done as follows. Algorithm (1)-(3) identifies range gates with clutter. At those range gates, GMAP filter was used in the H-channel alone to determine spectral coefficients belonging to clutter. These spectral coefficients were suppressed in both H- and V-channels. It is seen from Fig. D.14 that such filtering produces more realistic polarimetric fields than those in Fig. D.13.

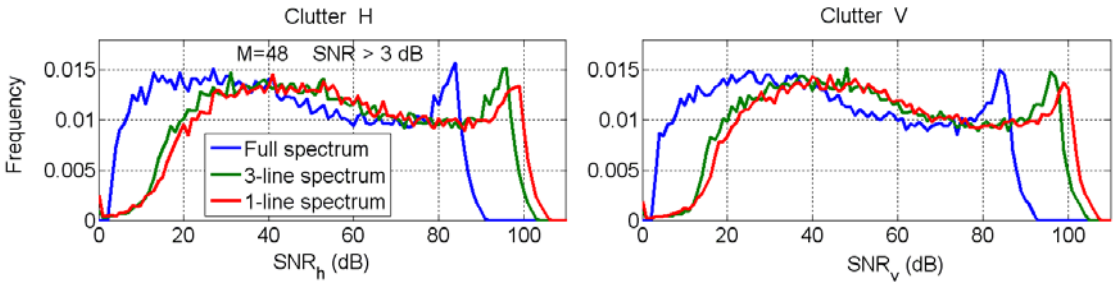

Fig. D.12. Distributions of SNR_h and SNR_v for ground clutter on 6 March, 2007. The 1-line spectrum is the central spectral line, i.e., DC component.

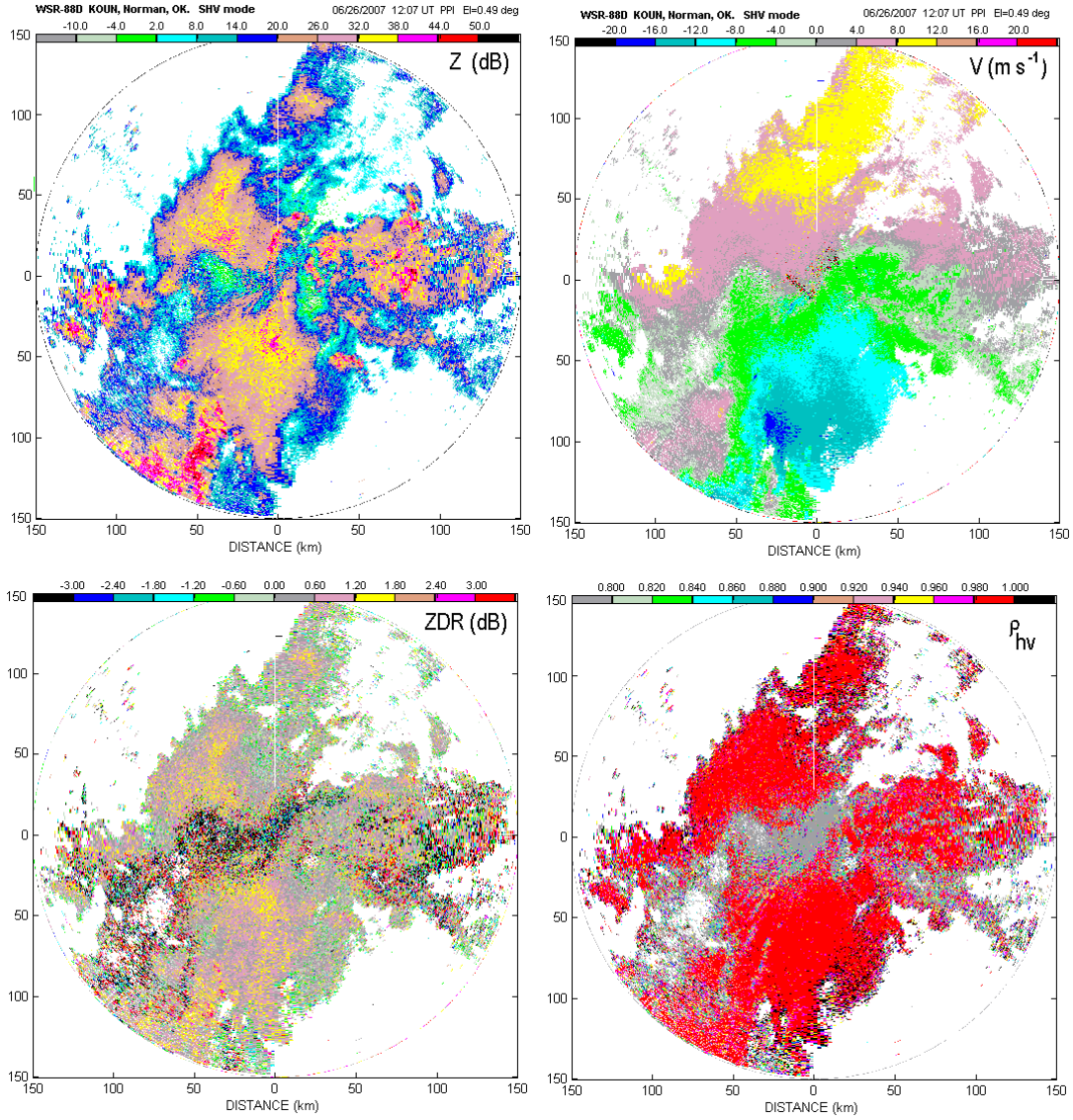

Fig. D.13. Fields of polarimetric variables and velocity obtained after applying GMAP independently to both channels. Filter is applied everywhere.

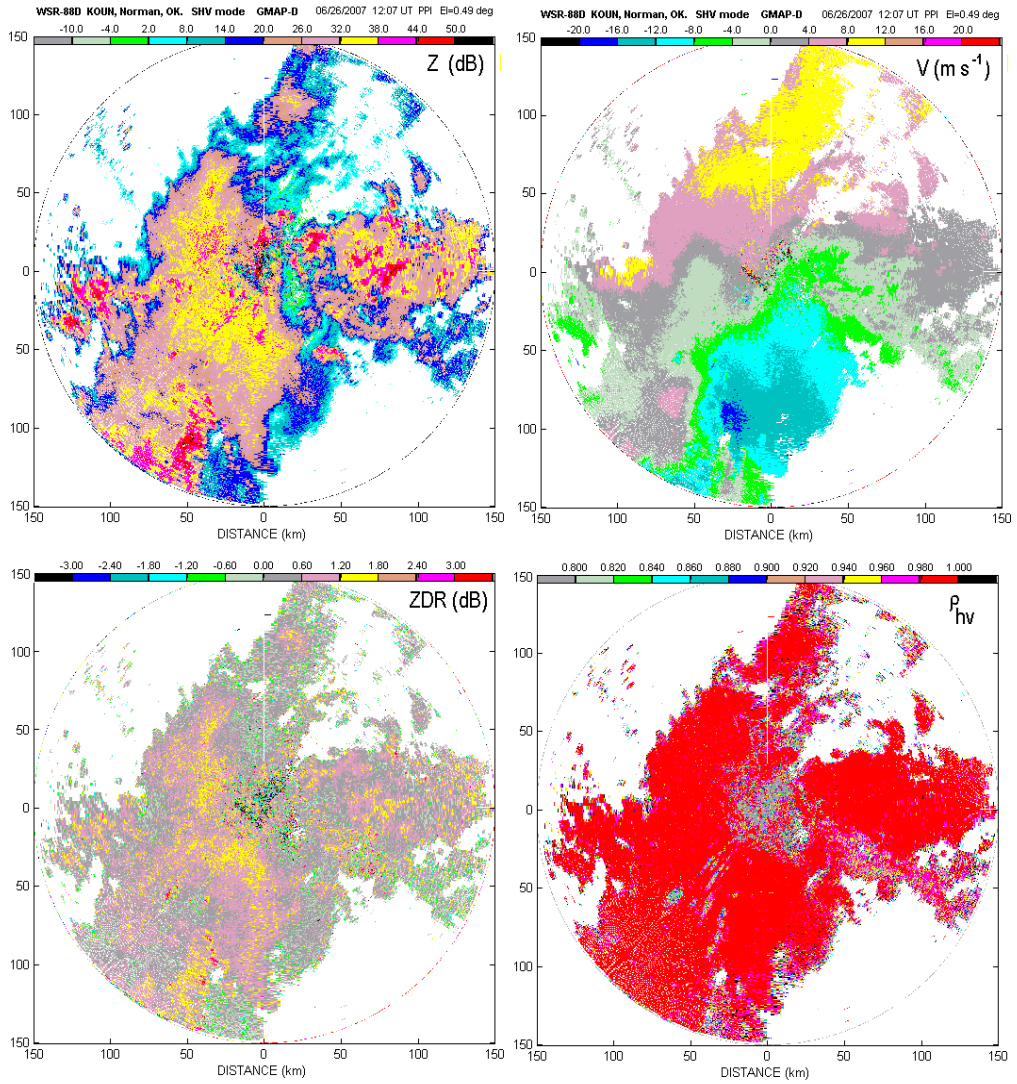

Fig. D.14. Same as in Fig. D.13 except the suppressed coefficients are determined by GMAP in the H channel. Then these coefficients are removed from both the H and the V channel at range locations where the clutter has been indentified with the algorithm (1)-(3).

D.5. Conclusions

The algorithm for clutter recognition based on polarimetric variables obtained from 3-lines of spectral densities has been applied to a relatively small number of samples 17 and 48. These are relevant to the surveillance and Doppler modes of the WSR-88D.

In the Doppler mode, the algorithm demonstrates about 93% of correct clutter recognition and a false alarm rate of 4%. Recognition of echoes due to anomalous propagation has the rate about 90%. The algorithm should be applied after removing echoes from the second and third trips. For a mixture of weather and clutter, clutter is recognized with the POD larger than 90% at clutter-to-signal-ratio greater than 4 dB even if weather echo has zero Doppler velocity (for the spectrum width smaller than 3 m s^{-1}).

In the surveillance mode, the algorithm demonstrates a POD of about 93% i.e., the same as in the Doppler mode, but the false alarm rate is about 12%. Recognition of echoes due to anomalous propagation has the POD of about 88%, i.e., slightly less than in the Doppler mode.

Clutter recognition rate with the algorithm can be increased by narrowing of the polarimetric thresholds. The lower Z_{DR} threshold parameters, i.e., -2 dB, can be raised up using correction of differential reflectivity for differential attenuation. Used ρ_{hv} threshold 0.8 defends the algorithm against low level bright bands which are observed in central Oklahoma only in the cold seasons. Preliminary analysis shows that the φ_{dp} deviations can be narrowed as well. All these combined will increase the probability of ground clutter recognition. Thus, with further refinement it is worth considering for generation of a instantaneous “clutter maps”. Simplicity and operation on signals from single range

locations are in its favor. Furthermore, it is straight forward to immediately remove the clutter following recognition and obtained the spectral moments and the polarimetric variables with minimal additional computations. The algorithm also prevents the removal of weather signals in situations where precipitation has zero Doppler velocity.

D.6. Power Comparison

The following power comparison can be incorporated into the data processing. It is obvious that if the weather power is much stronger than the clutter power, the echo is "weather like" and there is no need for any clutter recognition algorithm even if the clutter power is not weak. This can be incorporated into data processing to save some processing time.

At a given range, a spectrum is considered "weather like" if in H- and V-channel

$$\Delta S = 10\log(\frac{\widetilde{P}}{P}) \le -30 \quad dB\,. \tag{A1}$$

In other words, if the signal power of the 3-line spectrum is 30 dB weaker than the total power, the clutter contribution can be ignored. Clutter signals never pass inequality (A1) because the 3-line spectrum contains almost all their power.

Consider application of (A1) for a mixture of weather and clutter signals. Let indexes 'c' and 'w' denote clutter and weather returns. If (A1) is satisfied, Z_{DR} is

$$Z_{DR} = 10\log\frac{S_{hw}+S_{hc}}{S_{vw}+S_{vc}} = Z_{DRw} + 10\log\left(\frac{1+S_{hc}/S_{hw}}{1+S_{vc}/S_{vw}}\right) \approx Z_{DRw} + \frac{1}{\ln 10}\left(\frac{S_{hc}}{S_{hw}} - \frac{S_{vc}}{S_{vw}}\right).$$

Where S stands for signal power, i.e., returned power minus noise power. We see that Z_{DR} is biased but the bias is smaller than 10^{-3} dB and it can be neglected.

Consider next measurements of the correlation coefficients. Let R be the module of the correlation function of the signal so that $R = (S_h S_v)^{1/2}\rho_{hv}$. For the weather and clutter contributions, we write $R_w = (S_{hw}S_{vw})^{1/2}\rho_{hvw}$ and $R_c = (S_{hc}S_{vc})^{1/2}\rho_{hvc}$. For the mixture of weather and clutter, $R = R_w + R_c$. The worst case for ρ_{hv} bias is if clutter is uncorrelated, i.e., $\rho_{hvc} = 0$. In this worst case,

$$\rho_{hv} = \frac{R_w}{[(S_{hw}+S_{hc})(S_{vw}+S_{vc})]^{1/2}} = \rho_{hvw}\frac{1}{[(1+S_{hc}/S_{hw})(1+S_{vc}/S_{vw})} \approx \rho_{hvw}(1-\frac{S_{hc}}{S_{hw}}-\frac{S_{vc}}{S_{vw}}).$$

It follows from the latter that if (A1) is fulfilled the bias of ρ_{hv} is less than 2 10^{-3} and can be neglected.

Next, consider φ_{dp} measurements. Let R be the signal complex correlation function so that $R = (S_h S_v)^{1/2}\rho_{hv}\exp(j\varphi_{dp})$ and for the mixture of weather and clutter returns, we write $R = R_w + R_c = (S_{hw}S_{vw})^{1/2}\rho_{hvw}\exp(j\varphi_{dpw}) + (S_{hc}S_{vc})^{1/2}\rho_{hvc}\exp(j\varphi_{dpc})$. Tangent of the measured differential phase is

$$\tan(\varphi_{dp}) = \frac{\sin(\varphi_{dpw})+x\sin(\varphi_{dpc})}{\cos(\varphi_{dpw})+x\cos(\varphi_{dpc})}, \qquad x = \frac{(S_{hc}S_{vc})^{1/2}\rho_{hvc}}{(S_{hw}S_{vw})^{1/2}\rho_{hvw}} << 1.$$

Consider two opposing cases, $\varphi_{dpw} = 0$ and $\varphi_{dpw} = 90^o$. In the first case,

$$\tan(\varphi_{dp}) = \frac{x\sin(\varphi_{dpc})}{1 + x\cos(\varphi_{dpc})} \approx x\sin(\varphi_{dpc}) \leq 0.11^{o}.$$

In the second case,

$$\tan(\varphi_{dp}) = \frac{1 + x\sin(\varphi_{dpc})}{x\cos(\varphi_{dpc})} \approx \frac{1}{x\cos(\varphi_{dpc})} > 10^{3},$$

$$\varphi_{\mathrm{dp}} \approx 90^{\mathrm{o}} - 0.06^{\mathrm{o}}.$$

We see that in both of these cases, the φ_{dp} bias is small and therefore it is small for any case if (A1) is satisfied. Thus we conclude that the biases of the polarimetric variables are small if (A1) is satisfied and signal can be considered weather like regardless of the presence of clutter.

D.7. Appendix References

Berenguer M., D. Sempre-Torres, C. Corral, and R. Sanches-Diezma, 2006: A fuzzy logic technique for identifying nonprecipitating echoes in radar scans. *J. Atmos. Ocean. Technol.*, **23**, 1157-1179.

Billingsley, J.B., 2001: *Low angle radar land clutter*. William Andrew Publishing, 703 pp.

Dixon, M., C. Kessinger, and J. Hubbert, 2006: Echo classification within the spectral domain to discriminate ground clutter from meteorological targets. IIPS, P9.6.

Doviak, R. J. and D. S. Zrnić, 1993: *Doppler radar and weather observations*, 2nd ed., Academic Press, 562 pp.

Ellis, S., C. Kessinger, J. VanAndel, M. Dixon, and J. Hubbert, 2003: Enhansments in clutter/precipitation discrimination for the WSR-88D. IIPS 19, P2.9.

Gourley, J.J., P.Tabary, and J. P. du Chatelet, 2007: A fuzzy logic algorithm for the separation of precipitating from nonprecipitating echoes using polarimetric radar observations. *J.Atmos. Ocean. Technol.*, **24**, 1439-1451.

Ice, R.L., R.D.Rhoton, D.S. Saxion, N.K. Patel, D.A. Sirmans, D.A. Warde, D.L. Rachel, and R.G. Fehlen, 2004: Evaluation of the WSR-88D ORDA system signal processing. 20th IIPS.

Kessinger C., J. VanAndel, S. Ellis, G. Meymaris, 2003:The radar echo classifier: a fuzzy logic algorithm for the WSR-88D. 3rd Conf. Artif. Intell. Applic to Envir. Sci., AMS, 9-13.

Saffle, R. E., G. S. Cate, and M. Istok, 2007: NEXRAD Product Improvement—Update 2007. *23 Conf. on IIPS, Amer. Meteorol. Soc*., San Antonio, TX, paper 5B.1.

Siggia, A.D., and R.Passarelli Jr., 2004: Gaussian model adaptive processing (GMAP) for improved ground clutter cancellation and moment calculation. 3rd European Conf. Radar Meteorol. Hydrol.(ERAD), 67-73.

Steiner, M, and J.A. Smith, 2002: Use of three–dimensional reflectivity structure for automated detection and removal of nonprecipitating echoes in radar data. *J.Atmos. Ocean. Technol.*, **19**, 673-686

Yo-Han Cho, GyuWon Lee, Kyung-Eak Kim, and I. Zawadzki, 2006: Identification and removal of groung echoes and anomalous propagation using the characteristics of radar echoes. *J. Atmos. Ocean. Technol.*, **23**, 1206-1222.

Zrnić, D.S., A. Ryzhkov, J. Straka, Y. Liu, and J. Vivekanandan, 2001: Testing a procedure for automatic classification of hydrometeor types. *J. Atmos. Ocean. Technol.*, **18**, 892-913.

Zrnić, D.S., V.M. Melnikov, and A. V. Ryzhkov, 2006: Correlation coefficients between horizontally and vertically polarized returns from ground clutter. *J. Atmos. Ocean. Technol.*, **23**, 381-394.